# Theoretical study of spin-polarized surface states on metal surfaces

**Dissertation**

zur Erlangung des akademischen Grades
doctor rerum naturalium (Dr. rer. nat.)

vorgelegt der

Mathematisch-Naturwissenschaftlich-Technischen Fakultät
(mathematisch-naturwissenschaftlicher Bereich) der
Martin-Luther-Universität Halle-Wittenberg

von Herrn **Pavel Ignatiev**
geb. am: 11 Februar 1979 in Puschtschino,
Russische Föderation

angefertigt am Max-Planck-Institut
für Mikrostrukturphysik in Halle an der Saale

Gutachterin/Gutachter:
1. Prof. Dr. Patrick Bruno
2. Prof. Dr. Ingrid Mertig
3. Prof. Dr. Johannes Barth

Halle an der Saale, den 1.07.2008          verteidigt am 15. April 2009

# Abstract

Spin-polarisierte Oberflächenzustände, die auf den mit niederdimensionalen Strukturen dekorierten Oberflächen von edlen Metallen entstehen, werden mit Hilfe der ab-inito KKR Methode untersucht. Diese Methode ist eine Umsetzung der Dichtefunktional-Theorie in der Lokale-Spin-Dichte-Näherung (LSDA). Der Akzent der Arbeit liegt auf zwei unterschiedlichen Systemen: dekorierte gestufte Oberflächen und magnetische Co Nanoinseln auf (111) Oberflächen der edlen Metalle. Für das erste System wird gezeigt, dass die Spin-abhängige Streuung an monoatomaren magnetischen Ketten, die an den Stufenabsätzen von vicinalen Oberflächen platziert sind, einen starken Einfluss auf die Oberflächenzustände zeigt und zu dessen Polarisierung führt. Die änderungen der Bandstruktur werden angesprochen. Wir schlagen einen Weg vor, wie man auf vicinalen Oberflächen niederdimensionale magnetische Strukturen mit Hilfe der Atom-Atom und Atom-Stufe Wechselwirkungen erzeugen kann. Bei dem zweiten System, den magnetischen Co Nanoinseln auf (111) Oberflächen von edlen Metallen, sprechen wir gezielt die Herkunft der Spin-polarisierten Oberflächenzuständen an und die Rolle, die die Unterlage bei dessen Entstehung spielt. Das Zusammenspiel zwischen der energetischen Lage des Oberflächenzustandes und den mesokopischen Relaxationen in magnetischen Nanoinseln wird erläutert.

# Abstract (English)

Spin-polarized surface states arising on noble metal surfaces decorated with low-dimensional magnetic nanostructures are studied by means of the ab initio Korringa-Kohn-Rostoker Green's function method based on the density functional theory in the local spin-density approximation. We focus on two different systems: decorated stepped surfaces and magnetic Co nanoislands grown on noble metal (111) substrates. It is demonstrated for the first system that spin-dependent scattering at monatomic magnetic wires placed at step ledges of vicinal surfaces significantly affect surface states and make them spin-polarized. Changes in band structure are revealed. Then we present a way to create on vicinal surfaces at low temperatures a low-dimensional magentic nanostructures stabilized by surface-state-mediated adatom-step and adatom-adatom interactions. For the second studied system, i.e. cobalt nanoislands on noble metal (111) substrates we specially focus on the origin of spin-polarized surface states and on a role of substrate in their formation. The interplay between energy positions of surface states and mesoscopic relaxation in magnetic nanoislands is demonstrated.

# Contents

# Introduction

The avalanche-like development of microelectronics, magnetoelectronics and spintronics produces more complicated devices of a smaller size. Nowadays the smallest device elements are only several nanometers in size, so further downscaling turns them into purely quantum systems obeying laws of quantum mechanics. Though the ultimate goal, the invention of quantum computers, has been already announced, many practical and theoretical aspects are still not clear even for rather simple atomic-scale systems, like thin films, nanoislands, stripes, chains, small clusters and adatoms on surfaces. The main advantage of such nanostructures, i.e. the possibility to tune their electronic and magnetic properties by adjusting appropriate structure or environment, turns into a real problem, because the strong dependency of properties on atomic species involved hinders relevant generalizations. That is why a combined effort of experiment and theory is essential to reveal the detailed description of atomic-scale systems.

This work is dedicated to the investigation of special electronic states arising at metal surfaces. Despite the fact that first theoretical predictions and descriptions of these surface states were made more than 70 years ago they are still in focus of modern solid state science. Surface states on the one hand can be easily probed by various experimental techniques and on the other hand they are found to be perfect sensors of such material properties as a substrate structure, magnetism of thin films and adsorbates. Recent studies have clearly demonstrated that surface states can govern self organization of atomic scale ordered structures.

The most of systems we are dealing with in this work support spin polarized surface states. Spin polarization is achieved by decoration of nonmagnetic noble metal substrate with a low dimensional magnetic nanostructure. One dimensional magnetic nanostructures are represented by the monatomic Fe rows decorating step ledges of Cu(111) vicinal surfaces. We thoroughly trace how electronic states revealed on clean stepped Cu(111) substrates become spin-polarized on decorated step surfaces. The next kind of system we study is a small magnetic nanoisland on flat noble metal surfaces. We follow the evolution of spin-polarized surface states above magnetic nanostructures depending on their size: from a single magnetic adatom to infinite bilayers. In our work we specially focus on the origin of spin-polarized surface states on bilayer Co films and a role of substrate in their formation. Finally, the interplay between energy positions of surface states and mesoscopic relaxation in magnetic nanoislands is studied. All the calculations are performed with the help of the Korringa-Kohn-Rostoker Green's function method exploiting the density functional theory in the local density approximation.

The thesis is organized as follows.

The first chapter is an introduction to the surface state theory. We start from electronic states in the infinite crystall and demonstrate how new electronic states appear on a surface. We mention both mathematical and physical origins of Tamm and Shockley surface states.

The chapter is finished by modern experimental results on the surface state on noble metals {111} surfaces

In the second chapter we present the theory of scanning tunneling microscopy/ spectroscopy (STM/STS) by Tersoff and Hamann and demonstrate that STS data can be directly compared to the calculated density of states at the position of an STM tip. The key experimental works reviewed in this chapter convince a reader that STM/STS experiments on surface states can be supported by a simple but qualitatively correct theoretical quantum-mechanical description which helps to understand observed phenomena.

The third chapter describes theoretical methods applied in this study. Basics of the density functional theory are presented in the first section of the chapter. It is demonstrated how a many-body quantum problem can be reduced to an equivalent single-particle one. The second section contains the description of the Korringa-Kohn-Rostoker Green's function method. Theory underlying this method is presented. Basics of its applications to the calculations of infinite periodic 3D and 2D structures and real-space atomic configurations are demonstrated by example of Cu(111) surface and Fe adatom on Cu(111) surface. A molecular dynamics approach based on the many-body interatomic potentials formulated in the second moment of tight-binding approximation is mentioned as a rather simple way to obtain relaxed atomic configurations in the last section of the chapter.

The fourth chapter of the work presents our results on electronic confinement on stepped Cu(111) surfaces. We, at first, describe a modern view on the surface state on stepped surfaces and report on our ab initio investigations of surface states on clean Cu(111) vicinals. Then we proceed to the study of Cu(111) vicinals decorated with Fe wires and demonstrate that localization of the minority surface-states electrons at Fe wires results in the formation of spin-polarized surface states. At the end of the chapter we explain how a novel type of 1D magnetic Fe nanostructures can be grown on Cu(111) vicinal surface exploiting surface state confinement.

The fifth chapter is devoted to the spin-polarized surface states on bilayer Co islands grown on noble metal substrates. We focus on the influence of structural properties of the Co nanoislands on the spin-polarized surface states. By means of ab-initio methods we demonstrate the evolution of electronic states above Co nanoislands of various sizes starting from a single Co adatom up to Co bilayers. We show the origins of majority and minority surface states. We illustrate the effect of the stacking of Co bilayer on the spin-polarized surface states. Finally, comparing surface states on Co nanoislands on Cu(111) and Au(111) substrates we figure out the essential role of the substrate on the surface states and demonstrate that variation of the substrate lattice constant permits to tune energies of surface states.

In the last chapter, we demonstrate the interplay between strain-induced structural relaxations and the surface states of Co nanoislands on Cu(111). Recent STS experiments have established that the occupied surface states exhibit a size-dependent energy shift A shift has been also observed at the corners and edges of the island with respect to the center of the island. Our atomic-scale simulations and *ab initio* calculations demonstrate that the energy positions of the occupied surface states are determined by mesoscopic relaxations in the nanoislands. Our work suggests that surface states can be a sensitive probe for variations of the atomic structure at the nanoscale.

# Chapter 1

# Surface states: introduction

It was revealed quite early that electronic states at surfaces differed from their bulk counterparts. The first theoretical description of a new class of electronic states bounded to the surface was made by I.E. Tamm in 1932 [1]. Since that time the theory of surface states has been developed and extended; its prior conclusions and predictions were confirmed experimentally. This chapter provides basics of the surface state theory. We demonstrate mathematical and physical origins of surface states and the chapter is finished by modern experimental results on the surface state on {111} surfaces of noble metals.

## 1.1   Electrons in infinite crystals

The electronic structure of a solid having $N$ nuclei of masses $M_i$ with atomic numbers $Z_i$ at positions $\mathbf{R}_i$ and $n$ electrons can be described by solution of the quantum many body problem [2, 3]

$$
\left[ -\sum_{i=1}^{N} \frac{\hbar^2}{2M_i} \nabla_{\mathbf{R}_i}^2 - \sum_{k=1}^{n} \frac{\hbar^2}{2m_e} \nabla_{\mathbf{r}_k}^2 + \frac{1}{4\pi\varepsilon_0} \sum_{j=1}^{N} \sum_{i>j}^{N} \frac{Z_i Z_j}{|\mathbf{R}_i - \mathbf{R}_j|} - \right.
$$

$$
\left. -\frac{1}{4\pi\varepsilon_0} \sum_{k=1}^{n} \sum_{i=1}^{N} \frac{Z_i e}{|\mathbf{r}_k - \mathbf{R}_i|} + \frac{1}{4\pi\varepsilon_0} \sum_{k=1}^{n} \sum_{l>k}^{n} \frac{e^2}{|\mathbf{r}_k - \mathbf{r}_l|} \right] \psi = E\psi, \tag{1.1}
$$

where $m_e$ and $e$ are the mass and the charge of an electron, $\varepsilon$ is the universal constant of free space permittivity, $\psi = \psi(\mathbf{r}_1, \mathbf{r}_2, \ldots, \mathbf{r}_n)$ is the many body wavefunction and $E$ is the total energy of the system. Very often equation (1.1) is written in atomic units, whereby $\hbar = e_m = m_e = 4\pi\varepsilon_0 = 1$. Both exact and numerical solutions of this problem formulated for an infinite crystal are actually based on two main approximations. The first, *adiabatic approximation of Born and Oppenheimer*, assumes that nuclei move much more slowly than electrons, so nuclei and electronic motions can be separated. The second approximation, *one-electron approximation*, permits to substitute the many-body electronic problem with a single-particle, which describes an electron moving in effective potential $v(r)$ consisting of nuclei potentials and a potential all other electrons. This approximation is considered in details in Section 3.1. Under these two assumptions equation (1.1) takes the form

$$
\left\{ -\frac{\hbar^2}{2m} \nabla^2 + v(\mathbf{r}) + \int \frac{\rho(\mathbf{r}')}{|\mathbf{r} - \mathbf{r}'|} d\mathbf{r}' \right\} \psi_k(\mathbf{r}) = \epsilon_k \psi_k(\mathbf{r}), \tag{1.2}
$$

Since any ideal crystal by definition has translational symmetries, effective atomic potential $v(\mathbf{r})$ is periodic and can be generally written as

$$v(\mathbf{r}) = v(\mathbf{r} + \mathbf{a}_n), \tag{1.3}$$

where $\mathbf{a}_n$ are vectors of the crystall lattice. According to the Bloch-Floquet theorem [4, 5] solutions $\psi$ of equation (1.2) with periodic potential (1.3) may be written in the form:

$$\psi_{\mathbf{k}}(\mathbf{r}) = u_{\mathbf{k}}(\mathbf{r}) \cdot e^{i\mathbf{k}\cdot\mathbf{r}}, \tag{1.4}$$

where $\mathbf{k}$ is the wave vector and the function $u_{\mathbf{k}}(\mathbf{r})$ has a three-dimensional periodicity of the crystall lattice, i.e.:

$$u_{\mathbf{k}}(\mathbf{r}) = u_{\mathbf{k}}(\mathbf{r} + \mathbf{a}_n). \tag{1.5}$$

Substituting solution of the form (1.4) into the Schrödinger equation (1.2) leads us after simple transformations to

$$-\nabla^2 u_{\mathbf{k}}(\mathbf{r}) + v(\mathbf{r}) u_{\mathbf{k}}(\mathbf{r}) - 2i(\mathbf{k}\cdot\nabla u_{\mathbf{k}}(\mathbf{r})) = (E_{\mathbf{k}} - \mathbf{k}^2) u_{\mathbf{k}}(\mathbf{r}). \tag{1.6}$$

Since potential $v(\mathbf{r})$ and wave function envelope $u_{\mathbf{k}}(\mathbf{r})$ are periodic, they can be represented as a Fourier series:

$$v(\mathbf{r}) = \sum_{\mathbf{g}} V_{\mathbf{g}} e^{2\pi i(\mathbf{b_g}\cdot\mathbf{r})}, \tag{1.7}$$

$$u_{\mathbf{k}}(\mathbf{r}) = \sum_{\mathbf{h}} a_{\mathbf{h}} e^{2\pi i(\mathbf{b_h}\cdot\mathbf{r})},$$

where $\mathbf{b_g}$ and $\mathbf{b_h}$ are reciprocal lattice vectors. Setting constant term $V_0 = 0$ and substituting (1.7) into (1.6) we obtain an infinite linear homogeneous set of equations for the coefficients $a_{\mathbf{h}}$

$$a_{\mathbf{h}}\left[E_{\mathbf{k}} - (\mathbf{k} + 2\pi\mathbf{b_h})^2\right] - \sum_{\mathbf{g}\neq 0} V_{\mathbf{g}} a_{\mathbf{h-g}} = 0. \tag{1.8}$$

Non-trivial solutions of (1.8) vanish the determinant, so exact values of the allowed energies of the system can be found as solutions of an infinite order secular equation. A particular solution depends on the form of the potential and is an object for various ab initio methods. Nevertheless it is possible to demonstrate fundamental features of the band theory involving into consideration even the simplest model in the framework of the nearly free electron approximation.

## 1.2   Nearly free electron approximation

The nearly free electron approximation is based on the assumption that electrons move in the weak periodic potential $v(r)$. Mathematically potential weakness is determined by the following statements: all the Fourier coefficients $V_{\mathbf{g}}$ in eq. (1.7) can be treated as first-order corrections to the free-electron case; all $a_{\mathbf{h}}$ in eq. (1.7) are small in comparison to $a_0$ because $u_{\mathbf{k}}$ is almost independent of $\mathbf{r}$. Neglecting second-order terms (including products $V_{\mathbf{g}} \cdot a_{\mathbf{h-g}}$, $\mathbf{g} \neq \mathbf{h}$) we come to the following approximation to (1.8)

$$a_{\mathbf{h}}\left[E_{\mathbf{k}} - (\mathbf{k} + 2\pi\mathbf{b_h})^2\right] - V_{\mathbf{h}} a_0 = 0. \tag{1.9}$$
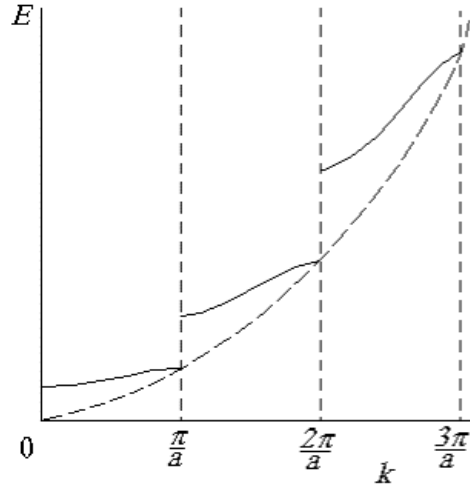
**Figure 1.1:** Dispersion relation $E(k)$ (solid curve) of electrons propagating in the 1D weak periodic potential is derived according to nearly free electron approximation. Free electron dispersion relation $E \propto k^2$ is drawn by dashed line. Periodic potential opens up gaps in the continuous energy spectra thus forming a set of bands.

Secular equation in this case takes the form

$$\left[E_{\mathbf{k}} - (\mathbf{k} + 2\pi\mathbf{b_h})^2\right]\left(E_{\mathbf{k}} - \mathbf{k}^2\right) - |V_{\mathbf{g}}|^2 = 0. \tag{1.10}$$

The graph of $E(k)$ obtained from this equation formulated for a one-dimensional (1D) system where $\mathbf{b_g} \equiv b_g = \pm g/a$; $k = \pm \pi g/a$, $g = 1, 2, \ldots$ is shown in Fig. 1.1 together with the free-electron curve $E_0(k) \sim k^2$. Periodic potential opens up gaps in the continuous free-electron curve, thus forming a series of allowed bands separated by gaps. The upper and the lower gap edges are located at

$$E^\pm = \left(\frac{\pi g^2}{a}\right) \pm |V_g|. \tag{1.11}$$

Bloch wave functions $\Psi^\pm$ at the band edges can be derived from (1.4):

$$\Psi^\pm = a_0 \left(e^{\mathrm{i}\pi x/a} \pm \frac{V_1}{|V_1|}e^{-\mathrm{i}\pi x/a}\right). \tag{1.12}$$

Symmetry of wave functions $\Psi^\pm$ bounding the gap depends on the sign of $V_1$:

$$\Psi^+ = \begin{cases} cos\left(\frac{\pi x}{a}\right), & V_1 > 0 \\ sin\left(\frac{\pi x}{a}\right), & V_1 < 0 \end{cases} \tag{1.13}$$

$$\Psi^- = \begin{cases} sin\left(\frac{\pi x}{a}\right), & V_1 > 0 \\ cos\left(\frac{\pi x}{a}\right), & V_1 < 0 \end{cases} \tag{1.14}$$

For negative $V_1$ the wave function for the lower band edge is even (s-type) and that for the upper edge is odd (p-type). Such a gap is known as the direct gap. If the wave function of the lower band edge is of p-type, the gap is called an inverted gap, in order to emphasize the inverted order of isolated atomic levels. The type of the gap, as we show further, affects electronic states rising at crystal surfaces.

## 1.3   Electrons at crystal surfaces

Real crystals are always limited by surfaces and thus are finite. It can be demonstrated that in a finite crystal consisting of $N$ atoms allowed bands split into a sequence of $N$ discrete levels. These levels lie in the bulk band gaps, i.e. in the regions inaccessible to electrons of original bulk material. Modern solid state physics tends to distinguish between two types of surface state: Tamm surface states [1] and Shockley surface states [6]. Below we briefly describe the origin and differences of both types.

Tamm was the first who considered the changes in the band structure introduced by a surface. In his original work [1] he considered a 1D crystall as an infinite array of $\delta$-potentials and introduced a surface by terminating the array from the one side. The key point of the Tamm's approach was to match wave functions and their derivatives in vacuum region to those in the crystall. Wave function inside the crystall can be written as

$$\Psi_{crystal} = A\left(e^{ik_1 x} + \lambda e^{-ikx}\right). \tag{1.15}$$

The wave function can be analytically continued to the band gap region, if a complex $k$ of the following form is introduced

$$k = \xi + \mathfrak{i}\mu, \quad \mu \geq 0. \tag{1.16}$$

The real part $\xi$ describes plane waves propagating in bulk crystal. Complex part $\mathfrak{i}\mu$ is responsible for decay of surface related states inside the crystal. Wave functions $\Psi^{\pm}$ (1.12) associated with the upper and the lower gap edges (1.11) are real but of different parity (1.13), i.e. have the phase shift $|\delta^{\pm}| = \pi/2$. Continuous complex wave function $\Psi$ can be introduced in the gap region by means of the continuously varying phase shift $\delta, (|\delta| < \pi/2)$. Wave function (1.15) takes the form

$$\Psi\left(x\right) = e^{\mu x}\cos\left(\pi x/a + \delta\right), \quad x \leq 0 \tag{1.17}$$

Cosine in (1.17) can be transformed into

$$\cos\left(\pi x/a + \delta\right) = \frac{1}{2}e^{\mathfrak{i}\delta}\left(e^{\mathfrak{i}\pi x/a} + e^{-2\mathfrak{i}\delta}e^{-\mathfrak{i}\pi x/a}\right). \tag{1.18}$$

Comparing (1.18) with (1.12) yields the link between $\delta$ and $V_1$:

$$e^{2\mathfrak{i}\delta} = \frac{E - k^2}{V_1}. \tag{1.19}$$

It is evident that the sign of $V_1$ is important and actually defines the possible values of $\delta$. To demonstrate it explicitly one should substitute complex $k$ (1.16) into (1.19) and equate complex parts on both sides of transformed (1.19):

$$\sin\left(2\delta\right) = -\frac{2\pi\mu}{aV_1}. \tag{1.20}$$

Since $\mu \geq 0$ and $|\delta| < \pi/2$, matching the signs of left and right sides of (1.20) gives the following possible values of $\delta$ for direct and inverted gaps, respectively:

$$\begin{aligned} V_1 &< 0, \qquad 0 \leq \delta \leq \pi/2 \\ V_1 &> 0, \qquad -\pi/2 \leq \delta \leq 0. \end{aligned} \tag{1.21}$$

The next step is to match the wave function (1.17) to the wave function outside the crystall. If a vacuum of a constant potential $V_0$ is present outside the crystall, the vacuum wave function can be written as

$$\Psi_{out} = De^{-k_0 x}, \qquad x \geq 0, \tag{1.22}$$

$$k_0 = \sqrt{V_0 - E}, \qquad E < V_0. \tag{1.23}$$

In general, the matching can be performed at arbitrary $x = x_0$ ($x_0 < 0$, where 0 is the position of the surface). If logarithmic derivatives of $\Psi_c$ and $\Psi_{out}$ can be matched at $x = x_0$, the wave function of the system will decay in both directions from the surface. Electrons of such a state will be localized at the surface and thus will be in a surface state. This situation is sketched in Fig. 1.2. Equation for surface state energy can be obtained from the matching procedure:

$$\frac{\pi}{a} \tan\left(\pi x_0/a + \delta\right) = (\mu + k_0). \tag{1.24}$$

For two special cases $x_0 = 0$ and $x_0 = -a/2$ equation (1.24) transforms into

$$x_0 = 0, \qquad \frac{\pi}{a} \tan\left(\delta\right) = (\mu + k_0) \tag{1.25}$$

$$x_0 = -a/2, \qquad \frac{\pi}{a} \cot\left(\delta\right) = -\left(\mu + k_0\right). \tag{1.26}$$

Since $\mu > 0$ and $k_0 > 0$ equations (1.25) and (1.26) can be satisfied only for $0 \leq \delta \leq \pi/2$ and $-\pi/2 \leq \delta \leq 0$, respectively. These conditions via (1.21) actually means that surface states arising in direct and inverted gaps are localized at different positions near the surface. Surface states appearing in the direct gap with the $s$-band at the bottom are called the Tamm state [1]. Surface states arising in the inverted gap with the $p$-band at the bottom are known as the Shockley surface state [6].

To understand the difference between these two states, one should analyze the behavior of wave function (1.17). It gets the maximal value at $x_m = \pi x_0/a + \delta$. For direct gap ($x_0 = 0$, $0 \leq \delta \leq \pi/2$) $x_m < 0$; for inverted gaps ($x_0 = -a/2$, $-\pi/2 \leq \delta \leq 0$) $x_m > 0$. Since $x = 0$ is the position of the topmost atomic layer it is possible to conclude that the Tamm surface state is localized at the surface atom and the Shockley surface state gets its maximal density in the vacuum, as is demonstrated in Fig. 1.2.

## 1.4 Quasi-2D free electron-like electrons on the noble metal surfaces

Noble metal surfaces supports on their {111} facets the Shockley-type surface state. Surface state electrons are bound to the surface because surface state density decays exponentially both into the vacuum and into the bulk (Fig. 1.2). As the simplest approximation the motion of surface state electrons in the surface plane can be treated as free-electron one, thus yielding the dispersion relation

$$E\left(k_\parallel\right) = E_0 + \frac{\hbar^2}{2m^*} k_\parallel^2, \tag{1.27}$$

where $E_0$ is the energy of the surface state band bottom, $m^*$ is the effective electron mass, $k_\parallel$ is the wave vector parallel to the surface. Strictly speaking, the model of nearly free
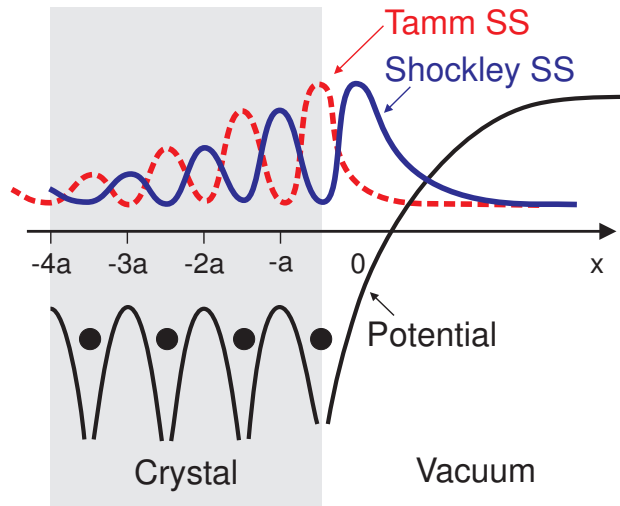
**Figure 1.2:** Sketch of the Shockley (solid blue line) and Tamm (dashed red curve) surface states wave functions.

**Table 1.1:** The summary of the parabolic dispersion fits results from Ref.[7] The two parabolas of the Au(111) surface state split due to spin-orbit coupling are centered at $\pm 0.013$ Å$^{-1}$.

|          | $E_0$ (meV) | $m^*/m_e$ | $k_F$ (Å$^{-1}$) |
|----------|-------------|-----------|------------------|
| Cu(111)  | $435 \pm 1$ | 0.412     | 0.215            |
| Ag(111)  | $65 \pm 1$  | 0.397     | 0.080            |
| Au(111)  | $487 \pm 1$ | 0.255     | 0.167/0.192      |

electrons propagating in the weak potential of surface atoms is more applicable, but, as was revealed by a number of experiments, the corrections introduced are not principal. As an example, the band structure of the surface states on Cu(111), Ag(111) and Au(111) surfaces measured by means of angle-resolved photoemission spectroscopy (ARPES) are demonstrated in Fig. 1.3 [7]. Shaded areas in the top panels correspond to the projected bulk band. The circular shape of the surface state Fermi surface (FS) reflects the isotropic dispersion parallel to the surface. Dispersion relation (1.27) fitted to the experimental data is drawn in Fig. 1.3. Fitting parameters are listed in Table 1.1 as well as the value $k_F$ equal to $k_\parallel$ at the Fermi energy. In the case of Au(111), the spin-orbit coupling caused by the structure inversion asymmetry (the Rashba effect [8]) results in a spin splitting of the surface state band proportional to $k$, and equation (1.27) takes the form [9, 10]:

$$E_\pm \left( k_\parallel \right) = E_0 + \frac{\hbar^2}{2m^*} k_\parallel^2 \pm \gamma_{SO} |k_\parallel|, \tag{1.28}$$

where the positive parameter $\gamma_{SO}$ controls the strength of the Rashba spin-orbit interaction, The "+" solution gives rise to an "inner" band of Au(111) surface state, the "−" solution to an "outer" one [10].

Up to 90th, surface states were probed mostly by various emission spectroscopy methods. Reviews of the main results can be found in the book by Davison et al. [11] and in the review
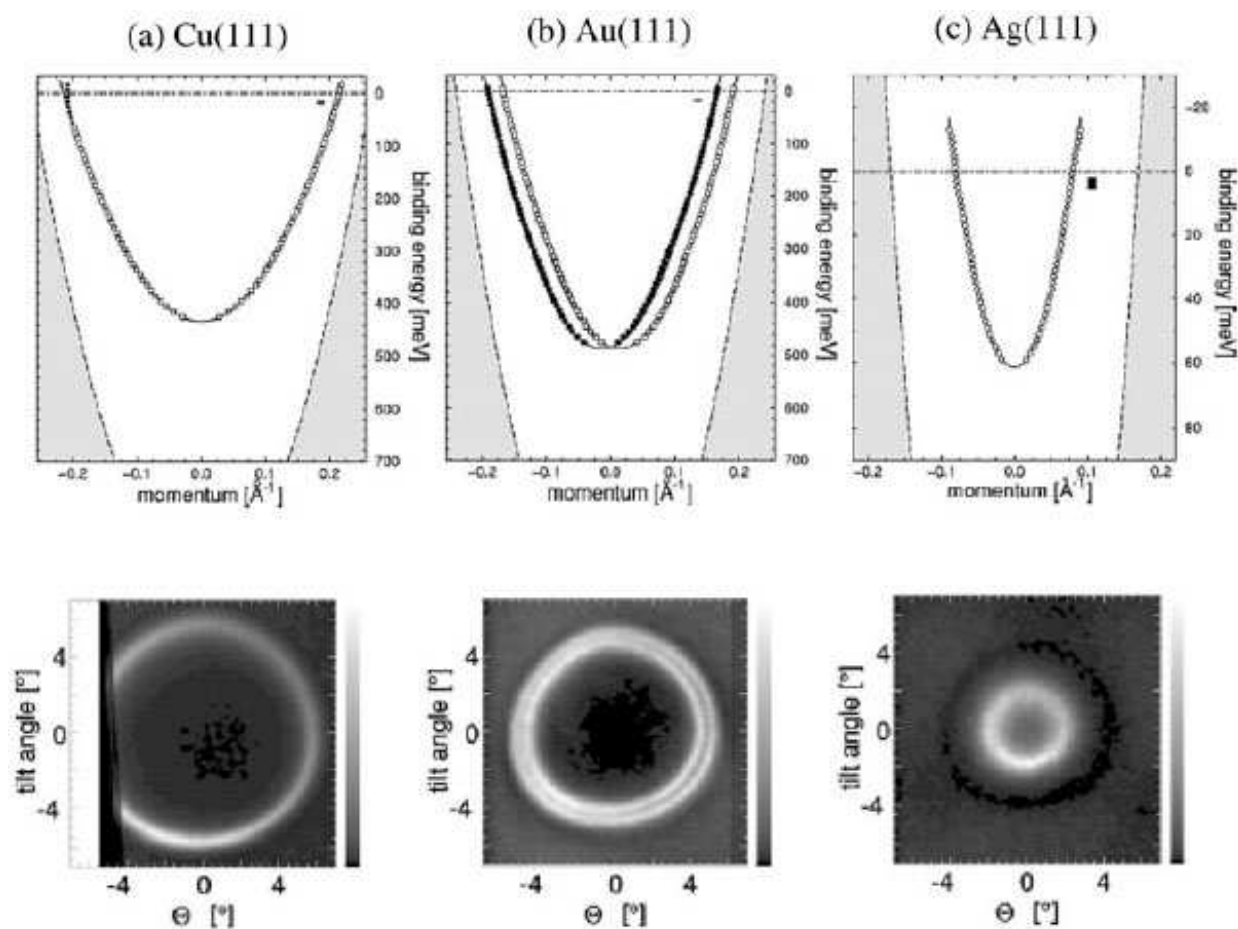
**Figure 1.3:** Surface state bands (top) and Fermi surface (bottom) of (a) Cu(111), (b) Au(111) and (c) Ag(111). The shaded areas in the top panels correspond to the bulk band projections. The circular shape of the FS reflects the isotropic dispersion parallel to the surface. In the case of Au(111), the surface state band splits due to the spin-orbit coupling, which leads to two concentric rings in the FS (The figure is adapted from [7]).

by Memmel [12]. Surface states were found to be perfect sensors of material properties. In particular, they can be exploited to control a surface structure: properties of surface states change if the surface is reconstructed, or in presence of adsorbates [12]. Surface states were found to contribute to thin film magnetism [12]. Since the early 90th, surface states are widely investigated by scanning tunneling microscopy technique.

# Chapter 2

# Probing of surface states with STM/STS

Scanning tunneling microscopy/spectroscopy (STM/STS) is one of the most advanced and flexible experimental techniques. In this chapter we present a theory of STM/STS and demonstrate that STS data can be directly compared to the calculated density of states at the position of an STM tip. This fact permits, on the one hand, to support STM/STS experiments by a simple but qualitatively correct theoretical description which helps to understand laws of quantum mechanics underlying observed phenomena, and on the other hand, provides a unique possibility to compare experimental results with density of states calculated from the first principles. Here we focus on noble metal {111} surfaces, review key experiments on surface state confinement to islands and vacancy craters, on surface state interaction with adsorbates and on surface states on stepped surfaces. Finally we briefly sketch the spin-polarized STS as a tool providing access to the information on spin channels of surface states on magnetic nanostructures.

## 2.1   The theory of STM

STM is based upon the quantum tunneling effect. In classical mechanics a particle needs an extra energy to overcome a potential barrier. In quantum mechanic when a particle faces a potential barrier it possesses a nonzero probability to tunnel directly through it without extra energy consumption. It can be easily demonstrated that for the simplest case of an electron inciding a rectangular potential barrier of width $d$ and height $U$, the tunneling probability is [13]:

$$T(E) \sim \exp\left[-\frac{2d}{\hbar}\sqrt{2m(U-E)}\right].$$ (2.1)

More general expression for an arbitrary form barrier can be obtained using perturbation WKB theory [13]:

$$T(E) \sim \exp\left[-\frac{2}{\hbar}\int_{z_1}^{z_2}\sqrt{2m(U(z)-E)}dz\right].$$ (2.2)

In metals valence band lies at the Fermi level, so if a sharp tip is brought in the proximity of a metal surface, electrons can tunnel from the tip to the surface or vice versa as sketched in Fig. 2.1(a). The barrier heights are determined by the tip and the sample work functions $\Phi_{tip}$ and $\Phi_{sample}$. The relative positions of the tip and the sample Fermi levels can be tuned
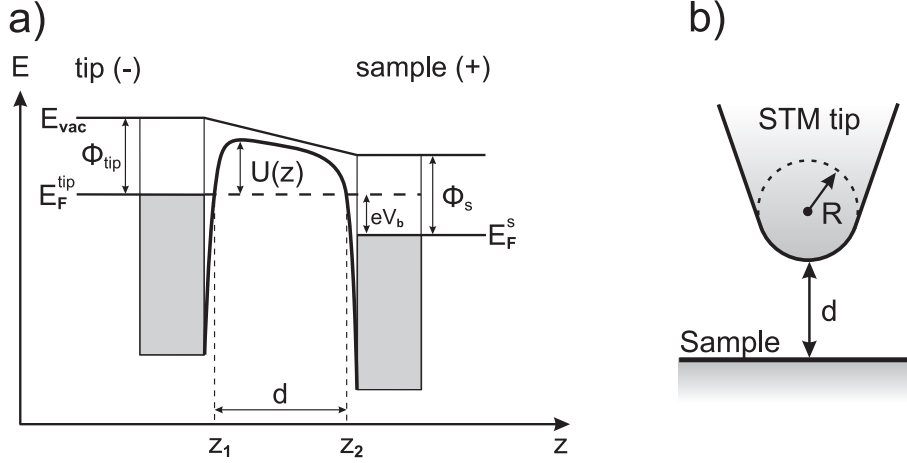
**Figure 2.1:** (a) The STM tunneling contact. See the text for details. (b) A spherical tip approximation suggested by Tersoff and Hamann [14].

by the bias voltage $V_b$. Such a construction of the system permits to alter the tunneling barrier by the variations of the tip-sample distance $d$ and bias voltage $V_b$ and, hence, affects the tunneling current measured in STM/STS. But here arises a question how to interpret measured data.

Tersoff and Haman suggested a simple theoretical approach to model the STM [14]. They considered an arbitrary surface and a spherical tip of radius $R$ at the point $\mathbf{r}_0$. The distance between the tip and the surface was $d$ as sketched in Fig. 2.1(b). The Bardeen formalism was used for the current calculations [15]. The assumption was that once electron was injected into an unoccupied sample state (negative bias voltage) or removed away from a sample state (positive bias) it never came back. Physically this means that injected electron propagates far away from the tip before it can tunnel back and electrons removed from the surface into the continuum of tip states also do not tunnel back. The current is

$$I = \frac{2\pi e}{\hbar} \sum_{\mu,\nu} f(E_\mu)\left(1 - f\left(E_\nu + eV_b\right)\right)|M_{\mu\nu}|^2 \delta\left(E_\mu - E_\nu\right), \qquad (2.3)$$

where $f(E)$ is the Fermi function and $M_{\mu\nu}$ is the matrix element for tunneling between the tip states $\Psi_\mu$ and the sample states $\Psi_\nu$. In the simplest approximation the tip can be replaced with a point probe, which, following Tersoff and Haman [14], represents the ideal case of a nonintrusive measurement. Matrix elements $M_{\mu\nu}$ and *tunneling current*, hence, are simply *proportional to the surface local density of states (LDOS) at the position of the tip*.

A more detailed treatment of (2.3) requires calculation of $M_{\mu\nu}$ [14]. Bardeen showed [15] that

$$M_{\mu\nu} = \frac{\hbar}{2m} \int \left(\Psi_\mu^* \nabla \Psi_\nu - \Psi_\nu^* \nabla \Psi_\mu\right) \mathbf{ds}, \qquad (2.4)$$

where the integration is taken over any surface lying entirely within the barrier region separating the sample and the tip. The quantity in parenthesis is simply the current operator. Tersoff and Haman took the wave function of the tip in the asymptotic spherical form

$$\Psi_\mu = \frac{\Phi_{tip}}{\sqrt{\Omega_{tip}}} R \cdot e^{\kappa R} \cdot \frac{1}{|\mathbf{r} - \mathbf{r}_0|} \cdot e^{-\kappa|\mathbf{r} - \mathbf{r}_0|}, \qquad (2.5)$$

where $\Omega_{tip}$ is the tip volume and $\kappa = \hbar^{-1}\sqrt{2m\Phi_{tip}}$. Sample states can be represented in general form by $s$-type Bloch functions exponentially decaying into the vacuum [14]:

$$\Psi_\nu = \frac{\Phi_{sample}}{\sqrt{\Omega_{sample}}} \sum_{\mathbf{G}} a_b \cdot \exp\left[\mathfrak{i}(\mathbf{G} + \mathbf{k}_\parallel)\rho - z\sqrt{\kappa^2 + (\mathbf{G} + \mathbf{k}_\parallel)^2}\right]. \tag{2.6}$$

Tersoff and Haman obtained the following expression for the matrix elements:

$$M_{\mu\nu} = \frac{\hbar^2}{2m}4\pi\kappa^{-1}\sqrt{\Omega_{tip}}\kappa R \cdot e^{\kappa R}\Psi_\nu(\mathbf{r}_0). \tag{2.7}$$

And for the tunneling current:

$$I = \frac{32\pi^3 e^2}{\hbar}\Omega_{tip}\frac{\Phi^2}{\kappa^4}\rho_{tip}(E_F)R^2 \cdot e^{2\kappa R}\rho_{sample}(\mathbf{r}_0, E_F) \tag{2.8}$$

In the theory of Tersoff and Hamann the tunneling current is proportional to the surface LDOS at the position of the tip. They claimed [14] that the made approximations appeared to introduce relatively little inaccuracy, except that the tip was treated in a model way; but even this approximation led to realistic and physically relevant picture.

## 2.2 Probing surface states with STM/STS

Davis et al. extended the Tersoff-Hamann theory to the case of surface state [16]. Surface states decay in the vacuum region in a different way than 3D Bloch states do (see eq. (2.6)). The surface states are localized in a wave function that decays into the vacuum as:

$$\Psi_{\mathbf{k}} \sim e^{\mathbf{i}\mathbf{k}\cdot\rho}\exp\left(-\int_0^z K(z)dz\right) \tag{2.9}$$

$$K(z) = \sqrt{\frac{2m}{\hbar^2}\left[U(z) - E(\mathbf{k})\right] + k^2},$$

where $U(z)$ is the potential above the surface and $\rho = \{x, y, 0\}$ is the 2D vector defined in the surface plane. A new expression for $\Psi_{\mathbf{k}}$ results in a different expression for the matrix elements $M_{\mu\nu}$ [16]

$$M \sim \exp\left[-\int_0^d K(z)dz - \frac{Rk^2}{2\tilde{\kappa}}\right], \tag{2.10}$$

$$\tilde{\kappa} = \sqrt{\frac{2m}{\hbar^2}\left(-E_\mu - eV/2\right)}, \tag{2.11}$$

so a new equation for tunneling current can be derived from (2.3) [16]

$$I \sim \int_0^\infty F(E, V)\exp\left(-2\int_0^d K(z)dz - \frac{E}{E_a}\right)dE \tag{2.12}$$

$$F(E, V) = f(E_F - E_0 + E) - f(E_F - E_0 + E + eV)$$

$$E = \frac{\hbar^2 k^2}{2m^*},$$

$$E_a = \frac{\hbar^2\kappa}{2am^*}.$$

For a qualitative understanding $\int_0^d K(z)dz$ can be expanded for small $V$ and $E$ [16], so we obtain

$$I = G_0 e^{\frac{V}{V_0}} \int\limits_0^\infty F(E,V) \exp\left(\frac{E_0 - E}{E_1}\right) dE, \tag{2.13}$$

$$V_0 = \frac{2\sqrt{\hbar^2 \Phi / 2m}}{ed},$$

$$E_1 = \frac{E_a}{1 + \frac{d}{a}\left(1 - \frac{m}{m^*}\right)},$$

where $G_0$ is the surface state conductance at zero bias and $T = 0$.

For low $T$ the conductance $dI/dV$ is proportional to the surface state density multiplied by factor depending on $V$ and $E$. At higher temperatures the discontinuous step-like onset of the surface state density at $E_0$ is smeared out giving the appearance of a peak-like feature in the spectrum. This conclusion of Davis et al. was confirmed for the first time by Crommie at al. [17]. Figure 2.2(a) demonstrates the $dI/dV$ spectrum of flat Cu(111) surface measured at 4 K with the help of polycrystalline tungsten tip. Acquired $dI/dV$ spectrum is uneven but surface state onset at $-0.44$ eV is clearly visible.

STM/STS probes a local density of the surface state at the tip position. On an ideal surface the spatial-resolved density of surface-state electrons is flat and featureless. But if any structural defect is introduced at the surface, one can expect from the basics of quantum mechanics that surface state electrons incident on the defect and scattered back from it are to interfere and form standing waves in the vicinity of the defect. These standing waves can be observed by STM/STS at low temperatures. A constant current $500 \times 500$ Å$^2$ image of Cu(111) surface from the paper by Crommie at al. is shown in Fig. 2.2(b). Monoatomic steps and a number of point defects are clearly visible. In addition STM revealed evident static spacial oscillations decaying away from the steps and point defects.

A step on Cu(111) surface can be described by a simple 1D model of free electrons inciding a step-like potential described by a Heaviside step function [13]. Local density of states at separation $x$ from the step at energy $E$ relative to the surface state band bottom is described by the following relation

$$\rho(x, E) = \frac{2}{\pi}\sqrt{\frac{2m^*}{\hbar^2 E}} \int\limits_0^{k_\perp} \frac{\sin^2(kx)}{\sqrt{1 - \frac{k}{k_\perp}^2}} dk \tag{2.14}$$

$$= \rho_0 \frac{m^*}{\pi \hbar^2}\left[1 - J_0(2k_\perp x)\right],$$

$$k_\perp = \sqrt{\frac{2m^* E}{\hbar}}, \tag{2.15}$$

where moment $k_\perp$ is parallel to the surface plane and perpendicular to steps; $J_0$ is oscillating Bessel function. Since the character of the LDOS oscillations is determined by $k_\perp$, it is possible to figure out the dispersion relation $E(k_\perp)$ from the energy dependent standing wave maps. Figure 2.2c demonstrates spatial dependency of $dI/dV$ spectra measured at different energies by Crommie et al. [17]. The inset of Figure 2.2(c) shows the fitted dispersion relation. Crommie et al. [17] observed a parabolic surface state [eq. 1.27] with the band bottom at $\sim 0.45$ eV below $E_F$ and the wavelength at the Fermi energy was equal approximately
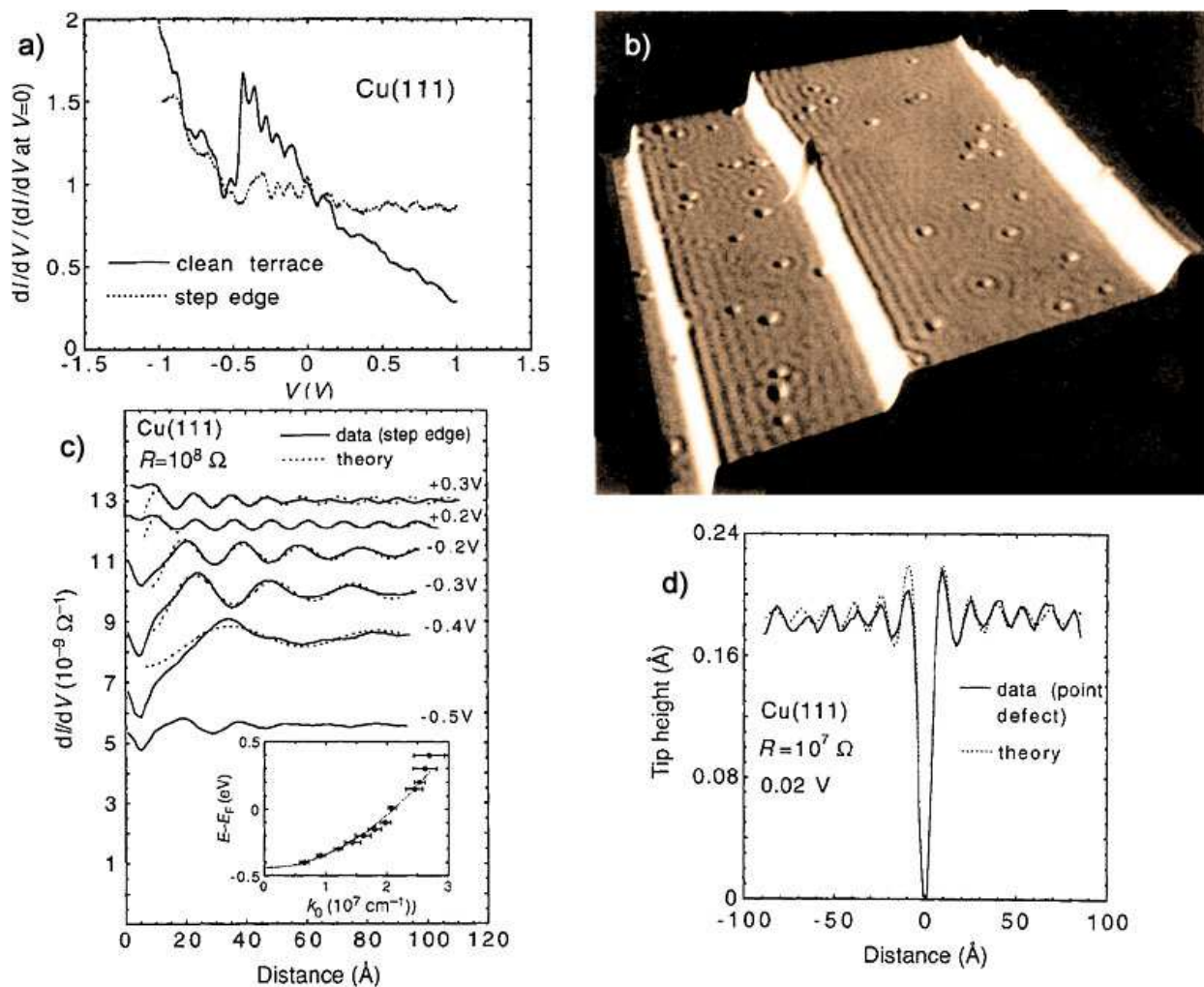
**Figure 2.2:** a) $dI/dV$ spectrum (normalized at $V = 0$) taken with a tip over a Cu(111) surface. A surface state onset is situated at 0.44 eV below the Fermi level. b) Constant current $500 \times 500 \text{Å}^2$ image of Cu surface ($V = 0.1$ V, $I = 1$ nA). Three monoatomic steps and about 50 point defects are visible. Spatial oscillations around steps and defects have a wavelength equal to $\sim 15$ Å. c) Solid lines: spatial dependence of $dI/dV$, measured as a function of distance from the step edge at different bias voltages. Dashed lines: theoretical fits of (2.14) to experimental data. Inset shows the surface state dispersion relation obtained from fits of (2.14) to $dI/dV$ data. d) Solid line: height of STM tip during linescan across the point defect ($V = 0.02$ V, $I = 2.0$ nA). Dashed line: a theoretical fit of equation (2.16) to dataset. The figure is adopted from [17].

to 30 Å. The corresponding wave vector equal to 2.09 Å$^{-1}$ is in a good agreement with the ARPES value from Table 1.1.

The LDOS oscillations around point defects on the Cu(111) surface can be similarly analyzed using a simple model of 2D free electron gas. If a point defect is considered as a cylindrically symmatric scattering potential, then the following expression for the LDOS can be derived [17]

$$\rho(x, E) \sim \frac{\sin(\delta_0)}{r} \cos(2kr + \delta_0),\tag{2.16}$$

where $\delta_0$ is a phase shift. Figure 2.2(d) shows a comparison of the STM linescan over a point defect with a theoretical curve. The best fit of the experimental data with (2.16) in assumption that the surface state band bottom lies at $-0.44$ eV below the Fermi energy gives the value of the phase shift $\delta_0$ equal to $-66°$. Such a phase shift corresponds to a scattering repulsive potential, in agreement with the appearance of point defects as dips on the surface [Fig. 2.2(b)].

## 2.3   Surface states confinement: a quantum laboratory

The work by Crommie et al. [17] evidenced that scattered and confined surface state electrons could be treated within simple models. Quantum confinement of surface state electrons as studied by STM/STS is obviously a very good illustration of quantum mechanics laws. Actually a number of research groups treated the systems they studied as a kind of a quantum laboratory [18, 19, 20, 21, 22].

### 2.3.1   Particle in the box model

Results of STM/STS measurements on surface state electrons confined to an island [18], to an vacancy hole [23, 20], to a step [19, 24] are often rationalized within one of the simplest models for electron behavior, the 1D particle-in-a-box model. In this model, the role of quantization becomes important in determining the energy eigenvalues of the electron. The confining potential $U(x)$ is finite only within a region $0 \leq x \leq L$ and is infinite outside

$$U(x) = \begin{cases} \infty & , & x < 0 \\ 0 & 0 \leq x \leq L \\ \infty & , & x > L. \end{cases}\tag{2.17}$$

Solution of the Schrödinger equation for such a system yields the following eigenfunctions $\Psi_n$ and eigenenergies $E_n$

$$\Psi_n(x) = \sqrt{\frac{2}{L}} \sin\left(\frac{n\pi x}{L}\right)\tag{2.18}$$

$$E_n = \frac{1}{2m} \left(\frac{\pi \hbar n}{L}\right)^2\tag{2.19}$$

The energy spectrum of the confined electron is quantized, only a discrete set of values is allowed. As a consequence, electron wave vectors are also quantized:

$$k_n = \sqrt{2mE_n/\hbar^2} = \pi n/L\tag{2.20}$$
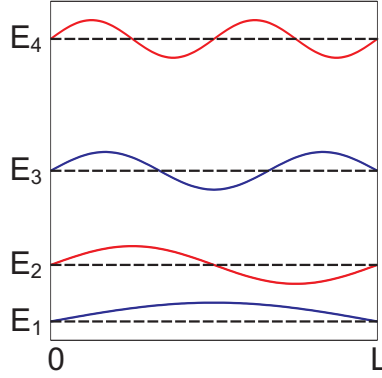
**Figure 2.3:** Eigenstates and eigenfunction of a particle-in-a-box model. Wavefunction parity depends on the energy level number $n$. Odd eigenfunctions are plotted with blue color, even – with red.

The set of allowed energies is scaled with $L$ proportionally to $L^{-2}$. The parity of wave functions $\Psi_n$ is determined by $n$, i.e wave functions with even $n$ are symmetric with respect to the center ($x = L/2$) of the potential well, and wave functions with odd $n$ are antisymmetric. Four first energy levels $E_n$ together with corresponding wave functions $\Psi_n$ are plotted in Fig. 2.3. Even and odd wave functions are drawn with blue and red colors respectively.

## 2.3.2   Confinement to islands

Li et al. [18] presented a quantitative STM/STS study of surface states on nanoscale Ag islands on Ag(111). Such close-packed islands grown on an Ag(111) surface are very stable structures, so standing waves can be observed over a wide range of voltages. Differential conductance maps taken above individual islands exhibited strongly voltage-dependent features. Figure 2.4 shows a typical series of differential conductance maps acquired above an island. Standing wave patterns appear at energies higher than $-65$ meV (the Ag(111) surface state band bottom energy). The standing waves may be identified as originating from surface state electrons, confined by the rapidly rising potential at the edges of the island. Simulated LDOS's of the 2D electron gas confined to the hexagonal potential well are demonstrated in the lower row of Fig. 2.4.

A typical STS spectrum taken with the STM tip positioned above the center of a hexagonal Ag island on Ag(111) with area 160 nm$^2$ is demonstrated in Fig. 2.5(a). Five peaks can be easily distinguished on the spectrum. The peaks correspond to energy levels of the confined surface state electrons broadened into resonances by single-particle scattering processes, many-body interactions, and instrumental effects such as thermal broadening [18]. The energy levels obtained in STS measurements were analyzed in terms of two-dimensional free electron gas confined within a hexagonal domain of potential $E_0$ bounded by infinitely high barriers. Experimental data and multiple scattering results for energies of the lowest two confined surface state levels at the center of variously sized hexagonal Ag islands on Ag(111) were found to be in a prefect agreement with a particle-in-a-box model [Fig. 2.5(b)]. The peak energies were found to conform to the scaling behavior (2.19) down to the smallest of island sizes.
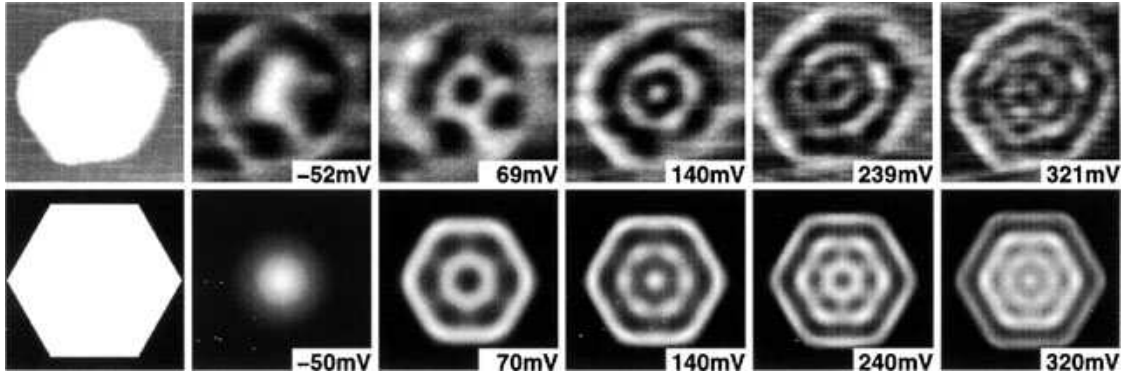
**Figure 2.4:** Upper row: topographic image of an approximately hexagonal Ag island on Ag(111) (area $\sim$ 94 nm$^2$), and a series of $dI/dV$ maps recorded at various bias voltages (at $T = 50$ K). Lower: geometry of a hexagonal box confining a two-dimensional electron gas, and the resulting local density of states. Experimental values have been used for the surface state onset $E_0$, electron effective mass $m^*$, and the island size. The calculations include a self-energy of $\Gamma = 0.2(E - E_0)$. The figure is taken from [18].
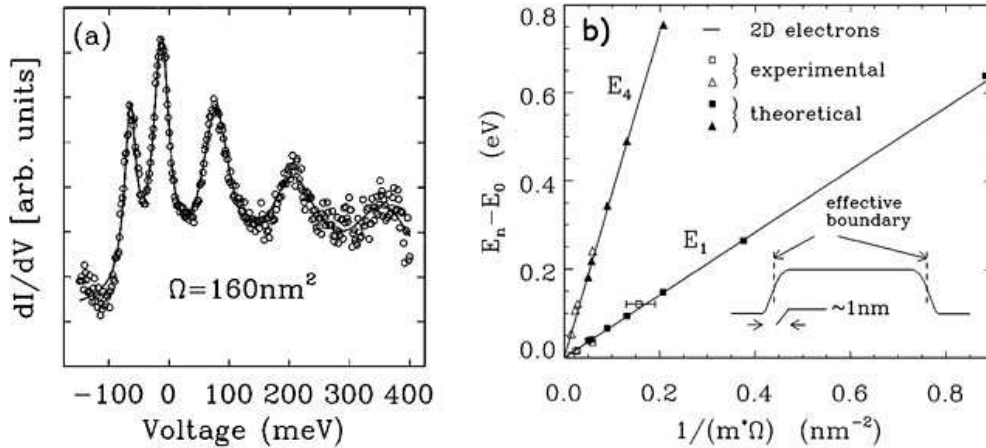


**Figure 2.5:** a) $dI/dV$ spectrum taken (at $T = 50$ K) with the STM tip positioned above the center of a hexagonal Ag island on Ag(111), area 160 nm$^2$. b) Energies of the lowest two confined surface state levels at the center of variously sized hexagonal Ag islands on Ag(111) as a function of renormalized inverse area. Comparison between measured energies (open symbols; error from experimental determination of the island size is indicated when larger than a symbol size), energies predicted by multiplescattering calculations (filled symbols), and the behavior expected of a perfectly confined two-dimensional electron gas (lines). Inset: measured topological cross section of an Ag island, along with the position identified as the effective boundary confining surface state electrons. The figure is adopted from [18].

### 2.3.3 Counting states in confined geometry

Rodary et al. [20] have recently demonstrated by means of STM/STS the quantization of the electron wave vector as it is stated by equation (2.20). This result was obtained by the Fourier analysis of the complete 2D map of the spatial modulation of the surface states confined to the vacancy craters on Cu(111) surface. A spatial modulation of the LDOS in a hexagonal crater of 20.5 nm size measured by STS is demonstrated in Fig 2.6(a). Corresponding 2D Fourier transforms (FT) exhibit two distinctive eigenvectors for the eigenstates at $-0.206$ V ($n = 10$) and $-0.156$ V ($n = 11$), which present simultaneously at $-0.176$ V. Figure 2.6(b) reveals that in contrast to the dispersion relation obtained at step edge [see, for instance, Fig. 2.2(c)], the dispersion relation of the confined system is a discontinuous curve. Although measurements are performed in steps of 10 mV, the absence of $k$ values within certain $k$ ranges was observed. Experimental data points were found to be always clustered around discrete, quantized $k$ values. The systematic analysis of surface states confined to craters of various sized figured out that the quantization of $k$ is determined by the lateral size of the crater. The larger was the crater, the denser was the spacing between the observed $k$ values. Actually the size of the crater known from STM images can be reinvented from the $n$-dependency of $k$. The inset of Fig. 2.6(b) shows $k$ as a function of $n$ for 13.5 nm and 22.5 nm craters. The slope of each curve calculated from (2.20) is exactly $\pi/L$, and it gives the crater sizes of 20.1 and 12.8 nm, respectively, in a very good agreement with topological STM measurements.

Previous works have ascribed maxima of $dI/dV$ spectra recorded at the center of the nanostructure to eigenstates. For hexagonal systems, the labeling scheme of observed states relies on an involved analysis [18]. These local $dI/dV$ measurements detect only a subset of eigenstates. Other eigenstates are accessible by measuring off center [25]. In contrast to the previous local STS analysis, the FT-based analysis exploits the complete two-dimensional LDOS modulation pattern within the nanostructure and, thus, reveals all eigenstates. These results show that each step of the discontinuous dispersion curve of the confined system of Fig. 2.6 gives rise to an extremum ( maximum or minimum ) of the density of states. This means that it is possible to identify the parity of each eigenstate. An even states have local $dI/dV$ minimum at the center of the island, and the odd states, vice versa, have maximum. This study offers a detailed understanding of the relation between quantized wave vectors, LDOS, and eigenstates of confined surface state.

### 2.3.4 Quantum corrals

A particle-in-a-box model is simple and at the same time qualitatively correct approach. But it can not account for the interaction between surface state electrons and impurity atoms, however, it is reasonable to assume that surface state scatter into the to bulk states at adatoms. In 1994 Heller et al. presented a combined theoretical and experimental description of the surface-state confinement to the $141 \times 285$ Å$^2$ quantum corral built of 76 Fe atoms on Cu(111) surface [26]. Artificial quantum corrals are structures with prescribed geometries, so they can be modeled in the experiment exactly one to one with minimal approximation of their structure. Heller et al. used in their model precise position of Fe atoms registered to the triangular grid of allowed binding sites of Cu(111) surface [26]. Experimental and theoretical LDOS near the Fermi energy in this corral are demonstrated in Fig. 2.7. To achieve such an agreement they introduced a complex phase shift $\eta = i\mu + \delta_0$
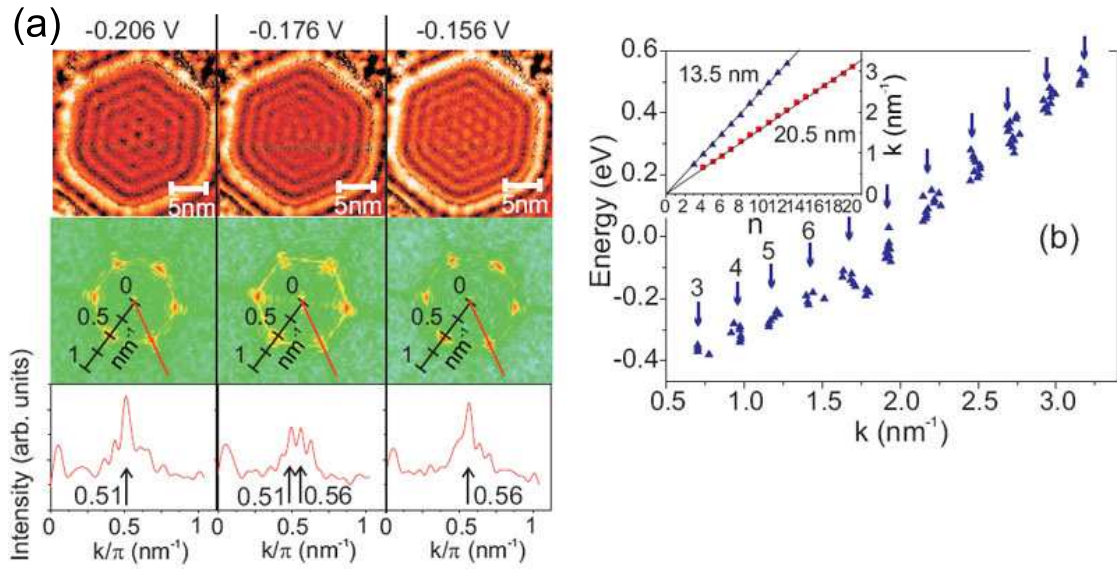
**Figure 2.6:** a) Spatial modulation of the LDOS in a hexagonal crater of 20.5 nm size, measured by STS at the indicated gap voltage $I = 1$ nA. The LDOS patterns at $-0.206$ and $-0.156$ V show different eigenstates. The central one is a superposition of these states. Central row: map of the Fourier transformation of the top LDOS patterns (red, high intensity; green, low intensity). Bottom row: Linescans through the FT maps along the red line. The linescan at the intermediate gap voltage $-0.176$ V shows the simultaneous presence of the two wave numbers $k = 0.51$ nm$^{-1}$, $0.56$ nm$^{-1}$ which characterizes two eigenstates at $-0.206$ and $-0.156$ V, respectively. b) Dispersion relation obtained by the FT analysis of the LDOS of a 13.5 nm crater. Note the discontinuous curves, where just discrete $k$ values are observed. The inset of reflects the quantization rule $k_n = n/L$. The first eigenstates are enumerated according to this rule. The figure is adopted from [20].
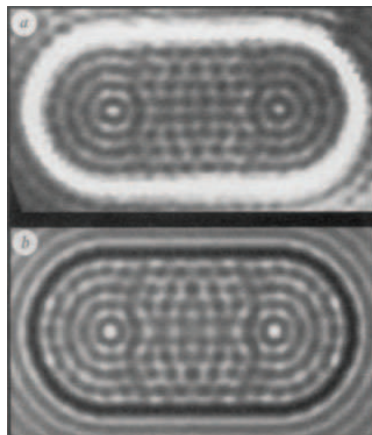


**Figure 2.7:** LDOS near $E_F$ for a 76 atom 'stadium' of dimensions $141 \times 285$ Å a) Experiment, bias voltage 0.01 V b) Theory The LDOS near the center of Fe adatoms is not accounted for in the theory and appears black. The figure is taken from [26]

in theoretical description and derived a new equation instead of (2.16)

$$\rho\left(x, E\right) \sim \mathfrak{Re}\left[\frac{\alpha_0 e^{2\mathrm{i}\delta_0} - 1}{2\mathrm{i}} \cdot \frac{e^{2\mathrm{i}kr}}{r}\right],\qquad(2.21)$$

where $\alpha_0 = e^{-\mu}$. Equation (2.16) can be derived from (2.21) at $\alpha_0 = 1$. The 'black body' case corresponds to $\alpha_0 = 0$. It is interesting to note that a standing wave pattern is created even in this case. Fitting of the experimental data to model (2.21) revealed that the corral walls transmit 25% of incident amplitude, reflect 25% and 50% is scattered into the bulk states. Further theoretical investigations on surface states confined to quantum corrals confirmed these experimental conclusions [27].

Manoharan et al. demonstrated that quantum corrals could be exploited to project electronic structure of adatom onto remote location [28]. They assembled an elliptical Co corral on Cu(111) surface and placed into one focus of the ellipse a magnetic Co atom. It is well known that circular wave emitted from the one focus of an ellipse is focused in the other one. Surface state of Cu(111) confined to elliptical quantum corral obey the same rule, so electronic structure surrounding Co adatom was coherently refocused onto the empty focus. A distinctive spectroscopical feature, known as many-particle Kondo resonance, was used to probe this effect [29, 30, 31, 32, 28, 33, 34]. The Kondo resonance, a signature of magnetic moment coupled to the sea of conduction electrons, was found in an empty focus [see Fig. 2.8]. This finding led to the Patent on method and system for information transfer and replication between spatially distinct points via engineered quantum states [US Patent 6441358].

Experiments of Manoharan et al. [28] on quantum mirages in quantum corrals inspired a number of theoretical works. Ab initio calculations performed by means of the KKR method for the elliptical corrals used by Manoharan et al. in their experiments unambiguously demonstrated that the spin polarization of the surface-state electrons caused by magnetic adatoms can be projected to a remote location and can be strongly enhanced in corrals, compared to an open surface [see Fig. 2.9] [35].

Adjustable geometries of quantum corrals open up wide range of possible theoretical treatments. In particular, it has been demonstrated that quantum corrals can permit to tailor the exchange interaction between magnetic adatoms at large separations [35, 36]. Corrals provide a convenient way to engineer eigenstates of the system [37, 38, 39]. This makes possible to create corrals with predefined electronic properties, for instance with multiple mirages with predefined relative intensities at specific locations [37]. Corrals are utilized to study surface state lifetimes [27, 21].
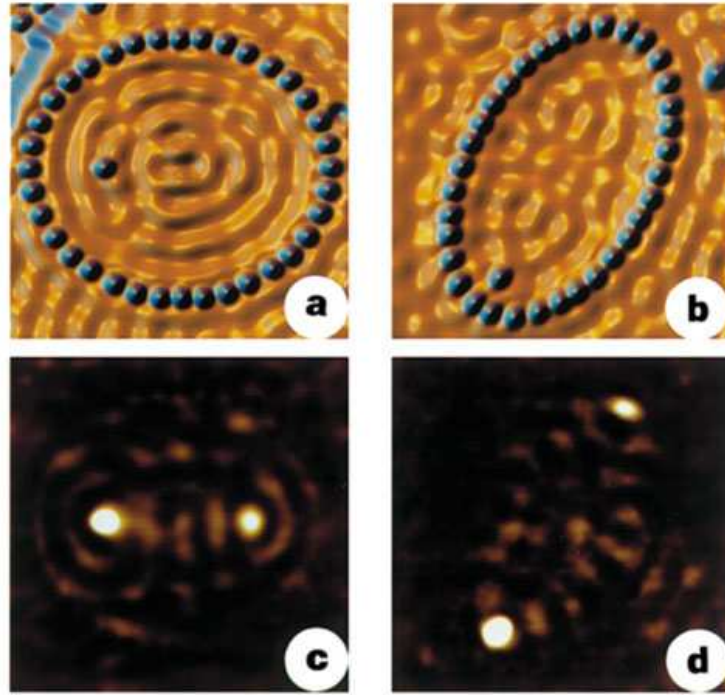
**Figure 2.8:** a), b), Topographs showing the eccentricity $e = 0.5$ (a) and $e = 0.786$ (b) ellipse each with a Co atom at the left focus. c), d), Associated $dI/dV$ difference maps showing the Kondo effect projected to the empty right focus, resulting in a Co atom mirage. The figure is adopted from [28]
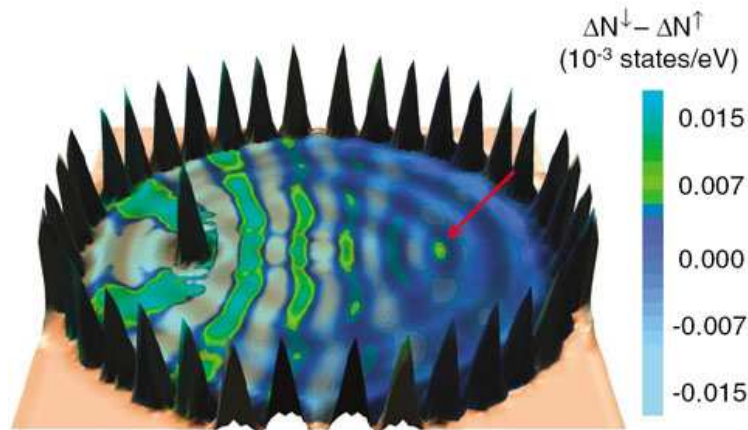


**Figure 2.9:** The LDOS at the Fermi energy on the Co adatom and the Co atoms of the corral walls are shown. The spin polarization of surface-state electrons inside the Co corral is presented in color: $\Delta N^{\downarrow}$ and $\Delta N^{\uparrow}$ are determined by the difference between LDOS near the Fermi energy (+10 meV) of the Co corral with the Co adatom, the empty Co corral, and the single Co adatom on the open Cu(111). The mirage in the empty focus is marked by the red arrow. The geometrical parameters of the corral are the same as in the experimental setup of Ref.[28], i.e., ellipse semiaxis $a = 71.3$ Å and eccentricity $e = 0.5$. The figure is taken from [35]

## 2.4 Surface state localization at adsorbates

Scattering of surface state electrons at impurities actually describes the system at scales comparable to the Fermi wave length of a surface state. The behavior of electrons at smaller scales, for example in tiny systems like adatoms or small clusters on surfaces, is determined by coupling between a surface state, bulk states and virtual bound states of nanostructures. Whenever a free electron gas is perturbed by an attractive potential, a bound state appears below the band bottom. The mathematical criterion of existence of such a state in 1D, 2D and 3D systems was proved by Simon [40]. In this section we at first illustrate the phenomenon by the basics of quantum mechanics and then proceed to a realistic theoretical model which can be directly compared to STS experiments.

The simplest model describing the phenomenon is a 1D free electron gas scattered at the attractive $\delta$-potential $U(x) = -a\delta(x)$. To find the energy of the bound state, note that for $E < 0$ momentum is purely complex [13]:

$$k = \frac{i}{\hbar}\sqrt{2m|E|}, \tag{2.22}$$

and the solution of the Schrödinger equation gives the decaying wave functions of the following form

$$\Psi(x) = \frac{\sqrt{ma}}{\hbar}e^{-ma|x|/\hbar^2}. \tag{2.23}$$

The only allowed bound state energy is situated below the band bottom:

$$E_{bound} = -\frac{ma^2}{2\hbar^2}. \tag{2.24}$$

Since surface state can be treated as a quasi-2D state, an atom adsorbed onto the surface should provoke the appearance of a bound state similarly to 1D case. On the other hand, for realistic description of the surface state localization at an adsorbate one should take into account the coupling between the surface and bulk states. This can be done using the extended Newns-Anderson model [41] describing a single adsorbate level of energy $\varepsilon_a$ interacting with the bulk Bloch states $|q\rangle$ and with the surface state $|k\rangle$. The Hamiltonian of such a system can be represented as

$$\hat{H} = \begin{pmatrix} \varepsilon_a & V_{aq} & \tilde{V}_{ak} \\ \tilde{V}_{aq} & \varepsilon_q & 0 \\ \tilde{V}_{ak}^* & 0 & \tilde{\varepsilon}_k \end{pmatrix}, \tag{2.25}$$

where $\varepsilon_q$ and $\tilde{\varepsilon}_k$ are submatrices of eigenenergies of the bulk and the surface states, respectively, while $V_{aq}$ and $\tilde{V}_{ak}$ are the elements of the coupling matrix. The LDOS $n_a(E)$ at the adsorbate atom can be expressed from the self-energy $\Sigma(E) = \Lambda(E) + i\Delta(E)$ of the system:

$$n_a(E) = \frac{1}{\pi}\frac{\Delta(E)}{\left(E - \epsilon_a - \Lambda(E)\right)^2 + \Delta^2(E)} \tag{2.26}$$

The imaginary part $i\Delta(E)$ of the self-energy $\Sigma(E)$ consists of contributions from the coupling of the adsorbate level to the bulk and the surface states. The bulk contribution $\Delta_b(E)$ is
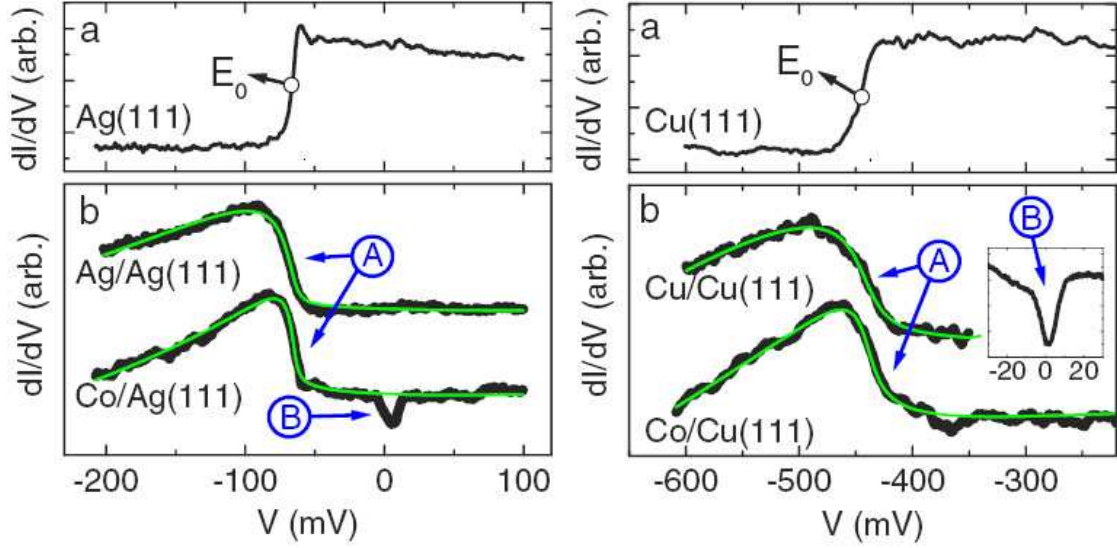
**Figure 2.10:** $dI/dV$ spectrums over flat Ag(111) surface (left panel) and Cu(111) (right panel) and over adatoms on those surfaces. Inset shows the Kondo-Fano resonance of Co adatom near Fermi level. Light-colored solid lines: ?fits to Newns-Anderson model described in the text. The figure is adopted from [41].

taken to be constant, and the surface-state contribution $\Delta_s(E)$ is governed by the step-like density of surface state:

$$\Delta(E) = \Delta_b(E) + \Delta_s(E) \tag{2.27}$$

$$\Delta_b(E) = \pi \sum_q |V_{aq}|^2 \delta(E - \varepsilon_q) = \delta_b \tag{2.28}$$

$$\Delta_s(E) = \pi \sum_k |V_{ak}|^2 \delta(E - \tilde{\varepsilon}_k) = \delta_s \Theta(E - E_0) \tag{2.29}$$

The real part $\Lambda(E)$ of the self-energy $\Sigma(E)$ can be expressed as a Hilbert transform of $\Delta(E)$

$$\Lambda(E) = \frac{\Delta_s}{\pi} \ln|E - E_0| + const \tag{2.30}$$

Detailed experimental studies of the surface state localization at adatoms have been conducted several years ago. Experiments by Limot et al. [41] and Olson et al.[42] revealed the existence of a resonance below the surface state onset energy, which was attributed to the split off bound state. $dI/dV$ spectra acquired over bare Ag(111) and Cu(111) surfaces have the only feature, the surface-state onset at $-0.067(1)$ eV for Ag(111) and $-0.445(1)$ eV for Cu(111) [Fig. 2.10]. The spectra taken above the atoms adsorbed on these surfaces significantly differ from cases of bare surfaces. The step-like feature at the surface state band bottom disappears but a new resonance arises below the surface state band bottom [Fig. 2.10]. Experiments demonstrated that this resonance was bound to adatoms and vanished at $\sim 10$ Å away from the adatom. The experimental data were modelled with the Newns-Anderson model (2.26). The results of fit are demonstrated in Fig. 2.10 by solid green lines. The agreement between the theory and the experiment is evident.

A number of theoretical methods were applied to study split-off bound state. Gauyacq et al. used a wave-packet propagation approach [43]. The experimental data of Limot et al.

were supported by the results of the extended Newns-Anderson model [44]. Several groups studied impurity-induced surface state localization by means of the ab initio Korringa-Kohn-Rostoker method [45, 46, 47]. The latter approach illustrated that magnetic impurities caused spin polarization of the surfrace states in their vicinity. Calculations performed for the Cu chains on Cu(111) surface resulted in the fact that increasing the size of the a nanostructure leads to dependency of split-off bound states on the position in a chain [45].

## 2.5 Spin-polarized surface states

### 2.5.1 Theoretical predictions on spin-polarized surface states on Co nanoislands on Cu(111)

In presence of magnetic thin films and/or nanoislands surface states on noble metal substrates turn spin-polarized. Co nanostructures grown on noble metal substrates are model system for studies of spin-polarized surface states [48, 49, 50, 51, 52, 53, 54, 55]. The first low temperature STM/STS observations of Co islands grown on Cu(111) substrate revealed two surface related electronic states [48]: a strong localized peak 0.31 eV below $E_F$ and a mainly unoccupied dispersive state, giving rise to quantum interference patterns of standing electron waves on the Co surface. *Ab initio* calculations revealed that the electronic states were spin polarized, originating from $d_{3z^2-r^2}$-minority and $sp$-majority bands, respectively [see Fig. 2.11].

The dispersive majority surface state was found to have a profound effect on the spin-polarization of the unoccupied states. Standing wave pattern shown in Fig. 2.11 were formed only by majority electrons, so the areas of standing waves with the increased electronic density had larger contribution of the majority states [50]. Ab initio calculations for equilateral triangular islands (Fig. 2.12(a) evidenced that the size of the island had a pronounced influence on the spatial distribution of the spin polarization of the Co islands. Those theoretical findings pointed out the possibility of modulating the spin polarization locally and energetically by engineering the shape and the size of the surface-deposited nanostructures.
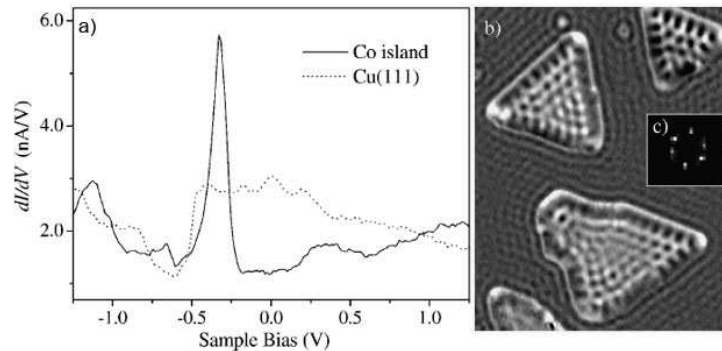


**Figure 2.11:** (a) STS spectra on 2 ML high Co nanoislands and on the bare Cu(111) surface taken with the same tip. (b) $dI/dV$ map of 2 ML high Co nanoislands on Cu(111). The scan range is 32 nm×41 nm and the tunneling parameters are $V = 0.5$ V, $I = 1.8$ nA. In the gray scale, brighter areas correspond to higher topography and larger LDOS, respectively. (c) Fourier spectrum of standing electron wave pattern on a Co island. The figure is adopted from [48]
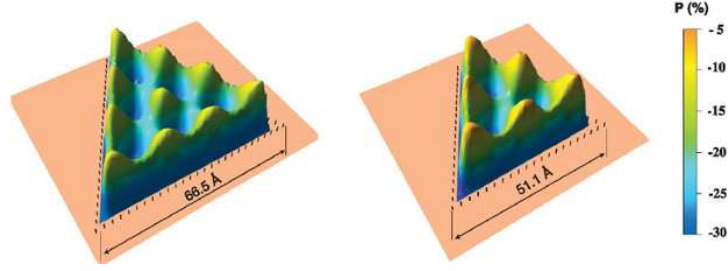
**Figure 2.12:** The spin polarization of surface-state electrons on triangular Co islands on Cu(111); calculations are performed for $E = 0.5$ eV above the Fermi level. The figure is taken from [50]
.

## 2.5.2   Basics of Spin-polarized STM

The contrast got in conventional STM is determined by the dependence of a shape and a strength of a tunneling barrier on the tip-sample distance and atomic species used. This technique permits to probe in the STM mode the topology of the sample and its DOS in the STS measurements. Suppose now that we probe a magnetic sample with a magentic tip. The magnetic moment originates from the different occupations for electrons of different spins. Imbalance in spin occupation is caused by the exchange interaction splitting up the majority and the minority states. Julliére found for a pair of ferromagnetic electrodes, that the tunneling current between them exhibited a significant dependence on the mutual orientation of the electrodes magnetization directions [56]. If we neglect any spin-dependence in the transmition through the barrier and assume that there is no spin-flip scattering during the tunneling process, then for small bias voltages, the tunneling conductance of the junction is determined by the electrons near the Fermi energy [57]. Since the density of spin-up and spin-down electrons are different, then the tunneling for parallel and antiparallel alignment of the electrodes magnetization are also different. Indeed, for the parallel orientation, the majority/minority electrons of the first electrode tunnel into majority/minority states of the second electrode, respectively. According to the Fermi golden rule, the conductance is proportional to the density $\rho$ of initial $(i)$ and final $(f)$ states at the Fermi level, and the total conductance of both spin channels can be expressed as [57]:

$$G_{\uparrow\uparrow} = \rho_\uparrow^i \rho_\uparrow^f + \rho_\downarrow^i \rho_\downarrow^f. \tag{2.31}$$

For the antiparallel orientation, majority electrons of the first electrode tunnel into the minority channel of the second electrode, and minority electrons tunnel, viceversa, to the majority channel:

$$G_{\uparrow\downarrow} = \rho_\uparrow^i \rho_\downarrow^f + \rho_\downarrow^i \rho_\uparrow^f. \tag{2.32}$$

The difference between conductances $G_{\uparrow\uparrow}$ and $G_{\downarrow\downarrow}$ is proportional to

$$\Delta G = G_{\uparrow\uparrow} - G_{\downarrow\downarrow} \sim \left( \rho_\uparrow^i - \rho_\downarrow^i \right) \left( \rho_\uparrow^f - \rho_\downarrow^f \right). \tag{2.33}$$

In general, for magnetic materials $\rho_\uparrow^i \neq \rho_\downarrow^i$ and $\rho_\uparrow^f \neq \rho_\downarrow^f$, so $\Delta G \neq 0$. Note, that paramagnetic materials exhibit no splitting and no occupation imbalance for majority and minority electrons, and therefore $\Delta G = 0$.

Slonczewski performed a detailed theoretical study of spin-polarized tunneling and derived a general formula [58] for the current between two magnetic electrodes with arbitrary aligned magnetizations:

$$I = I_0 \left( 1 + P^i P^f \cos\left(\Theta\right) \right), \tag{2.34}$$

where $\Theta$ is the angle between magnetizations of two electrodes, $P = \left(\rho_\uparrow - \rho_\downarrow\right) / \left(\rho_\uparrow + \rho_\downarrow\right)$ is the spin polarization. Equation (2.34) can also be used in the case when a small bias is applied and all the states between the two Fermi levels are involved in tunneling. Such a system is more complex, because tunneling probability can depend on energy and other parameters, but $G$ anyway can be calculated by means of some effective polarizations.

The tunneling current $I$ according to (2.34) increases if the second term in the brackets, i.e. $P^i P^f \cos\left(\Theta\right)$, is positive. It is the case for the tunneling between the states of the same spin-character for a parallel-oriented tip and sample magnetizations. If the magnetization alignment reverses, the cosine changes its sign and the tunneling current decreases. The sample LDOS, as shown by Tersoff and Haman, is proportional to the differential conductance $dI/dV$. The changes, the tunneling current gets due to TMR, affects also $dI/dV$ spectra. Comparison of spectra acquired at different magnetization alignments of tip and sample provides the access to the magnetic information.

### 2.5.3   SP-STM studies of Co nanoislands on Cu(111)

Pietzsch et al. studied by means of SP-STM Co nanoislands grown on Cu(111) [49, 51]. Co islands exhibit significant out of plane magnetization, so a Cr coated magnetic tip sensitive to the perpendicular component of the sample magnetization was used. Spectra were acquired on faulted and unfaulted Co islands with different magnetizations. The results are displayed in Fig. 2.13. Besides differences in spectra caused by islands stackings (red vs green curves in Fig. 2.13), for each island stacking order two distinct curves were observed for Co islands magnetized parallel and antiparallel to the tip magnetization direction (solid vs dotted curves in Fig. 2.13). It had found that, the Cr is negatively polarized around the Fermi level [59]. Taking the curves of higher intensities at the Co $d_z$ surface state as indicative of a parallel magnetization alignment (solid curves in Fig. 2.13), Pietzsch et al. concluded that that sample state was also negatively polarized [49], in agreement with theoretical prediction [48]. Tunneling of the majority dispersive state was, on the contrary, the most efficient for the antiparallel configuration. According to the theoretical description [50], only free-like sample majority electrons took part in the LDOS oscillations while localized minority d-like electrons did not. The effect of spin-polarization of the standing wave patters on Co nanoislands is illustrated in Fig. 2.14(b) by the $dI/dV$ profiles ( taken along lines as indicated in Fig. 2.14(a) for bias voltages being representative for ranges of inverse, balanced, and normal spin contrast. In each case the standing wave amplitude was found significantly larger on the antiparallel island, regardless of the sign of the bias dependent SP.
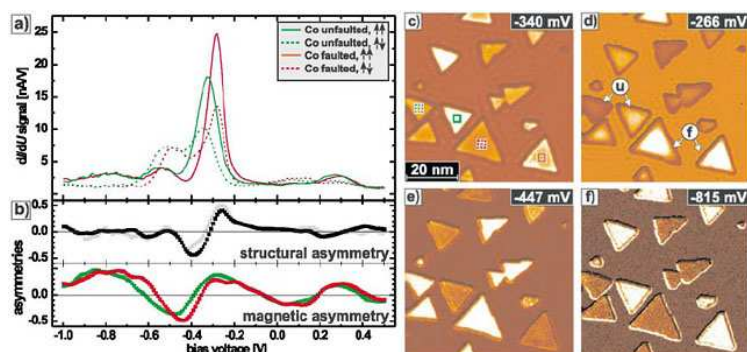
**Figure 2.13:** a) Spin-resolved tunneling spectra. Arrows ↑↑ (↑↓) refer to parallel (antiparallel) magnetization alignment of sample and tip. b) Asymmetries arising from different stacking [upper panel; grey (black) spin averaged (spin polarized)], and from opposite magnetization (lower panel). c-f) $dI/dV$ maps at bias voltages as indicated. Stabilization parameters: $I = 1$ nA, $V = 0.6$ V. The figure is adopted from [49].
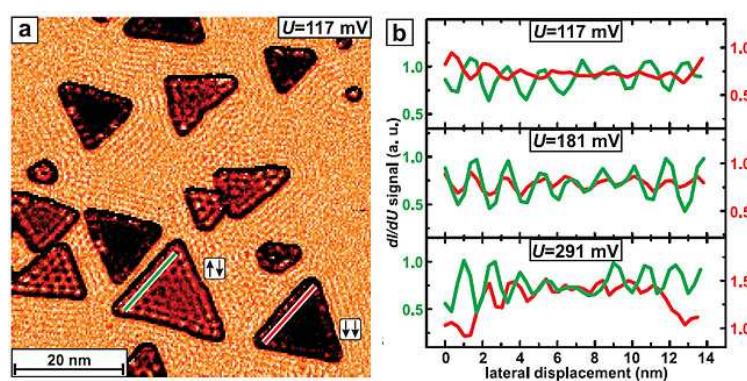


**Figure 2.14:** 0.6 ML Co on Cu(111). a)$dI/dV$ maps at sample bias voltages as indicated, showing standing wave patterns on both Cu substrate and Co islands. Arrows indicate islands being magnetized parallel (↑↑) or antiparallel (↑↓ ) to the tip magnetization. d) $dI/dV$ profiles taken along lines as indicated in a), at corresponding color coding. Regardless of the bias voltage, the standing wave amplitude is larger on the antiparallel island. The figure is adopted from [51].

# Goals of the work

Simple theoretical models presented in the introductory chapters can not provide a detailed, fully theoretical description of real systems and always need fitted parameters for input. Such kind of models practically can not help to study magnetic systems. In this work we focus on noble metal substrates decorated with low dimensional magnetic nanostructures like monatomic rows and thin films. We study such systems by means of ab initio calculations and make several generalizations on the behavior of spin-polarized surface states.

The following problems are addressed in this work:

- Surface state confinement on clean Cu(111) stepped surfaces.

- Origins and electronic structure of spin-polarized surface states arising on Cu(111) stepped surfaces decorated with 1D magnetic monatomic rows.

- Self organization of 1D nanostructures on Cu(111) stepped surfaces governed by surface states electrons.

- Development of Cu(111) surace state above magnetic Co clusters of increasing size, from a single adatom up to bilayer.

- Origin of spin-polarized surface states on Co bilayer on noble metal substrates.

- The impact of Co bilayer structure on spin-polarized surface states

- The role of substrate in the energetics of spin-polarized surface states on Co bilayer on noble metal substrates.

- The interplay between size-dependent strain of Co nanoislands on Cu(111) and their spin-polarized surface states.

# Chapter 3

# Methods used in the work

The Kohn-Sham density functional theory discussed in the first section of this chapter permits to substitute many-body problem with the single-particle one. The second section gives an insight into the Korringa-Kohn-Rostoker Green's function method for solution of the single-particle Kohn-Sham problem. Finally, some aspects of the atomic relaxations and structure optimizations are considered.

## 3.1 Density functional theory

The density functional theory (DFT) developed by Kohn and Hohenberg in 1964 [60] provides a way to treat ground state properties of a quantum many-body problem in terms of a single particle density. Such an approach can handle infinite periodic systems and nonperiodic systems consisting of about $10^3$ atoms. The paramount advantage of the DFT is that it is an *ab-initio* approach. Since its development, the DFT has been successfully applied to investigations of atoms, molecules, bulk and surafaces of solids. The present work also uses this approach within the framework of the Korringa-Kohn-Rostoker Green's function method.

### 3.1.1 Hohenberg - Kohn Theorems

The density functional theory rests on two theorems stating the possibility to completely describe ground state of a many body system through a single-particle electronic density [3, 60, 61, 62].

**Theorem 1** *For a nondegenerate ground state $\psi$, the external potential $v(\mathbf{r})$ is (within an additive constant) uniquely determined by the density distribution $\rho(\mathbf{r})$.*

The original theorem [60] was formulated for the one component, nondegenerate in the ground state system of spinless particles in the scalar and nonrelatevistic external potential. Later on, all these restrictions were relaxed and the theorem was considerably generalized. We will not describe all these theorems here but only refer to the literature [61, 62, 3].

**Theorem 2** *For a given $v(\mathbf{r})$ , the correct $\rho(\mathbf{r})$ minimizes the (nondegenerate) ground state energy, which is unique functional of $\rho(\mathbf{r})$.*

$$E\left[\rho\right] = \int dr v\left(r\right) \rho\left(r\right) + F\left[\rho\right],  \tag{3.1}$$

where $F\left[\rho\right]$ is the functional representing the sum of kinetic and Coulomb interaction energies. It can be written as

$$F\left[\rho\right] \equiv T_S\left[\rho\right] + \frac{1}{2}\int \frac{\rho\left(\mathbf{r}\right)\rho\left(\mathbf{r}'\right)}{\left|\mathbf{r} - \mathbf{r}'\right|}d\mathbf{r}d\mathbf{r}' + E_{xc}\left[\rho\right],  \tag{3.2}$$

where $T_S\left[\rho\right]$ is the kinetic energy of non-interacting electrons of density $\rho$, the second term is the classical electron-electron interaction density. If the last term, $E_{xc}\left[\rho\right]$ is completely neglected, one obtains the Hartree equations. The explicit many-body effects beyond the Hartree mean field approximation are encapsulated in the exchange-correlation functional $E_{xc}\left[\rho\right]$. The ground state energy and corresponding electronic density can be determined by minimizing (3.1) with respect to density.

## 3.1.2   Kohn-Sham equation

The minimization of the energy functional (3.1) can be performed by varying the density with the constraint that the number of electrons $N$ is fixed (i.e. $\int \rho\left(\mathbf{r}\right)d\mathbf{r} = N\left[\rho\right]$). The variational procedure is

$$\delta\left\{E\left[\rho\right]\right\} = 0  \tag{3.3}$$

or

$$\int d\mathbf{r}\delta\rho\left(\mathbf{r}\right)\left[\frac{\delta E\left[\rho\right]}{\delta\rho\left(\mathbf{r}\right)}\right] = 0.  \tag{3.4}$$

The constraint results in the condition $\int d\mathbf{r}\delta\rho\left(\mathbf{r}\right) = 0$, so the quantity in the square brackets in eq. (3.4) is a constant independent of $\mathbf{r}$. This gives the Euler-Lagrange equation:

$$\frac{\delta E\left[\rho\right]}{\delta\rho\left(\mathbf{r}\right)} = \mu,  \tag{3.5}$$

where $\mu$ is the chemical potential. Taking into account equations (3.1), (3.2):

$$\frac{\delta T_s\left[\rho\right]}{\delta\rho\left(\mathbf{r}\right)} + v_{eff}\left(\mathbf{r}\right) = \mu,  \tag{3.6}$$

where $v_{eff}\left(\mathbf{r}\right)$ is an effective one-body potential:

$$v_{eff}\left(\mathbf{r}\right) = v\left(\mathbf{r}\right) + \int \frac{\rho\left(\mathbf{r}'\right)}{\left|\mathbf{r} - \mathbf{r}'\right|}d\mathbf{r}' + v_{xc}\left[\rho\left(\mathbf{r}\right)\right],  \tag{3.7}$$

and the many body effect is accounted in a single-particle problem through the functional derivative $v_{xc}$:

$$v_{xc}\left[\rho\left(\mathbf{r}\right)\right] = \frac{\delta E_{xc}\left[\rho\right]}{\delta\rho\left(\mathbf{r}\right)}.  \tag{3.8}$$

Now the ground state electronic density can be determined as the self-consistent solution of the Schrödinger-like equation for the motion of a particle in the effective potential $v_{eff}\left(\mathbf{r}\right)$. This equation is called the Kohn-Sham equation:

$$\left\{-\frac{\hbar^2}{2m}\nabla^2 + v\left(\mathbf{r}\right) + \int \frac{\rho\left(\mathbf{r}'\right)}{\left|\mathbf{r} - \mathbf{r}'\right|}d\mathbf{r}' + v_{xc}\left(\mathbf{r}\right)\right\}\psi_k\left(\mathbf{r}\right) = \epsilon_k\psi_k\left(\mathbf{r}\right),  \tag{3.9}$$

where density is defined through the wave functions $\psi_k(\mathbf{r})$ as

$$\rho(\mathbf{r}) = \sum_{k=1}^{N} |\psi_k(\mathbf{r})|^2. \tag{3.10}$$

Note, that, according to Hohenberg-Kohn theorems, only overall electronic density (3.10) describes a real physical system. The standalone single-particle wave functions $\psi_k(\mathbf{r})$ describe some quasiparticles without a direct physical meaning. The overall electronic density (3.10), on the one hand, is defined by the solutions $\psi_k(\mathbf{r})$ of the Kohn-Sham equation (3.9), and on the other hand, it is included into the Kohn-Sham Hamiltonian. This means that problem (3.9) must be solved self-consistently.

### 3.1.3  The local density approximation

$$E_{xc}[\rho(\mathbf{r})] = \int \rho(\mathbf{r}) \varepsilon_{xc}^{hom}(\rho(\mathbf{r})) \, d\mathbf{r}. \tag{3.11}$$

The exchange–correlation potential in local density approximation (LDA) is expressed as:

$$v_{exc}(\mathbf{r}) = \frac{d}{d\rho} \{\varepsilon_{xc}(\rho) \cdot \rho(\mathbf{r})\} \equiv v_{xc}(\rho). \tag{3.12}$$

Then the total energy in the LDA can be recast as:

$$E \approx \sum_i \varepsilon_i - \frac{1}{2} \int d\mathbf{r} d\mathbf{r}' \frac{\rho(\mathbf{r})\rho(\mathbf{r}')}{|\mathbf{r} - \mathbf{r}'|} + \int d\mathbf{r} \rho(\mathbf{r}) \{\varepsilon_{ex}(\rho) - v_{ex}(\rho)\}. \tag{3.13}$$

Thus by a local approximation the problem of exchange and correlation in an inhomogeneous system is reduced to calculating the exchange–correlation energy density $\epsilon_{ex}(\rho)$ of a homogeneous electron gas [3, 61, 62]. However, the LDA is assumed to be the most suitable for systems with slowly varying density, it has been found to be surprisingly accurate in description of other cases.

## 3.2  Green's function KKR method

In the previous section the DFT has been proposed as a rather simple way to solve many-body quantum problems. It has been shown that all exchange-correlation effects can be encapsulated into the effective potential depending on the electronic density. The corresponding self-consistent problem is described by the Kohn-Sham equation (3.9). In this chapter we outline the possibility to solve this equation for an arbitrary case, including infinite periodic lattices, surfaces and clusters. In this respect, two general approaches to the solution of the Kohn-Sham equation can be distinguished.

The first approach is actually the frontal attack of the Kohn-Sham problem (3.9). The electronic density is determined from the solutions $\psi_k$ ((3.10)) of the Kohn-Sham equation (3.9). The usual mathematical technique applied to obtain $\psi_k$ is to expand them on some basis set $\phi_p^{basis}$ and solve the obtained secular equation in order to get expansion coefficients. This technique is used in the following methods: local combination of atomic orbitals (LCAO), pseudopotential method, the augmented plane wave (APW) method, the linearized augmented plane wave method (LAPW ) and some others [2, 3].

The second approach doesn't deal with quasi-particle wave functions, but exploits the properties of the Green's function to find the electronic density. This technique was developed by Korringa [63], Kohn and Rostoker [64] and called the Korringa-Kohn-Rostoker (KKR) Green's function method. However this method is tangled from the mathematical point of view, it allows to describe electronic properties of large and complicated systems. In particular, this method successfully describes both surface states arising on metal surface and their changes due to scattering at nanostructures on the surface.

This section is aimed to explain the basics of the KKR Green's function method. For this purpose the following sequence was decided upon: We start from the relation between the Green's function of the system and its electronic properties. Then we pass over to expressing the Green's function (and therefore electronic properties) of the perturbed system through the unperturbed one. Further on, we consider the scattering of the electron at a single spherical potential and multiple scattering at a collection of such potentials. And finally the KKR method workflow closes the section.

### 3.2.1   Green's function and its properties

Usually quantum systems are described by their Hamiltonians $\hat{\mathcal{H}}$. In our case we use Kohn-Sham Hamiltonian $\hat{\mathcal{H}}_{KS}$ [see eq. (3.9)]. The Kohn-Sham Hamiltonian is a linear differential operator and therefore its energy-dependent Green's function can be defined in spectral representation [62, 65, 66]:

$$\left(\hat{\mathcal{H}}_{KS} - E\right)\hat{\mathcal{G}}\left(E\right) = \hat{\mathcal{I}}, \tag{3.14}$$

where $\hat{\mathcal{I}}$ is a unitary operator, or in real-space representation:

$$\left(\hat{\mathcal{H}}_{KS} - E\right)G\left(\mathbf{r}, \mathbf{r}', E\right) = \delta\left(\mathbf{r} - \mathbf{r}'\right), \tag{3.15}$$

where $\delta$ is the Dirac delta function. The singularities of $G\left(\mathbf{r}, \mathbf{r}', E\right)$ determine the eigenvalue spectrum. $G\left(\mathbf{r}, \mathbf{r}', E\right)$ has poles at the eigenenergies of the bound states and a brunch cut along the energies of continuous spectrum. $G\left(\mathbf{r}, \mathbf{r}', E\right)$ is an analytical function of $E$ if $\mathfrak{Im}E > 0$. One should take it into account when choosing a contour for integration over energies. If $\psi_i\left(\mathbf{r}\right)$ and $\epsilon_i$ are eigenvectors and eigenvalues of eigenvalue problem $\hat{\mathcal{H}}_{KS}\psi_i\left(\mathbf{r}\right) = \epsilon_i\psi_i\left(\mathbf{r}\right)$, then $G\left(\mathbf{r}, \mathbf{r}', E\right)$ can be constructed from the complete set of eigenvectors and corresponding eigenvalues:

$$G\left(\mathbf{r}, \mathbf{r}', E\right) = \lim_{\gamma \to 0}\sum_{i=0}^{\infty}\frac{\psi\left(\mathbf{r}\right)\psi^*\left(\mathbf{r}'\right)}{E + \mathfrak{i}\gamma - \epsilon_i}. \tag{3.16}$$

The Green's function contains all the information on the electronic density of states in the system. Indeed, the local density of states $\rho\left(\mathbf{r}, E\right)$ can be expressed through the probability density of all the states with energy $E$ at the point $\mathbf{r}$:

$$\rho\left(\mathbf{r}, E\right) = \sum_{i=0}^{\infty}\delta\left(\epsilon_i - E\right)\psi\left(\mathbf{r}\right)\psi^*\left(\mathbf{r}\right). \tag{3.17}$$

With a help of the Dirac equality [65]

$$\lim_{\gamma \to 0}\frac{1}{x \pm \mathfrak{i}y} = P\left(\frac{1}{x}\right) \mp \mathfrak{i}\pi\delta\left(x\right) \tag{3.18}$$

the energy-resolved local density of states can be expressed from the Green's function: [62, 65, 66]

$$\rho(\mathbf{r}, E) = -\frac{1}{\pi} \Im m G(\mathbf{r}, \mathbf{r}, E). \tag{3.19}$$

It is necessary to recall here that the goal of the DFT framework is to find a ground state electronic density $\rho(\mathbf{r})$. It is clear that this density can be found as the imaginary part of the Green's function integrated over energy:

$$\rho(\mathbf{r}) = -\frac{1}{\pi} \Im m \int_{-\infty}^{E_F} G(\mathbf{r}, \mathbf{r}, E) \, dE. \tag{3.20}$$

### 3.2.2 The Dyson equation

Solving the Kohn-Sham equation (3.9) one deals with the self-consistent problem, so the Green's function does not only define the electronic density but also depends on it. On the other hand the only part of the Kohn-Sham Hamiltonian depending on $\rho(\mathbf{r})$ is the effective potential. This fact immediately leads us to the idea of representing a Hamiltonian $\hat{\mathcal{H}}$ in terms of an unperturbed part $\hat{\mathcal{H}}_0$ and a Hermitian perturbation $\hat{\mathcal{V}}$:

$$\hat{\mathcal{H}} = \hat{\mathcal{H}}_0 + \hat{\mathcal{V}}. \tag{3.21}$$

The Hamiltonian (3.21) describes, for instance, scattering of electrons at perturbing potential $V$. Applying equation (3.14) both to perturbed $\hat{\mathcal{H}}$ and unperturbed $\hat{\mathcal{H}}_0$ Hamiltonians one obtains the Dyson equation linking the corresponding Green's functions $\hat{\mathcal{G}}(E)$ and $\hat{\mathcal{G}}_0(E)$:

$$\begin{aligned} \hat{\mathcal{G}}(E) &= \hat{\mathcal{G}}_0(E) + \hat{\mathcal{G}}(E) \hat{\mathcal{V}} \hat{\mathcal{G}}_0(E) \\ &= \hat{\mathcal{G}}_0(E) + \hat{\mathcal{G}}_0(E) \hat{\mathcal{V}} \hat{\mathcal{G}}(E). \end{aligned} \tag{3.22}$$

### 3.2.3 Single site T-operator

The Dyson equation (3.22) can be reformulated in order to contain only the unperturbed Green's function $\hat{\mathcal{G}}_0(E)$ on the right hand side

$$\hat{\mathcal{G}}(E) = \hat{\mathcal{G}}_0(E) + \hat{\mathcal{G}}_0(E) \left\{ \hat{\mathcal{V}} + \hat{\mathcal{V}} \hat{\mathcal{G}}_0 \hat{\mathcal{V}} + \hat{\mathcal{V}} \hat{\mathcal{G}}_0 \hat{\mathcal{V}} \hat{\mathcal{G}}_0 \hat{\mathcal{V}} + \ldots \right\} \hat{\mathcal{G}}_0(E). \tag{3.23}$$

The term in the figure brackets is called *T-operator*.

$$\hat{\mathcal{T}} = \hat{\mathcal{V}} + \hat{\mathcal{V}} \hat{\mathcal{G}}_0 \hat{\mathcal{V}} + \hat{\mathcal{V}} \hat{\mathcal{G}}_0 \hat{\mathcal{V}} \hat{\mathcal{G}}_0 \hat{\mathcal{V}} + \ldots . \tag{3.24}$$

With the *T-operator* the Dyson equation takes on the following form

$$\hat{\mathcal{G}} = \hat{\mathcal{G}}_0 + \hat{\mathcal{G}}_0 \hat{\mathcal{T}} \hat{\mathcal{G}}_0. \tag{3.25}$$

If only a single perturbation $\hat{\mathcal{V}}$ is present in the system, the corresponding *T-operator* is called *single-site T-operator* and usually denoted by $\hat{t}$. The following equation for a single-site T-operator can be easily derived from (3.24) [67, 62, 65, 66]:

$$\begin{aligned} \hat{t} &= \hat{\mathcal{V}} + \hat{\mathcal{V}} \hat{\mathcal{G}}_0 \hat{t} \\ &= \left( \hat{\mathcal{I}} - \hat{\mathcal{V}} \hat{\mathcal{G}}_0 \right)^{-1} \hat{\mathcal{V}} \end{aligned} \tag{3.26}$$

The T-operator can be used to express the eigenfunctions $\psi_i$ of the perturbed Hamiltonian $\hat{\mathcal{H}}_0 + V$ through the eigenfunctions $\phi_i$ of the ideal Hamiltonian $\hat{\mathcal{H}}_0$. Indeed, if

$$\left(\epsilon\hat{\mathcal{I}} - \hat{\mathcal{H}}_0\right)\phi_i = 0$$
$$\left(\epsilon\hat{\mathcal{I}} - \hat{\mathcal{H}}_0\right)\psi_i = \hat{\mathcal{V}}\psi_i,$$

then for $\psi_i = \phi_i + \delta\psi_i$ the following expression can be derived:

$$\left(\epsilon\hat{\mathcal{I}} - \hat{\mathcal{H}}_0 - \hat{\mathcal{V}}\right)\delta\psi_i = \hat{\mathcal{V}}\phi_i. \tag{3.27}$$

Applying the definition of the Green's function (3.14) to the above equation immediately yields

$$\psi_i = \phi_i + \hat{\mathcal{G}}\hat{\mathcal{V}}\phi_i \tag{3.28}$$

or taking into account the definition of the T-operator (3.26)

$$\psi_i = \phi_i + \hat{\mathcal{G}}_0\hat{t}\phi_i. \tag{3.29}$$

The last two equations are called the Lippmann-Schwinger equations [62, 65, 66].

The *T-operator* can be used to describe the change of integrated density of states $\Delta\rho\left(E\right)$ between the perturbed and the unperturbed systems due to scattering of electrons at a perturbing potential

$$\Delta\rho\left(E\right) = \frac{1}{\pi}\mathfrak{Im}Tr\left(\ln\hat{t}\left(E\right)\right) \tag{3.30}$$

The above expression is usually referred to as the *Lloyd's formula* [62, 65, 66].

### 3.2.4   Multiple-site T operator

In a general case of an ensemble of $N$ scatterer the total potential $V\left(\mathbf{r}\right)$ can be considered as a sum of individual potentials $V_i\left(\mathbf{r}\right)$ nonzero only in corresponding disjoint domains $D_{V_i} \in \mathsf{R}^3$:

$$V\left(\mathbf{r}\right) = \sum_{i=1}^{N} V_i\left(\mathbf{r}\right) \tag{3.31}$$

$$V_i\left(\mathbf{r}\right) \neq 0, \ \mathbf{r} \in D_{V_i}, \ D_{V_i} \cap D_{V_j} = \delta_{ij}D_{V_i}$$

The multiple-site *T-operator* $T_{ms}$ for the potential (3.31) can be introduced similar to the single site t-operator (see equation (3.23) and (3.24)) [67, 62, 65, 66]. Taking into account the expression (3.26) we obtain the following relation

$$\begin{aligned}\hat{\mathcal{T}}_{ms} = \quad & \sum_i \hat{t}_i + \\ + \; & \sum_{i,j} \hat{t}_i\hat{\mathcal{G}}_0\left(1-\delta_{ij}\right)\hat{t}_j + \\ + \; & \sum_{i,j,k} \hat{t}_i\hat{\mathcal{G}}_0\left(1-\delta_{ij}\right)\hat{t}_j\hat{\mathcal{G}}_0\left(1-\delta_{jk}\right)\hat{t}_k + \\ + \; & \sum_{i,j,k,n} \hat{t}_i\hat{\mathcal{G}}_0\left(1-\delta_{ij}\right)\hat{t}_j\hat{\mathcal{G}}_0\left(1-\delta_{jk}\right)\hat{t}_k\hat{\mathcal{G}}_0\left(1-\delta_{kn}\right)\hat{t}_n + \\ + \; & \dots. \end{aligned} \tag{3.32}$$
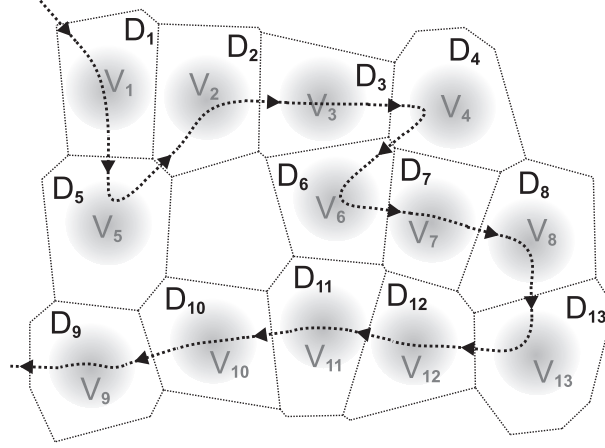
**Figure 3.1:** A sketch of a multiple scattering of an electron in a system of individual potentials nonzero in corresponding space domains separated by the thin dashed borders. Only one multiple scattering process is shown. The Green's function of the system (and therefore its electronic structure) is determined by all possible multiple scattering processes. Figure is inspired by [67].

The first sum corresponds to a single scattering at each potential $V_i(\mathbf{r})$. The second sum over $i, j$ describes the double scattering at first at potential $V_i$ and then at potential $V_j$. The third sum accounts the triple scattering, the forth is used for the quatro-scattering and so on. A multiple-scattering sequence is shown schematically in Figure 3.1. The Green's function of the system (and therefore its electronic structure) is determined by all possible multiple scattering processes.

### 3.2.5 Structural Green's function

Now let us assume that an electron gets to some space domain $D_{V_i}$ from another domain $D_{V_j}$. According to the equation (3.32) it can follow different paths crossing a number of domains on its way. If all possible paths between domains $D_{V_i}$ and $D_{V_j}$ are considered, the on-way perturbations are completely described. Mathematically it is defined by the scattering-path operator (SPO) $\hat{\tau}^{ij}$ [66]:

$$
\begin{aligned}
\hat{\tau}^{ij} = \quad & \hat{t}_i \delta_{ij} + \\
+ \quad & \hat{t}_i \hat{\mathcal{G}}_0 (1 - \delta_{ij}) \hat{t}_j + \\
+ \quad & \sum_k \hat{t}_i \hat{\mathcal{G}}_0 (1 - \delta_{ik}) \hat{t}_k \hat{\mathcal{G}}_0 (1 - \delta_{kj}) \hat{t}_k + \\
+ \quad & \sum_{k,n} \hat{t}_i \hat{\mathcal{G}}_0 (1 - \delta_{ik}) \hat{t}_k \hat{\mathcal{G}}_0 (1 - \delta_{kn}) \hat{t}_n \hat{\mathcal{G}}_0 (1 - \delta_{nj}) \hat{t}_j + \\
+ \quad & \dots
\end{aligned}
\tag{3.33}
$$

or

$$
\begin{aligned}
\hat{\tau}^{ij} &= \hat{t}_i \delta_{ij} + \sum_k \hat{t}_i \hat{\mathcal{G}}_0 (1 - \delta_{ik}) \hat{\tau}^{kj} \\
&= \hat{t}_i \delta_{ij} + \sum_k \hat{\tau}^{ik} \hat{\mathcal{G}}_0 (1 - \delta_{kj}) \hat{t}_j.
\end{aligned}
\tag{3.34}
$$

The multiple scattering T-operator is equal to the sum of SPOs between all the domains in the system

$$\hat{\mathcal{T}}_{ms} = \sum_{i,j} \hat{\tau}^{ij},$$

(3.35)

so the multiple-scattering Dyson equation (3.22) can be written in terms of SPOs

$$\hat{\mathcal{G}} = \hat{\mathcal{G}}_0 + \sum_{i,j} \hat{\mathcal{G}}_0 \hat{\tau}^{ij} \hat{\mathcal{G}}_0$$

(3.36)

The first term in the equations (3.33) and (3.34) describes the single-site *T-operator* $\hat{t}_i$ of the domain $D_{V_i}$. If we want to express the perturbation induced by the structure of our system (which is described by spatial configuration of domains $D_{V_j}$), the rest terms must be considered. Thus equation (3.33) transforms into

$$\hat{\tau}^{ij} = \hat{t}_i \delta_{ij} + \hat{t}_i \underline{\hat{\mathcal{G}}}^{ij} \hat{t}_j,$$

(3.37)

where $\underline{\hat{\mathcal{G}}}^{ij}$ is so-called *structural Green's function*:

$$\underline{\hat{\mathcal{G}}}^{ij} = \hat{\mathcal{G}}_0 \left(1 - \delta_{ij}\right) + \sum_{k,l} \hat{\mathcal{G}}_0 \left(1 - \delta_{ik}\right) \hat{\tau}^{kl} \hat{\mathcal{G}}_0 \left(1 - \delta_{lj}\right).$$

(3.38)

The representation of the Green's function $\hat{\mathcal{G}}$ of the system with multiple perturbating potentials follows from the equations (3.36) and (3.37):

$$\hat{\mathcal{G}} = \hat{\mathcal{G}}^i \delta_{ij} + \sum_{i,j} \hat{\mathcal{G}}_0 \hat{t}_i \underline{\hat{\mathcal{G}}}^{ij} \hat{t}_j \hat{\mathcal{G}}_0,$$

(3.39)

where $\hat{\mathcal{G}}^i$ are Green's functions (3.25) of the single-site scattering problem for the domain $V_i$. In such a formulation the properties of the individual scattering potentials described by the single-site Green's functions $\hat{\mathcal{G}}^i$ are separated from their geometrical arrangement, described by the structural Green's function $\underline{\hat{\mathcal{G}}}^{ij}$ [62, 65, 66].

### 3.2.6   Fundamental KKR equation

Equations (3.34) and (3.36) can be reformulated in terms of supermatrices. If the following supermatrices are defined [62, 66, 67]:

$$\begin{aligned}
\underline{\hat{\mathbf{G}}} &= \left\{ \underline{\hat{\mathcal{G}}}^{ij} \right\}, \\
\hat{\mathbf{t}} &= \left\{ \hat{t}_i \delta_{ij} \right\}, \\
\hat{\mathbf{G}}_0 &= \left\{ \hat{\mathcal{G}}_0 \left(1 - \delta_{ij}\right) \right\}, \\
\hat{\tau} &= \left\{ \hat{\tau}^{ij} \right\},
\end{aligned}$$

(3.40)

then equations (3.37) and (3.38) transform into:

$$\hat{\tau} = \left( \hat{\mathbf{t}}^{-1} - \hat{\mathbf{G}}_0 \right)^{-1},$$

(3.41)

$$\underline{\hat{\mathbf{G}}} = \hat{\mathbf{G}}_0 \left( \hat{\mathbf{I}} - \hat{\mathbf{t}} \hat{\mathbf{G}}_0 \right)^{-1}.$$

(3.42)
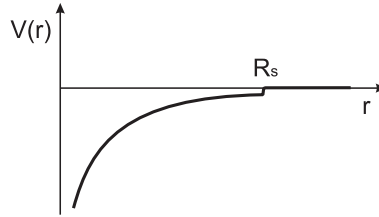
**Figure 3.2:** Approximation of an spherically symmetric potential of finite radius $r_s$. Outside the radius $r_s$ the potential is zero.

Equations (3.41) and (3.42) are very often called the fundamental equations of the Multiple Scattering Theory. The electronic eigenvalues are completely defined by the singularities of the Green's function of the perturbed system. To find them one has to find conditions vanishing the determinant:

$$\det\left[\hat{\mathbf{t}}^{-1} - \hat{\mathbf{G}}_{\mathbf{0}}\right] = 0. \tag{3.43}$$

### 3.2.7   Scattering at a single spherical potential

We have not suggested the form of the perturbing effective potential $V_{eff}$. Now we turn to the description of the KKR representations of the Green's function and the Dyson equation.

The potential of an ideal crystal is invariant to translations with arbitrary lattice vectors $\mathbf{R}_i$:

$$V_{eff}\left(\mathbf{r} + \mathbf{R}_i\right) = V_{eff}\left(\mathbf{r}\right). \tag{3.44}$$

Defects in crystalls reduce this symmetry. Following equation (3.31) the crystal volume can be divided into the disjoint space domains. Each space domain coinsides with the corresponding Wigner-Seits cell and is associated with the charge-neutral atom situated at this cell. In the simplest approximation, the potential inside each space domain can be assumed to be spherically symmetric and nonzero only inside a sphere of some radius $r_s$ [see Figure 3.2]:

$$V_{eff}\left(r\right) = \begin{cases} V_i\left(r\right), & r \leq r_s \\ 0, & r > r_s \end{cases} \tag{3.45}$$

There are two main approximations defining the radius $r_s$: the *Muffin-Tin* (MT) and *atomic sphere* (ASA) approximations. In the MT approximation radiuses are chosen to construct a system of touching nonoverlapping spheres. In the ASA, the volume of each sphere is chosen to be equal to the volume of the corresponding Wigner-Seits cell. In this case the adjacent spheres overlap.

The Kohn-Sham equation (3.9) for a single spherical symmetric potential (3.45) transforms into [68, 69, 67]:

$$\left[-\frac{\partial^2}{\partial r^2} + \frac{\ell\left(\ell + 1\right)}{r^2} + V\left(r\right) - \epsilon\right] r F_\ell\left(r, \epsilon\right) = 0. \tag{3.46}$$

The eigenfunctions of equation (3.46) can be represented by the product of spherical harmonics $Y_{\ell m}\left(\theta, \phi\right) \equiv Y_L\left(\hat{\mathbf{r}}\right)$ and radial wavefunctions $F_\ell\left(r, \epsilon\right)$ [68, 69, 67, 62, 65, 66]. For each energy $\epsilon$ and angular momentum $\ell$ there are two linear independent solutions:

- the regular physical solution

$$R_L\left(\mathbf{r}, \epsilon\right) = R_\ell\left(r, \epsilon\right) Y_L\left(\hat{\mathbf{r}}\right), \tag{3.47}$$

$$R_L\left(\mathbf{r}, \epsilon\right) \sim r^\ell, \; r \to 0;$$

- and the irregular solution diverging at the origin:

$$H_L\left(\mathbf{r}, \epsilon\right) = H_\ell\left(r, \epsilon\right) Y_L\left(\hat{\mathbf{r}}\right), \tag{3.48}$$

$$H_L\left(\mathbf{r}, \epsilon\right) \sim \frac{1}{r^{\ell+1}}, \; r \to 0.$$

For a vanishing potential $(V\left(r\right) \equiv 0)$ the radial wavefunctions are:

$$\begin{aligned}
R_\ell\left(r, \epsilon\right) &= j_\ell\left(\sqrt{\epsilon}r\right), \\
H_\ell\left(r, \epsilon\right) &= h_\ell\left(\sqrt{\epsilon}r\right),
\end{aligned} \tag{3.49}$$

where $h_\ell\left(\sqrt{\epsilon}r\right) = n_\ell\left(\sqrt{\epsilon}r\right) - \mathrm{i}j_\ell\left(\sqrt{\epsilon}r\right)$ is the spherical Hankel function, $j_\ell\left(\sqrt{\epsilon}r\right)$ is the spherical Bessel function and $n_\ell\left(\sqrt{\epsilon}r\right)$ is the spherical Neumann function. Solutions outside the sphere have to match the regular solutions inside the sphere. Therefore $R_\ell\left(r, \epsilon\right)$ for $r > r_0$ can be expressed as a linear combination of the spherical Bessel and Hankel functions, being the regular and irregular solutions of (3.46):

$$R_\ell\left(r, \epsilon\right) = j_\ell\left(\sqrt{\epsilon}r\right) + \sqrt{\epsilon}t\left(\epsilon\right) h_\ell\left(\sqrt{\epsilon}r\right). \tag{3.50}$$

It can be shown that the spherical Bessel function $j_\ell$ describes the propagation of the inciding plane wave, and the spherical Hankel function $h_\ell$ corresponds to the spherical wave backscattered at the perturbing potential $V\left(r\right)$ [65]. Physically this fact should be described by the Lippmann-Schwinger equation (3.28) [68, 69, 67, 62, 65, 66]:

$$R_\ell\left(r, \epsilon\right) = j_\ell\left(\sqrt{\epsilon}r\right) + \int_0^{r_{MT}} g\left(r, r', \epsilon\right) V\left(r'\right) R_\ell\left(r', \epsilon\right) r'^2 dr', \tag{3.51}$$

where $g\left(r, r', \epsilon\right)$ is the Green's function of the free space [69, 70]:

$$g\left(r, r', \epsilon\right) = \sqrt{\epsilon}j_\ell\left(\sqrt{\epsilon}r_<\right) h_\ell\left(\sqrt{\epsilon}r_>\right), \tag{3.52}$$

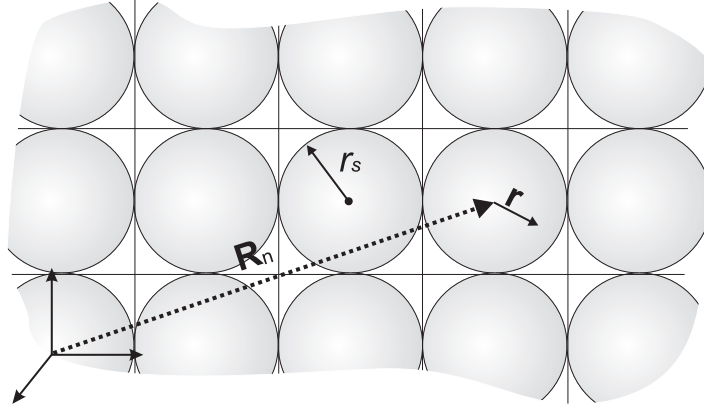$$r_< \equiv \min\left\{r, r'\right\}, \; r_> \equiv \max\left\{r, r'\right\}.$$

The equation (3.50) for the regular solution follows for $r > r_s$ from equations (3.51) and (3.52). The irregular solution outside the $r_s$ can be described only by the Hankel function:

$$H_\ell\left(r, \epsilon\right) = h_\ell\left(\sqrt{\epsilon}r\right), \; r > r_0. \tag{3.53}$$

The representation of T-operator can be obtained if the Lippmann-Schwinger equation (3.28) is compared with eq. (3.51) using (3.52), [68, 69, 67, 62, 66]:

$$t_\ell\left(\epsilon\right) = \int_0^{r_s} j_\ell\left(\sqrt{\epsilon}r'\right) V\left(r'\right) R_\ell\left(r', \epsilon\right) r'^2 dr' \tag{3.54}$$

**Figure 3.3:** A sketch of a crystal and cell-centered coordinates.

Finally the Green's function of a spherically symmetric potential in the free space can be constructed similar to (3.16) as the product of the regular and the irregular solutions (3.47) (3.48) and the corresponding spherical harmonics [68, 69, 67, 62, 65, 66, 71, 72]:

$$
\begin{aligned}
G_s\left(\mathbf{r}, \mathbf{r}', \epsilon\right) &= \sum_L G_\ell\left(r, r', \epsilon\right) Y_L\left(\hat{\hat{\mathbf{R}}}\right) Y_L\left(\hat{\mathbf{r}}'\right) \\
&= \sqrt{\epsilon} \sum_L R_\ell\left(r_<, \epsilon\right) H_\ell\left(r_>, \epsilon\right) Y_L\left(\hat{\hat{\mathbf{R}}}\right) Y_L\left(\hat{\hat{\mathbf{R}}}'\right).
\end{aligned}
\tag{3.55}
$$

The regular and irregular solutions must satisfy the Wronski relation:

$$
\left[H_\ell\left(r, \epsilon\right), R_\ell\left(r, \epsilon\right)\right] = \left(\partial_r H_\ell\left(r, \epsilon\right)\right) R_\ell\left(r, \epsilon\right) - \left(\partial_r R_\ell\left(r, \epsilon\right)\right) H_\ell\left(r, \epsilon\right) = \frac{1}{r^2 \sqrt{\epsilon}}.
\tag{3.56}
$$

### 3.2.8 Multiple scattering at single potentials: description of a bulk crystal

Any solid body can be represented as a collection of single potentials. Equation (3.39) demonstrates that the Green's function of a system with multiple scattering centers situated in the space domains $D_{V_i}$ can be represented as a sum of corresponding single-site scattering Green's functions $\hat{\mathcal{G}}^i$ and the term describing all multiple scattering processes through the structural Green's function $\hat{\underline{\mathcal{G}}}^{ij}$. This approach can be easily applied to a crystall if we assume that a crystall can be determined as a periodic array of spherically symmetric potentials with centers at the lattice sites $\mathbf{R}_i$. It can be demonstrated that in cell-centered coordinates [see Fig. 3.3]:

$$
\begin{aligned}
\mathbf{r} &\rightarrow \mathbf{r} + \mathbf{R}_n \\
\mathbf{r}' &\rightarrow \mathbf{r}' + \mathbf{R}_{n'}, \qquad r, r' < r_s,
\end{aligned}
\tag{3.57}
$$

the solution of the Kohn-Sham equation

$$
\left[-\frac{\partial^2}{\partial r^2} + + V_n\left(r\right) - \epsilon\right] G\left(\mathbf{r} + \mathbf{R}_n, \mathbf{r}' + \mathbf{R}_{n'}, \epsilon\right) = -\delta_{nn'}\delta\left(\mathbf{r} - \mathbf{r}'\right)
\tag{3.58}
$$

for the Green's function with the spherical potential $V_n(r)$ at the lattice site $\mathbf{R}_n$ can be formulated as [62, 65, 66, 71, 72]:

$$G\left(\mathbf{r}+\mathbf{R}_n, \mathbf{r}'+\mathbf{R}_{n'}, \epsilon\right) = \delta_{nn'}G_s^n\left(\mathbf{r}+\mathbf{R}_n, \mathbf{r}'+\mathbf{R}_n, \epsilon\right) +$$
$$+ \sum_{LL'} Y_L(\hat{\mathbf{r}}) R_\ell^n(r, \epsilon) \underline{G}_{LL'}^{nn'}(\epsilon) R_{\ell'}^{n'}(r', \epsilon) Y_{L'}(\hat{\mathbf{r}}'). \tag{3.59}$$

Up to now we have counted the perturbation of the system as a deviation from the propagation of electrons in free space. On the other hand the KKR approach is not restricted to the choice of the unperturbed Green's function $\hat{\mathcal{G}}_0$ and therefore any system can be taken as an unperturbed one [72, 73, 74]. For instance, a crystal with substitutional defects can be described as a perturbation of the ideal crystal [68, 69, 75, 76]. The Green's function $G(\mathbf{r}, \mathbf{r}', E)$ for the crystal with point defects and that of the ideal crystal $\overset{o}{G}(\mathbf{r}, \mathbf{r}', \epsilon)$ are related by the Dyson equation (3.22):

$$G\left(\mathbf{r}+\mathbf{R}_n, \mathbf{r}'+\mathbf{R}_{n'}, \epsilon\right) = \overset{o}{G}\left(\mathbf{r}+\mathbf{R}_n, \mathbf{r}'+\mathbf{R}_{n'}, \epsilon\right) +$$
$$+ \sum_{n''} \int \overset{o}{G}\left(\mathbf{r}+\mathbf{R}_n, \mathbf{r}''+\mathbf{R}_{n''}, \epsilon\right) \triangle V_{n''}(r'') G\left(\mathbf{r}''+\mathbf{R}_{n''}, \mathbf{r}'+\mathbf{R}_{n'}, \epsilon\right) \mathbf{dr}'', \tag{3.60}$$

where $\triangle V_n(r) \equiv V_n(r) - V(r)$ is the potential perturbation at the lattice site $\mathbf{R}_n$ caused by impurities. The integration in (3.60) is performed only over the region that is assumed to be perturbed. In metals, potential perturbation is effectively screened by the electron gas and perturbation is different from zero only in the vicinity of defects. The algebraic Dyson equation for the defect structural Green's function $\underline{G}_{LL'}^{nn'}(\epsilon)$ can be obtained from the equations (3.59) and (3.60):

$$\underline{G}_{LL'}^{nn'}(\epsilon) = \overset{o}{\underline{G}}_{LL'}^{nn'}(\epsilon) + \sum_{nn'LL'} \overset{o}{\underline{G}}_{LL''}^{nn''}(\epsilon) \triangle t_{\ell''}^n(\epsilon) \underline{G}_{L''L'}^{n''n'}(\epsilon), \tag{3.61}$$

where $\triangle t_{\ell''}^n(\epsilon) = t_{\ell''}^n(\epsilon) - \overset{on}{t}_{\ell''}(\epsilon)$ is the difference between the t-matrices of perturbed and host potentials.

We consider the infinite bulk as the perturbation of the free space [71, 72, 73]. The Dyson equation for the structural Green's functions of the crystal $\overset{o}{\underline{G}}_{LL''}^{nn'}(\epsilon)$ and free space $g_{LL'}^{nn'}$ is the following:

$$\overset{o}{\underline{G}}_{LL''}^{nn'}(\epsilon) = g_{LL'}^{nn'}(\epsilon) + \sum_{n''L''} g_{LL''}(\epsilon) \overset{o}{t}_{\ell''}(\epsilon) \overset{o}{\underline{G}}_{L''L'}^{n''n'}(\epsilon). \tag{3.62}$$

Due to translational invariance the host and perturbed structural Green's functions depend only on the difference $\mathbf{R}_n - \mathbf{R}_{n'}$ and the t-matrix is the same for each lattice site. That makes it possible to solve the Dyson equation using the following Fourier transform:

$$\overset{o}{\underline{G}}_{L''L'}(\mathbf{k}, \epsilon) = \sum_{n'} e^{-i\mathbf{k}(\mathbf{R}_n'' - \mathbf{R}_{n'})} \overset{o}{\underline{G}}_{L''L'}^{n''-n'}(\epsilon). \tag{3.63}$$

The Dyson equation (3.62) in this case is formulated in the momentum-space:

$$\overset{o}{\underline{G}}_{LL''}(\mathbf{k}, \epsilon) = g_{LL'}(\mathbf{k}, \epsilon) + \sum_{L''} g_{LL''}(\mathbf{k}, \epsilon) \overset{o}{t}_{\ell''}(\epsilon) \overset{o}{\underline{G}}_{L''L'}(\mathbf{k}, \epsilon). \tag{3.64}$$

$\overset{o}{G}_{LL''}(\mathbf{k}, \epsilon)$ is obtained from (3.64) by a simple matrix inversion and the structural coefficients $\overset{o\ nn'}{\underline{G}_{LL''}}$ are calculated by the inverse Fourier transform:

$$\overset{o\ nn'}{\underline{G}_{LL''}}(\epsilon) = \frac{1}{V_B} \int e^{-i\mathbf{k}(\mathbf{R}_n - \mathbf{R}_{n'})} \overset{o}{\underline{G}}_{LL'}(\mathbf{k}, \epsilon)\, \mathbf{dk}, \tag{3.65}$$

where $\overset{o}{\underline{G}}_{LL'}(\mathbf{k}, \epsilon)$ can be expressed through the $g_{LL''}(\mathbf{k}, \epsilon)$ with the help of the fundamental KKR equation (3.42):

$$\overset{o\ nn'}{\underline{G}_{LL''}}(\epsilon) = \frac{1}{V_B} \int e^{-i\mathbf{k}(\mathbf{R}_n - \mathbf{R}_{n'})} \sum_{L''} \left[ \left( \hat{\mathcal{I}} - \mathbf{g}(\mathbf{k}, \epsilon)\, \hat{\mathbf{t}}(\epsilon) \right) \right]^{-1}_{LL''} g_{LL''}(\mathbf{k}, \epsilon)\, \mathbf{dk}. \tag{3.66}$$

Integration is hold over the first Brillouin zone. The band structure according the equation (3.43) is defined by the eigenvalues of the KKR matrix in the square brackets.

### 3.2.9   Surfaces and layered systems

Exactly the same scheme can be applied to surfaces. In this case a surface is viewed as a planar perturbation of the infinite bulk [see Fig. 3.4] [71, 72, 73, 74]. Each layer of the planar perturbation can be identified by the index $i$ and equivalent atoms in the monolayer $i$ are enumerated by index $\nu$. The lattice vector $\mathbf{R}_n$ can be unambiguously expressed by the sum of the reference vector of the $i$-th layer and a lattice vector $\chi_\nu$ of the two-dimensional Bravais lattice of the monolayer $i$ [see Fig. 3.5].  The Dyson equation for the structural Green's functions in case of planar perturbation can be stated as [62, 66, 72, 73, 74]:

$$\underline{G}_{LL'}^{ii'\ \nu\nu'}(\epsilon) = \overset{o\ ii'\ \nu\nu'}{\underline{G}_{LL'}}(\epsilon) + \sum_{i'',\nu'',L''} \overset{o\ ii''\ \nu\nu''}{\underline{G}_{LL''}}(\epsilon)\, \triangle t_{\ell''}^{i''}(\epsilon)\, \overset{o\ i''i'\ \nu''\nu'}{\underline{G}_{L''L'}}(\epsilon), \tag{3.67}$$

where $\triangle t_\ell^n(\epsilon) \equiv t_\ell^n(\epsilon) - \overset{o\ n}{t}_\ell(\epsilon)$. Due to 2D translational symmetry both host and perturbed Green's functions depend only on the difference $\chi_\nu - \chi_{\nu'}$:
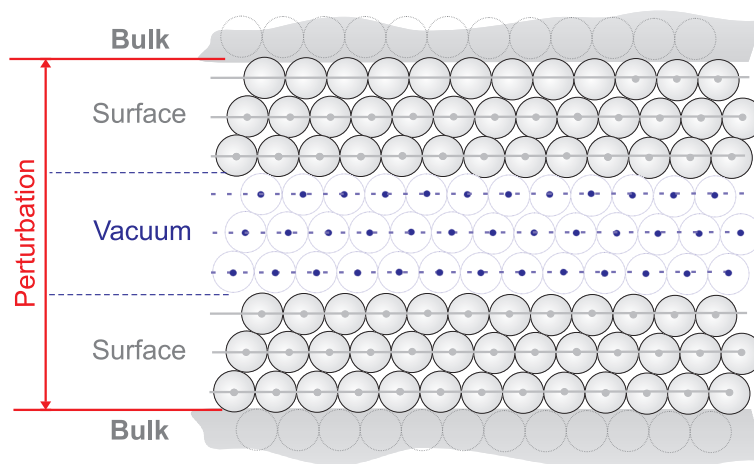
$$\underline{G}_{LL'}^{ii'\ \nu\nu'}(\epsilon) = \underline{G}_{LL'}^{ii'\ \nu-\nu'}(\epsilon)$$
$$\overset{o\ ii'\ \nu\nu'}{\underline{G}_{LL'}}(\epsilon) = \overset{o\ ii'\ \nu-\nu'}{\underline{G}_{LL'}}(\epsilon) \tag{3.68}$$

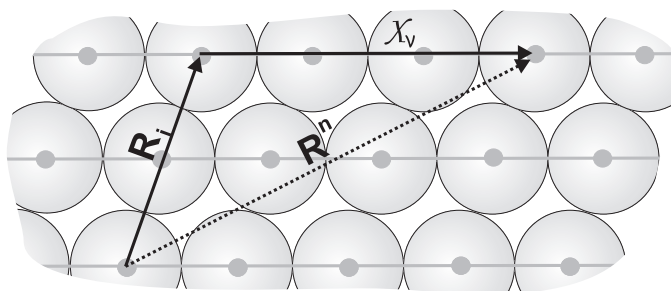Similarly to (3.62) the Dyson equation (3.68) can be solved with the help of the 2D Fourier transforms:

$$\underline{G}_{L''L'}^{ii'}(\mathbf{q}_\parallel, \epsilon) = \sum_{\nu'} e^{-i\mathbf{q}_\parallel(\chi_\nu - \chi_{\nu'})} \underline{G}_{L''L'}^{ii'\ \nu-\nu'}(\epsilon)$$
$$\overset{o\ ii'}{\underline{G}_{L''L'}}(\mathbf{q}_\parallel, \epsilon) = \sum_{\nu'} e^{-i\mathbf{q}_\parallel(\chi_\nu - \chi_{\nu'})} \overset{o\ ii'\ \nu-\nu'}{\underline{G}_{L''L'}}(\epsilon), \tag{3.69}$$

so the 2D Dyson equation (3.68) is formulated as:

$$\underline{G}_{LL'}^{ii'}(\mathbf{q}_\parallel, \epsilon) = \overset{o\ ii'}{\underline{G}_{LL'}}(\mathbf{q}_\parallel, \epsilon) + \sum_{i'',L''} \overset{o\ ii''}{\underline{G}_{LL''}}(\mathbf{q}_\parallel, \epsilon)\, \triangle t_{\ell''}^{i''}(\epsilon)\, \underline{G}_{L''L'}^{i''i'}(\mathbf{q}_\parallel, \epsilon). \tag{3.70}$$

**Figure 3.4:** In KKR calculations a surface can be represented as a planar perturbation of the infinite bulk.



**Figure 3.5:** Notation of the lattice vectors for the description of planar defects.

The structural Green's function $\underline{G}_{LL'}^{ii'\,\nu\nu'}(\epsilon)$ can be calculated by the integration of the $\underline{G}_{LL'}^{ii'}(\mathbf{q}_\parallel, \epsilon)$ over the 2D Brillouin zone:

$$\underline{G}_{LL'}^{ii'\,\nu-\nu'}(\epsilon) = \frac{1}{\Sigma_{BZ}} \int e^{i\mathbf{q}_\parallel(\chi_\nu - \chi_{\nu'})} \underline{G}_{LL'}^{ii'}(\mathbf{q}_\parallel, \epsilon)\, \mathbf{dq}_\parallel, \tag{3.71}$$

where $\Sigma_{BZ}$ is the area of 2D Brillouin zone. To solve the 2D Dyson equation (3.70) it is still necessary to calculate the host real-space 2D structural Green's function $\overset{o}{\underline{G}}_{LL'}^{ii'\,\nu-\nu'}(\epsilon)$. It can be derived from the structural Green's function $\overset{o}{\underline{G}}_{LL''}(\mathbf{k}, \epsilon)$ of an ideal bulk by means of a Fourier integral over the first Brillouin zone of the 3D-lattice:

$$\overset{o}{\underline{G}}_{LL'}^{ii'\,\nu-\nu'}(\epsilon) = \frac{1}{V} \int e^{i\mathbf{k}(\mathbf{R}_i + \chi_\nu - \mathbf{R}_{i'} - \chi_{\nu'})} \overset{o}{\underline{G}}_{LL''}(\mathbf{k}, \epsilon)\, \mathbf{dk}. \tag{3.72}$$

## 3.2.10  Screened KKR

A choice (3.62) of free space as a reference system for 3D bulk may seem to be the most convenient, because the free space structural Green's function matrix elements $\underline{g}_{LL'}^{nn'}$ are analytically known [73, 72, 71]. However, such an approach applied to periodic systems has a serious disadvantage. Fourier series (see (3.63))

$$\underline{g}_{LL'}(\mathbf{k}, \epsilon) = \sum_{n'} e^{-i\mathbf{k}(\mathbf{R}_n - \mathbf{R}_{n'})} \underline{g}_{LL'}^{n-n'}(\epsilon). \tag{3.73}$$

converge only conditionally and require demanding Ewald procedures for their evaluation [72]. This problem originates from the free-electron singularities for $E = |\mathbf{k} + \mathbf{G_a}|^2$, where $\mathbf{k}$ is the wave vector and $\mathbf{G_a}$ is a reciprocal lattice vector. Green's function singularity corresponds to the eigenstate of the potential-free space, so to avoid it one can start from the reference system, which has no eigenstates in the energy range of valence electrons and the reference Green's function would then decay exponentially [73, 72]. The matrix elements of the screened KKR (SKKR) structural Green's function should be calculated numerically according to the Dyson equation (3.62).

Any potential without eigenstates in the energy range of valence electrons can be used as a new reference system. The simplest choice is an infinite array of finite repulsive potentials $V_{\mathbf{R_n}}(\mathbf{r})$ constant inside nonoverlapping spheres circumstained around each scattering center $\mathbf{R_n}$ and a zero potential in the interstitial region between the spheres:

$$V_{\mathbf{R_n}}(\mathbf{r}) = \begin{cases} V_C, & |\mathbf{r}| \leq R_s^n \\ 0, & \text{otherwise} \end{cases} \tag{3.74}$$

The value $V_C$ of constant potential is usually chosen to be a few Rydbergs. It was demonstrated that eigenstates of such potentials fell above 0.7 Ry for potentials of 1 Ry height, above 1.35 Ry for 2 Ry high potentials, 2.24 Ry for 4 Ry high potentials

The scheme described above is the exact mathematical treatment of the problem. The resulting SKKR method does not rely upon the exponential decay of the density matrix and therefore is suitable for particular materials and systems. SKKR works for metals, semiconductors and insulators. We also use this method in the present work.

### 3.2.11   Clusters on surfaces

The consideration of clusters on the surface destroys the translation symmetry. Therefore the Green's function of a cluster on a surface is calculated in a real space formulation. The structural Green's function of the ideal surface in real space representation is then used as the reference Green's function for the calculation of the cluster-surface system from an algebraic Dyson equation:

$$\underline{G}_{LL'}^{nn'}(E) = \overset{o}{\underline{G}}_{LL'}^{nn'}(E) + \sum_{n''L''} \overset{o}{\underline{G}}_{LL''}^{nn''}(E)\Delta t_{L''}^{n''}(E)\underline{G}_{L''L'}^{n''n'}(E), \qquad (3.75)$$

where $\underline{G}_{LL'}^{nn'}(E)$ is the energy-dependent structural Green's function matrix and $\overset{o}{\underline{G}}_{LL''}^{nn''}(E)$ – the corresponding matrix for the ideal surface, serving as a reference system. $\Delta t_{L}^{n}(E)$ describes the difference in the scattering properties at site $n$ induced by the existence of the adsorbate atom.

For the first time self-consistent calculations of single Ni, Zn, Ga and Ge impurities in Cu crystal were performed in 1979 by Zeller and Dederichs [68]. In a year, realistic self-consistent electronic structures of 3d magnetic impurities embedded into bulk Cu and Ag were presented [69]. Obtained results were in a qualitative agreement with the Anderson model, but it was emphasized that modifications of the impurities' electronic structures due to host band structure were important. Local magnetic moments were in a reasonable agreement with available experimental data. Further improvements of the method made possible calculations of the exchange interaction of magnetic dimers in nonmagnetic hosts like Cu or Ag [77].

Development of the KKR for layered systems open up a possibility to study clusters on surfaces. Calculations performed for 4d transition-metal clusters on Ag(001) substrate, contrary to nonmagnetic bulks of the species investigated, revealed strong tendency to magnetism [74, 78]. Exact magnetic moments of 4d nanostructures were found to depend strongly on geometries of clusters. Later on similar calculations were conducted for 3d, 4d and 5d transition metals on Pd(001) and Pt(001) substrates [79].

## 3.3   Example KKR calculations: clean Cu(111) and adsorbed Fe atom

The KKR Green's function method is able to treat rather complex systems from the first principles. "From the first principles" means that a method can reproduce the properties of a *real system* having on the input the information on atomic species and, may be, on the system geometry. To illustrate how it works, we choose a Cu(111) surface, a system which properties have already been examined both theoretically and experimentally. In this section we demonstrate the Cu(111) surface state obtained by means of the KKR Green's function method, figure out surface state localization on Fe adatom and reveal spatial oscillations of LDOS around adsorbed Fe atom.

### 3.3.1   The surface state on Cu(111)

The KKR calculations start from the infinite Cu *fcc* crystal, which is assumed to be a 3D periodic perturbation of vacuum. The experimental lattice constant equal to 3.615 Å is used.

The Dyson equation (3.64) is solved for a set of $\mathbf{k}$ points from the irreducible part of 3D Brillouin Zone (BZ). In principle, various strategies for generation of $\mathbf{k}$-set can be applied. We use the Monkhorst-Pack method [80], which allows to generate sets of special points in the Brillouin zone which provides an efficient means of integrating periodic functions of the wave vector. Usually about 1000–10000 $\mathbf{k}$-points in the irreducible part of 3D BZ are used. The solution of the Dyson equation yields the Green's function of the Cu crystal, and, therefore, its electronic density. The ground state electronic density can be found by a self-consistent cycle, when the electronic density is used to calculate a perturbing potential. The perturbing potential, in turn, gives, through the solution of the Dyson equation, a new electronic density. If densities calculated at several consequent steps of the self-consistent cycle are the same within the predefined errorbar, one can use the obtained electronic density as a ground state one. The Fermi level is defined in a usual way as the energy at which the integrated density of states is equal to the number of valence electrons in a unit cell.

According to the approach explained in Section 3.2.9, a surface is treated as a 2D perturbation of infinite bulk. Geometry used in calculations is illustrated in Fig. 3.4. We use a perturbing slab consisting of 4 Cu layers 6 vacuum layers and again 4 layers of Cu. Cu layers at each side are introduced to account for surface related charge redistribution. Bulk electronic states are introduced in the system through the scattering matrix $\triangle t\,(\epsilon)$ imported from the bulk calculations. The Dyson equation (3.70) is now formulated in 2D $\mathbf{k}_\parallel$ space. The Green's function $\underline{G}_{LL'}^{ii'}\left(\mathbf{k}_\parallel, \epsilon\right)$ depends on energy $\epsilon$ and 2D momentum $\mathbf{k}_\parallel$, so its imaginary part $-1/\pi \mathfrak{Im} \underline{G}_{LL'}^{ii'}\left(\mathbf{k}_\parallel, \epsilon\right)$ is the momentum and energy resolved density of states, or the spectral density. Spectral density plotted for a plane or volume in $(\mathbf{k}_\parallel, \epsilon)$ space give an insight into the band structure of the studied system. A momentum resolved spectral density map (SDM) calculated at the Fermi energy for the interface Cu layer of the Cu(111) surface is demonstrated in Fig. 3.6(a). The green hexagon depicts the 2D BZ of the {111} $fcc$ surface. $\overline{\Gamma}$, $\overline{M}$ and $\overline{K}$ are high symmetry points. The black areas of the SDM correspond to projected bulk band gaps. One gap is situated at the $\overline{\Gamma}$-point, and six gaps are around $\overline{K}$-points. The blue and violet area correspond to projected bulk states of Cu. Yellow circle centered at $\overline{\Gamma}$-point represents a single isotropic band which can be attributed to the surface state. To prove it we demonstrate in Fig. 3.6(b) the SDM calculated along $\overline{M} - \overline{\Gamma} - \overline{K}$ line of the 2D BZ for energies from $-1.0$ to $0.2$ eV. The surface state band with parabolic dispersion is clearly visible. Fit to the parabolic dispersion law (1.27) (depicted with solid black curve in Fig. 3.6(b) gives the following parameters: band bottom $E_0 = -0.536$ eV, $m_{eff} = 0.38$, $k_F = 0.235$ Å$^{-1}$. These values are in a good agreement with parameters obtained by means of ARPES [see Table 1.1] and STS.

The surface state is bound to the surface, i.e. its density decays exponentially both into the vacuum and into the crystal. To be sure that the state we obtain in the KKR calculations is also bound to the surface region, in Fig. 3.7 we plot the spectral density at the $\overline{\Gamma}$-point at the surface state band bottom energy for different layers of our system. It is evident that the density is maximal at the surface and rapidly decays in both sides. Finally, it is reasonable to examine the vacuum LDOS at the surface state energies. LDOS calculated in the first vacuum layer is demonstrated in Fig. 3.8. The surface state step-like onset of LDOS appears at the band bottom energy. It is important to note that the surface state is formed mostly by $s$ and $p$ electrons.
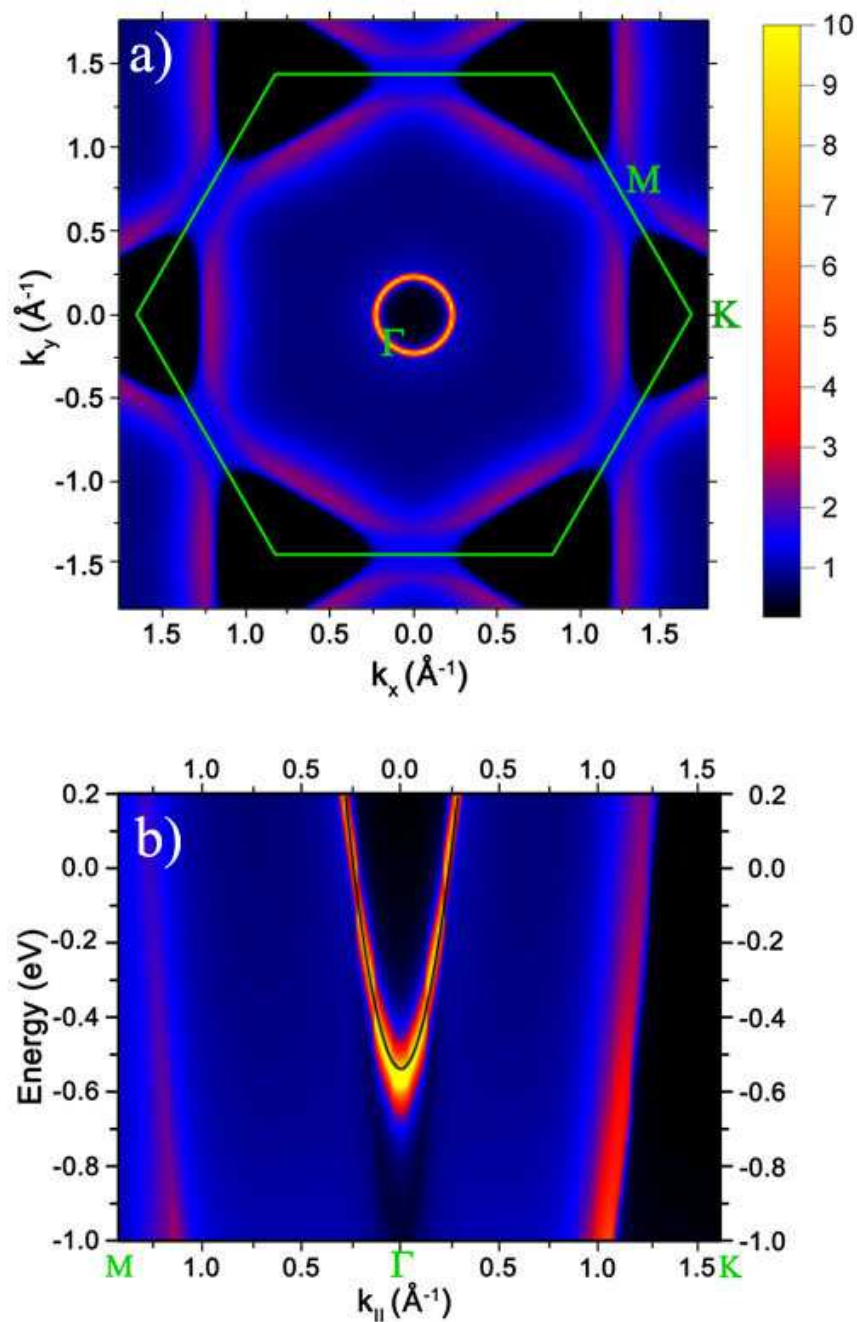
**Figure 3.6:** a) The momentum resolved SDM calculated at Fermi energy for the interface Cu layer. Blue and violet areas correspond to the projected bulk bands. Black regions are gaps of the projected band structure. A bright circle around $\overline{\Gamma}$-point is the surface state. b) The energy resolved SDM calculated along $M - \Gamma - K$ direction of the 2D BZ. The surface state band is presented as a bright parabola with a band bottom at $-0.536$ eV. Parabolic fit is plotted with a black line.
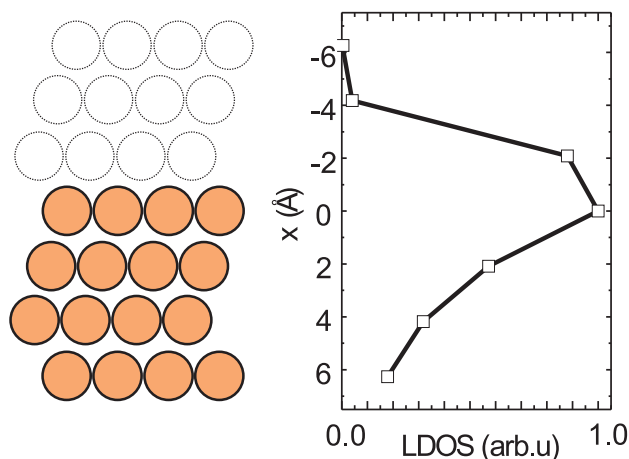
**Figure 3.7:** The spectral density at the $\overline{\Gamma}$-point at the surface state band bottom energy calculated for different layers.
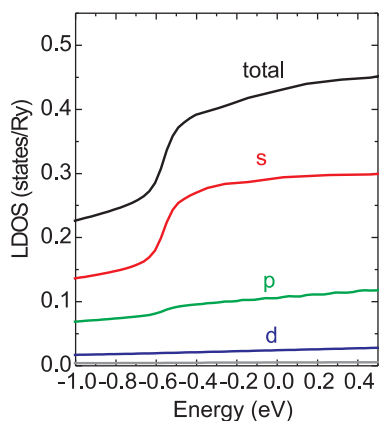


**Figure 3.8:** Density of states calculated in the first vacuum layer The surface state step-like onset is visible.
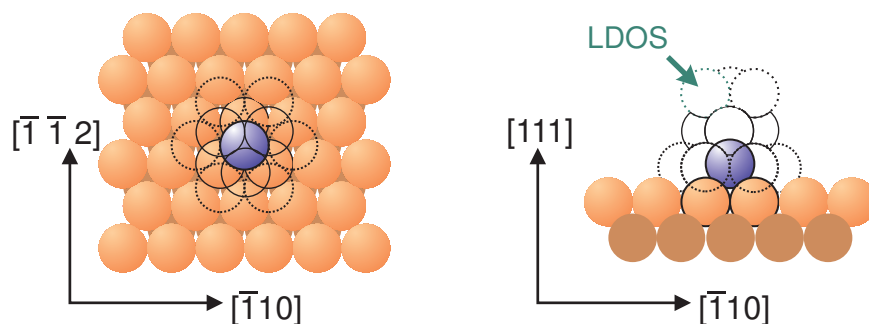


**Figure 3.9:** The atomic cluster used in the calculation of a single Fe adatom on Cu(111) surface. Left panel demonstrates the top view on Cu(111) surface, cluster atomic spheres are marked with black borders. A side view on the same cluster is shown on right panel. Green arrow points to the atomic sphere where the LDOS presented in Fig. 3.10 was calculated.

### 3.3.2   Iron adatom on Cu(111) surface

An adatom on a surface breaks the translational symmetry of the surface, so the Dyson equation is formulated in the real space. Perturbed region is built from the atomic spheres surrounding the adatom. Since potential perturbation in metals is effectively screened by the conduction electrons and perturbation is different from zero only in the vicinity of defects, it is enough to include in the perturbed cluster only surface and vacuum atomic spheres closest to the adatom. Such a cluster is sketched in Fig. 3.9. In Section 2.4, we demonstrate that an atom adsorbed onto the surface should provoke the appearance of a bound state. In the STS experiments such a state was revealed as an asymmetric resonance arising below the surface state band bottom [Fig. 2.10]. STS, according to the Tersoff-Haman theory [see Section 2.1], is proportional to the vacuum LDOS at the tip position. This allows a direct comparison of the calculated LDOS with the STS results. The spin-polarized LDOS calculated at 4.02 Å  above the Fe adatom is demonstrated in Fig. 3.10.

The surface state band bottom is marked with a vertical dashed line. Asymmetric resonances attributed as split-off bound states similar to those observed experimentally [Fig. 2.10] appear right below the band bottom in both spin channels. The same resonances for Fe adatom have been recently obtained by Stepanyuk et al. [45], Lounis et al. [47] and Lazarovits et al. [46].

The first LT STM/STS experiments revealed a spacial oscillations of the LDOS around adsorbed atoms [17]. The KKR Green's function method treats this phenomenon. The spin-polarized LDOS around Fe adatom is plotted in Fig. 3.11 as a function of distance from the impurity. Oscillations of the surface state density around adatom are evident both for minority and majority electrons, but, due to different scattering phase shifts, the minority and the majority densities are shifted with respect to each other. Nevertheless, the half periods of minority and majority oscillations are the same and equal to $\sim 14$ Å.

## 3.4   Atomic scale simulations

### 3.4.1   General Strategy

Fully ab initio structural relaxation of a system consisting of hundreds atoms become a challenging problem and very often demands too advanced computing facilities to be performed in appropriate time. It is much more convenient to use some simplified model to obtain relaxed atomic positions. Interatomic forces in such an approach are defined explicitly but depend on a number of parameters which are to be somehow fitted in order to reproduce a real system. Once forces acting on each atom are defined, it is possible to determine the equilibrium structure at some temperature by integrating the newtonian motion equations

$$\frac{d^2 \mathbf{r}_i}{dt^2} = \frac{\mathbf{F}_i}{m_i} \tag{3.76}$$

where $\mathbf{r}$ is the coordinate, $m_i$ is the mass and $\mathbf{F}_i$ is the force acting on the $i$-th atom. If $N$ is the total number of atoms in the system, then a system of $N$ motion equations (3.76) define coordinates and velocities of all the atoms. Numerical solution of the system (3.76) is performed by means of the Euler's method. The differential equations are replaced with
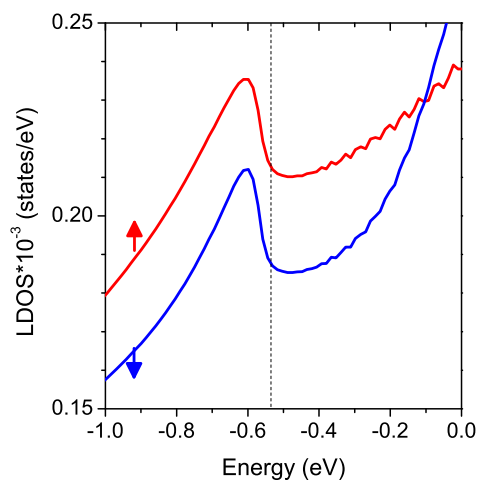
**Figure 3.10:** The spin-polarized LDOS calculated at 4.02 Å above Fe adatom on Cu(111) surface. The bound state split off the surface state band bottom (see Section 2.4 for details) is clearly visible in both spin-channels.
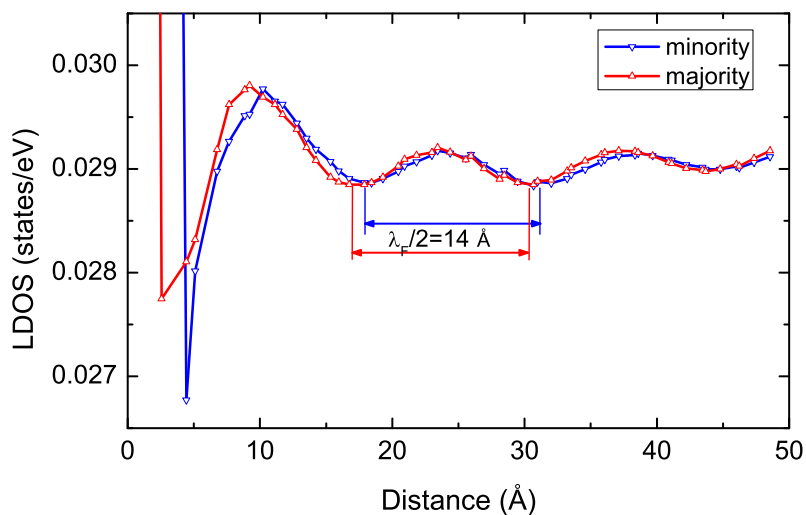


**Figure 3.11:** The spin-polarized standing wave pattern around a single Fe adatom on Cu(111) surface calculated at Fermi level. Oscillations of the surface state density around adatom are evident both for minority (blue, down triangles) and majority (red, up triangles) electrons, but, due to different scattering phase shifts, the minority and the majority densities are shifted with respect to each other. Nevertheless, the half periods of minority and majority oscillations are the same and equal to $\sim 14$ Å.

finite differences:

$$
\begin{cases}
\mathbf{v}_i^{n+1/2} - \mathbf{v}_i^{n-1/2} = \dfrac{\mathbf{F}_i^n}{m_i}\Delta t \\
\mathbf{r}_i^{n+1} - \mathbf{r}_i^n = \mathbf{v}_i^{n+1/2}\Delta t.
\end{cases}
\tag{3.77}
$$

The first equation describes the momentum conservation law written for $i^{th}$ atom at $n^{th}$ time step. The change of velocity $\Delta\mathbf{v} = \mathbf{v}_i^{n+1/2} - \mathbf{v}_i^{n-1/2}$ is determined by the force $\mathbf{F}_i^n$ acting on the atom $i$ with mass $m_i$ during the unit time interval $\Delta t$. The second equation is the definition of the velocity formulated in finite differences.

Such a scheme can be applied to two major tasks: the first is the study of the time evolution of the system at some nonzero temperature $T$ and the second is investigation of the relaxed geometries, where forces acting on all the atoms in the system are zero. The latter case corresponds to the system at zero temperature when all the atoms are immobile. Cooling to zero temperature is applied through the quenching procedure when the velocity $\mathbf{v}_i^{n+1/2}$ is canceled if scalar product $\left(\mathbf{r}_i^{n+1} - \mathbf{r}_i^n, \mathbf{F}_i\right)$ becomes negative. The scheme described above can be, in principle, applied to any kind of system including ideal gases, van der Vaals gases, liquids, solids. The behavior of each system is determined by the interaction $E$. Forces acting on each atom of the system are then calculated as $\mathbf{F} = -\nabla E$. The particular form of $E$ is derived from the physical properties of the system being investigated.

### 3.4.2  Interatomic potentials

The form of many-body interatomic potential $E$ can be derived from simple assumptions on the electronic structure of the materials studied. The LDOS of transition metals, we are interested in, is characterized by the narrow partly filled $d$ band and by broad band of quasi-free $s$-$p$ electrons. It is well known that the cohesive properties of transition metals originate from the $d$-band density of states. The attractive bond energy describing many-atom interactions due to bonding is obtained as a measure of $d$ electrons energy with respect to the band center of gravity $E_d$

$$
E_B = \int^{E_F} (E - E_d)\, n_d(E)\, dE,
\tag{3.78}
$$

where $n_d(E)$ is $d$ band density of states. The realistic density of states associated with atom $i$ can be replaced by a hypothetic gaussian centered at $E_d$ with the dispersion (or second moment) $\mu_{(i)}$ [81, 82]:

$$
n_{(i)}(E) = \frac{10}{\mu_{(i)}\sqrt{2\pi}} \exp\left(-\frac{(E - E_d)^2}{2\mu_{(i)}^2}\right).
\tag{3.79}
$$

Factor 10 appears from the normalization of the $n_{(i)}(E)$ to the total number of $d$ electrons. Substituting (3.79) to (3.78) one can easily obtain the expression for the bond energy

$$
E_B^{(i)} = -\frac{5\mu_{(i)}}{\sqrt{2\pi}} \exp\left(-\frac{(E_F - E_d)^2}{2\mu_{(i)}^2}\right).
\tag{3.80}
$$

Finally, $\mu_{(i)}$ can be derived from the definition of the second moment of the density of states of $i$-th atom [83, 82]:

$$
\mu_{(i)}^2 = \int_{-\infty}^{\infty} (E - E_d)^2\, n_{(i)}(E - E_d)\, dE.
\tag{3.81}
$$

Integral (3.81) describes the hopping of the electrons from the atom $i$ to all the neighbor atoms $j$ and therefore it can be rewritten by means of the effective hopping integral $\xi_{ij}$ depending on the chemical species $\alpha(i)$ and $\beta(j)$ of atoms at sites $i$ and $j$:

$$\mu_{(i)}^2 = \sum_j \xi_{\alpha(i)\beta(j)}^2. \tag{3.82}$$

Taking into account a dependence of the hopping integral on the distance between interacting atoms [84], the following general expression for the bond energy can be derived from (3.80) and (3.82):

$$E_{(i)}^B = -\sqrt{\sum_{j \neq i,\, r_{ij} < r_c} \xi_{\alpha(i)\beta(j)}^2 \exp\left[-2q_{\alpha(i)\beta(j)}\left(\frac{r_{ij}}{r_{0_{\alpha(i)\beta(j)}}} - 1\right)\right]}, \tag{3.83}$$

where $q_{ij}$ characterizes the distance dependence of the hopping integral between atoms at sites $i$ and $j$; $r_{ij}$ is the distance between sites and $r_0$ is the first neighbor distance for the given chemical species. Note, that starting from some interatomic separation $r_{ij} = r_c$ the bond energy $E_{(i)}^B(r_{ij})$ is close to zero, so it is reasonable to assumed that the interaction is canceled beyond this cutoff radius $r_c$.

The repulsive part $E_R^{(i)}$ is introduced to stabilize the system as a sum of modified Born-Mayer ion-ion repulsions:

$$E_{(i)}^R = \sum_{j \neq i\, r_{ij} < r_c} \left[A_{\alpha(i)\beta(j)}^1 \left(\frac{r_{ij}}{r_{0_{\alpha(i)\beta(j)}}} - 1\right) A_{\alpha(i)\beta(j)}^0\right] \exp\left[-p_{\alpha(i)\beta(j)}\left(\frac{|\mathbf{r}_{ij}|}{r_{0_{\alpha(i)\beta(j)}}} - 1\right)\right] \tag{3.84}$$

where $p_{\alpha(i)\beta(j)}$ is related to the bulk modulus of the material. The term $A_1$ introduced into the repulsive term makes the potential more flexible in applications for surfaces and nanoclusters. The relevance of this correction was proved by a number of works [85, 86, 87, 88, 89, 90, 91].

The energy $E_{(i)}$ of atom $i$ is stated as the sum of an attractive band energy $E_{(i)}^B$ (3.83) and a repulsive pair interaction $E_{(i)}^R$ (3.84):

$$E_i = E_{(i)}^B + E_{(i)}^R \tag{3.85}$$

It was shown in many calculations that many-body interatomic potentials correctly describe surface relaxations, reconstruction, and diffusion on surfaces of fcc transition metals [85, 86, 87, 88, 89, 90, 91].

### 3.4.3 Details of realization

To construct potentials for different systems the interaction parameters

$$\varrho_{\alpha\beta} = \{A^1, A^0, \xi, p, q, r_0\} \tag{3.86}$$

are to be fitted to reproduce a set $\{\mathbb{P}^0\}_i$ of experimental and theoretical values of the lattice constant, cohesive energy, bulk modulus, binding energy of embedded and ad-clusters of different sizes and geometry. Surface-related properties are taken into account for realistic description of the atomic relaxations in supported clusters. For the same sake ab initio values

of Helmann-Feynman forces acting on the adatom on the surface can be used. Potential parameters (3.86) are fitted to minimize the functional

$$\mathcal{F}[\varrho_{\alpha\beta}] = \sum_i (\mathcal{P}_i(\varrho_{\alpha\beta}) - \mathbb{P}_i^0)^2, \qquad (3.87)$$

Minimization is performed numerically by means of conjugate gradient method. Table 3.4.3 lists parameters of the Co-Cu potentials. These potentials have been recently used in a number of works [86, 85, 88, 90, 92, 87].

**Table 3.1:** Parameters of interatomic potentials for Cu/Cu systems.

| Parameter | $A^1$ (eV) | $A^0$ (eV) | $\xi$ (Å) | $p$ | $q$ | $r_0$ (Å) |
|---|---|---|---|---|---|---|
| Cu-Cu | 0.0000 | 0.0854 | 1.2243 | 10.939 | 2.2799 | 2.5563 |
| Co-Cu | -1.5520 | -0.0372 | 0.8522 | 7.6226 | 5.5177 | 2.4995 |
| Co-Co | 0.0000 | 0.1209 | 1.5789 | 11.3914 | 2.3496 | 2.4953 |

### 3.4.4   Example of MD relaxation: short Co chains on Cu(554) surface

To illustrate the MD method we present here our recent results on the relaxation of short Co chains placed at the step ledge of Cu(111) vicinal surface [90]. We calculated relaxations of short $Co_2$-$Co_7$ chains at the step edge of Cu(554) vicinal surface. The coordinate frame used is drawn in the insert of Fig. 3.12. The $x$-axis is parallel to the step, the $z$-axis direction matches the surface terrace-normal and the $y$ axis points from the step. Projections of relaxed atomic positions of the Co chains and underlying substrate atoms on $xz$ plane are plotted respectively in upper and lower panels of Fig. 3.12(a-f). Vertical displacements of Co atoms strongly depend on the chain length. To rationalize such a difference and to find common features in Co chains relaxations, we should stress that the edge atoms of Co chains due to a lower coordination number, exhibit the strongest relaxations towards the substrate, towards the step and towards the adjacent Co atom. The positions of Cu atoms in the step remain practically the same except Cu atoms at the chain edges (they are marked with green arrows in the insert of Fig. 3.12). These atoms move out from the step to the terrace. The picture described above remains valid for all the considered Co chains (see upper panels of Fig. 3.12(a-f)). Such a displacement of the edge Co atoms hinders the relaxation of the second atom in the chain towards the substrate. As a result, the second Co atoms are situated remarkably higher than the edge ones. This 'edge effect' completely explains the arched relaxations profiles of $Co_3$ and $Co_4$ chains. The longer $Co_5$, $Co_6$ and $Co_7$ chains have the 'letter M-like' shape when three outermost Co atoms form two arches at each edge of the chain and the rest Co atoms in the center exhibit similar relaxations forming steady central region. The description of the atomic relaxations in the Co chains can be summarized in the 3D illustration as is plotted in Fig. 3.13 for the $Co_7$ chain. All the considered Co chains push underlying substrate atoms downwards, but the outer substrate atoms exhibit upward vertical relaxations due to the shift of the edge Co atoms towards the chain center. The relative changes of Co-Co and Co-Cu bonds in $Co_7$
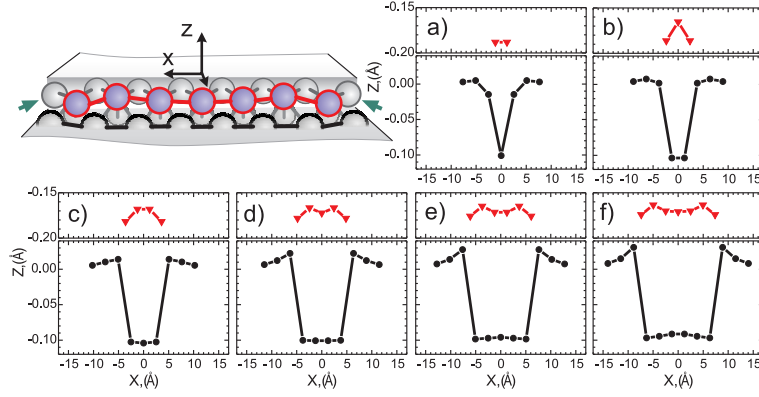
**Figure 3.12:** Strain relaxations in short Co chains placed at the Cu(111) vicinal surface step edge. The upper panels of all the figures demonstrate displacements of Co atoms in (a) $Co_2$, (b) $Co_3$, (c) $Co_4$, (d) $Co_5$, (e) $Co_6$, (f) $Co_7$ chains. The corresponding relaxation profiles of underlying substrate atoms are shown in lower panes. Coordinate origins coinside with the geometrical centers of corresponding unrelaxed structures. The figure is published in [90].

**Table 3.2:** Effect of atomic relaxations on structural and magnetic properties of the $Co_7$ chain. Values of Co-Co and Co-Cu bonds length changes are listed in percentage relative to the the unrelaxed bond length. Order of the Co atoms and bonds notation are illustrated in Fig. 3.14. Magnetic moments are calculated by means of tight-binding method. The table is published in [90].

| Bonds | Co atom | | | |
|---|---|---|---|---|
| | 1 | 2 | 3 | 4 |
| 1 | - | -6.2 | -3.2 | -2.3 |
| 2 | -6.2 | -3.2 | -2.3 | -2.3 |
| 3 | 0.3 | 0.6 | -0.8 | -1.5 |
| 4 | -5.2 | -2.6 | -2.0 | -1.5 |
| 5 | -0.8 | -0.4 | -1.9 | -2.6 |
| 6 | -6.1 | -3.8 | -3.2 | -2.6 |
| 7 | -3.5 | -3.3 | -3.3 | -3.3 |
| Magnetic moments $\mu_B$ | | | | |
| ideal | 1.71 | 1.68 | 1.64 | 1.66 |
| relaxed | 1.59 | 1.52 | 1.53 | 1.50 |

chain caused by relaxation are listed in Table 3.2. The Co atoms enumeration is explained in Fig. 3.14. Because of the reflection symmetry $x \rightarrow -x$ only first four Co atoms are considered in Table 3.2. The zoomed view in Fig. 3.14 elucidates the bonds notation. To illustrate the effect of relaxations on the electronic structure of $Co_7$ chain we also put in Table 3.2 values of spin magnetic moments for ideal and relaxed configurations calculated by means of tight-binding method [90]. In both cases edge Co atoms have the maximum magnetic moment in the chain. Atomic relaxations reduce magnetic moments of all the atoms.
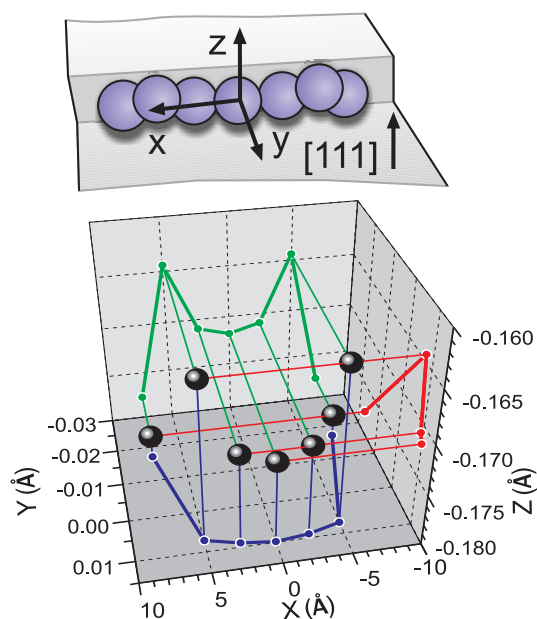
**Figure 3.13:** Three dimensional relaxation profile in the $Co_7$ chain. Edge atoms are strongly attracted to the step due to the lower coordination number. The next atoms from the edge are shifted from the step. Atoms in the middle of the chain lie approximately at the straight line. The figure is published in [90].
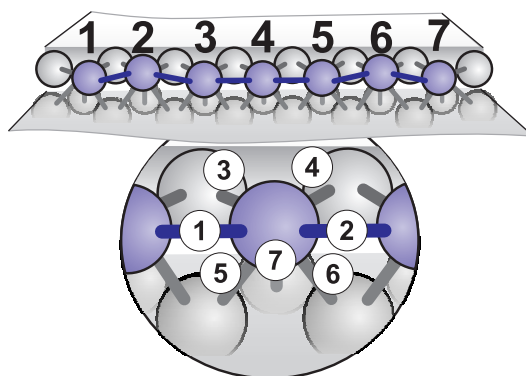


**Figure 3.14:** Sketch of the Cu(111) vicinal surface step with the $Co_7$ chain. Substrate Cu atoms are drawn with grey colour, Co chain is light blue. Top view illustrated Co atoms enumeration order used in table 3.2. Bottom zoomed view is designed to clarify the bonds notation from table 3.2. The figure is published in [90].

# Chapter 4

# Electronic states on stepped Cu(111) surfaces

Stepped or vicinals surfaces attract much attention of scientific community for more than 3 decades. Such regular or quasi-regular structures can be obtained if a crystal is cut along some plane vicinal to a high-symmetry plane of the crystal [93]. The interest to vicinal surfaces is not idle because such 1D-arranged structures are widely used as natural templates for self-assembly of 1D and quasi-1D nanostructures: adsorbed atoms diffuse across terraces and are trapped at steps [94, 95, 96, 97]. Below we describe a modern view on the surface state on stepped surfaces and report on our *ab initio* investigations of surface states on clean Cu(111) vicinals. Then we proceed to the study of Cu(111) vicinals decorated with Fe wires and demonstrate that localization of minority electrons at Fe wires results in the formation of spin-polarized surface states. At the end of the chapter we explain how a novel type of 1D magnetic Fe nanostructures can be grown on Cu(111) vicinal surface exploiting surface state confinement.

## 4.1 Stepped surface as a planar perturbation: the SKKR treatment

According to the KKR workflow any surface is to be treated as a planar perturbation of an infinite bulk. It is rather simple to imagine the structure of such a perturbation for high-symmetry planes of *fcc* crystal [see Fig. 3.4]. Any vicinal surfaces can be also treated in the same manner [98]. As an example we demonstrate how a set of inequivalent atoms is defined for Cu(332) surface. Every terrace of Cu(332) surface consists of atomic rows aligned in Fig. 4.1 along $z$-axis. It is natural to assume that all the atoms in the atomic row are equivalent. This yields us the first basis vector, pointing to the next atom in the same row (vector number 1 in Fig. 4.2). All the terraces of a vicinal surface are equivalent, or in another words, atoms of the row on one terrace are equivalent to all the atoms of the same row on all other terraces. Thus the second basis vector points to the same row on the adjacent terrace (vector number 2 in the Fig. 4.2). These two basis vectors define the equivalent atoms in the {332} plane. The third vector should point to the next atomic row in the terrace (vector number 3 in the Fig. 4.2). Atoms belonging to different atomic rows are inequivalent. Position of any atom in the system can be determined by means of these three vectors.
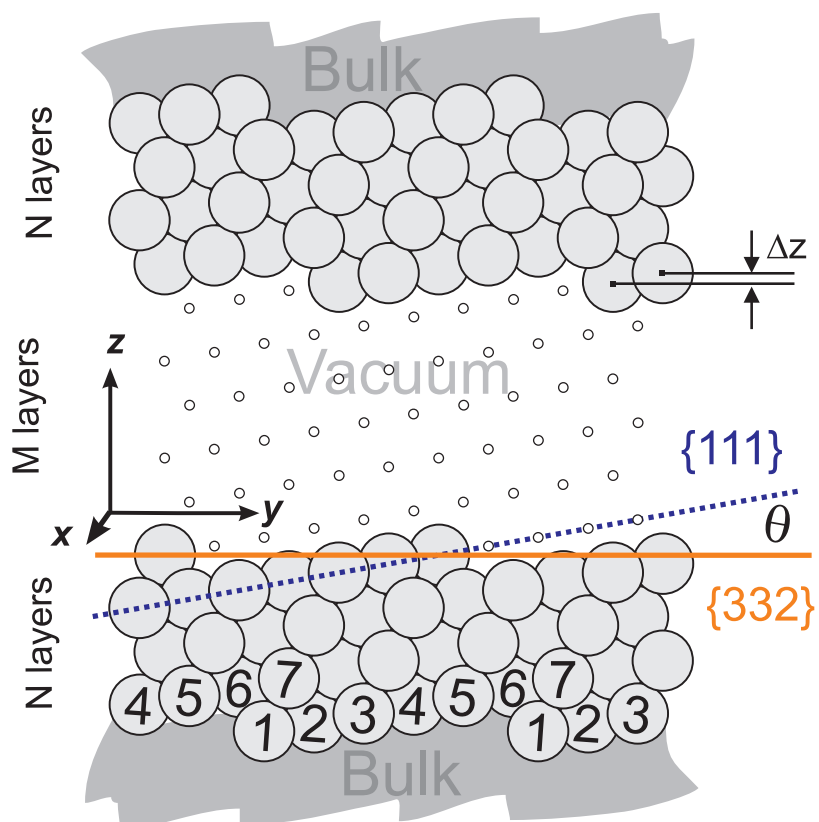
**Figure 4.1:** Vicinal Cu(332) surface as a planar perturbation of bulk. {332} plane is depicted by the red solid line. {111} terrace plane is sketched by dashed blue line. The angle Θ between these two plains is called a miscut angle. Atoms in the same row are equivalent. Inequivalent atoms in different rows are highlighted by numbering. The basis set for such a geometry is drawn in Fig. 4.2 .
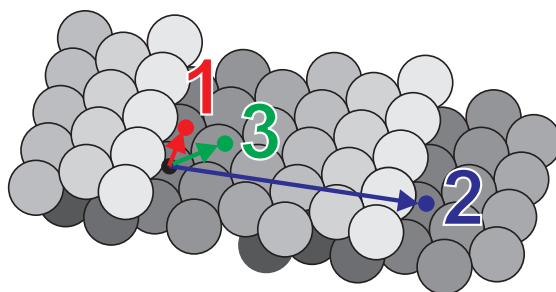


**Figure 4.2:** Bravais vectors of vicinal surface. The first vector points to the equivalent atom in the same atomic row. The second vector points to the equivalent atoms on the adjacent terrace. The third vector introduces the adjacent inequivalent atomic row.

The Dyson equation in the $k_\parallel$ space is written for the layers parallel to the {332} plane, sketched in Fig. 4.1 with the red line. This plane forms the miscut angle $\theta$ with the {111} plane of the step terraces. Inequivalent atoms in Fig. 4.1 are enumerated according to their $z$-coordinate, so each {111} terrace plane consists of atoms belonging to the layers with the ascending numbers. In this way, the first $N$ layers are Cu layers, the next $M$ layers are vacuum, and the last $N$ layers are Cu again. Because the interlayer distance $\Delta z$ is small, large $N$ and $M$ should be utilized to obtain a valid electronic states in the whole system. Exact values of $N$ and $M$ depend on $\Delta z$ and vary from 10 to 100 for different surfaces.

Any vicinal surface can be defined and studied by ab initio methods according to the described scheme. But it should be kept in mind that the total number of layers to be taken into account increases proportionally to the $[\sin(\theta)]^{-1}$. The wider terraces of vicinal surface are, the smaller miscut angle $\theta$ is and it increases requirements to the essential computer facilities and calculation time.

## 4.2    Results on clean Cu(111) vicinal surfaces

In our study we considered the following Cu(111) vicinals: Cu(332), Cu(775), Cu(443), Cu(997), Cu(554) with the terrace width equal to 12, 14, 16, 18, 20 Å, respectively. We have performed a systematic study of the surface states on these surfaces. We illustrate how the LDOS is changed across a terrace and discuss features of the electronic structure typical for vicinal surfaces. All data are also analyzed within the framework of 1D KP model.

### 4.2.1    LDOS on vicinal surfaces

At first we present our results on the LDOS calculated at centers of terraces of all the studied stepped surfaces as it is sketched in Fig. 4.3(a). LDOSes calculated above the terrace center of the considered vicinal surfaces are plotted in Fig. 4.3(b). They can be directly compared with LDOS calculated on flat Cu(111) surface, which is marked in Fig. 4.3(b) by the shaded area.

A brief analysis of Fig. 4.3(b) reveals that surface states of Cu(111) vicinal surfaces are shifted towards higher energies in comparison to the flat Cu(111). The similar effect has been observed in the STS experiments by Sánchez et al. [99] and Hansmann et al. [100]. The second remarkable feature of the LDOSes calculated on vicinal surfaces is a broad but evident peak. In Fig. 4.3(b) these peaks are marked by arrows. Such peaks are not observed in the LDOS of flat Cu(111). Position of the peak strongly depends on a terrace width. For instance, the peak is unoccupied on Cu(332) (L=11.9 Å), but it shifts under the Fermi level on Cu(775) (L= 14.1 Å). The peak position versus the terrace width is plotted in Fig. 4.3(c).

Our results are in a good agreement with the STS measurements of Hansmann et al. [100]. They studied the electronic structure of Cu(111) vicinals by means of STS/STM at low temperature [100]. This technique allows to locally acquire electronic structure data on individual terraces and sites rather than averaging over the entire sample as in photoemission. Figure 4.4(a) presents an atomistic structure of Cu(554) surface. Each terrace consisting of 9 atoms is 21 Å wide and has {111} facet. In the STM image [Fig. 4.4(b)], the Cu(554) surface consists of a fairly regular array of {111} terraces where the average terrace width is in a good agreement with the ideal value of 21 Å . However, deviations are observed and terrace widths are distributed around the expected value. Moreover, kink sites are present, affecting the step superlattice geometry.
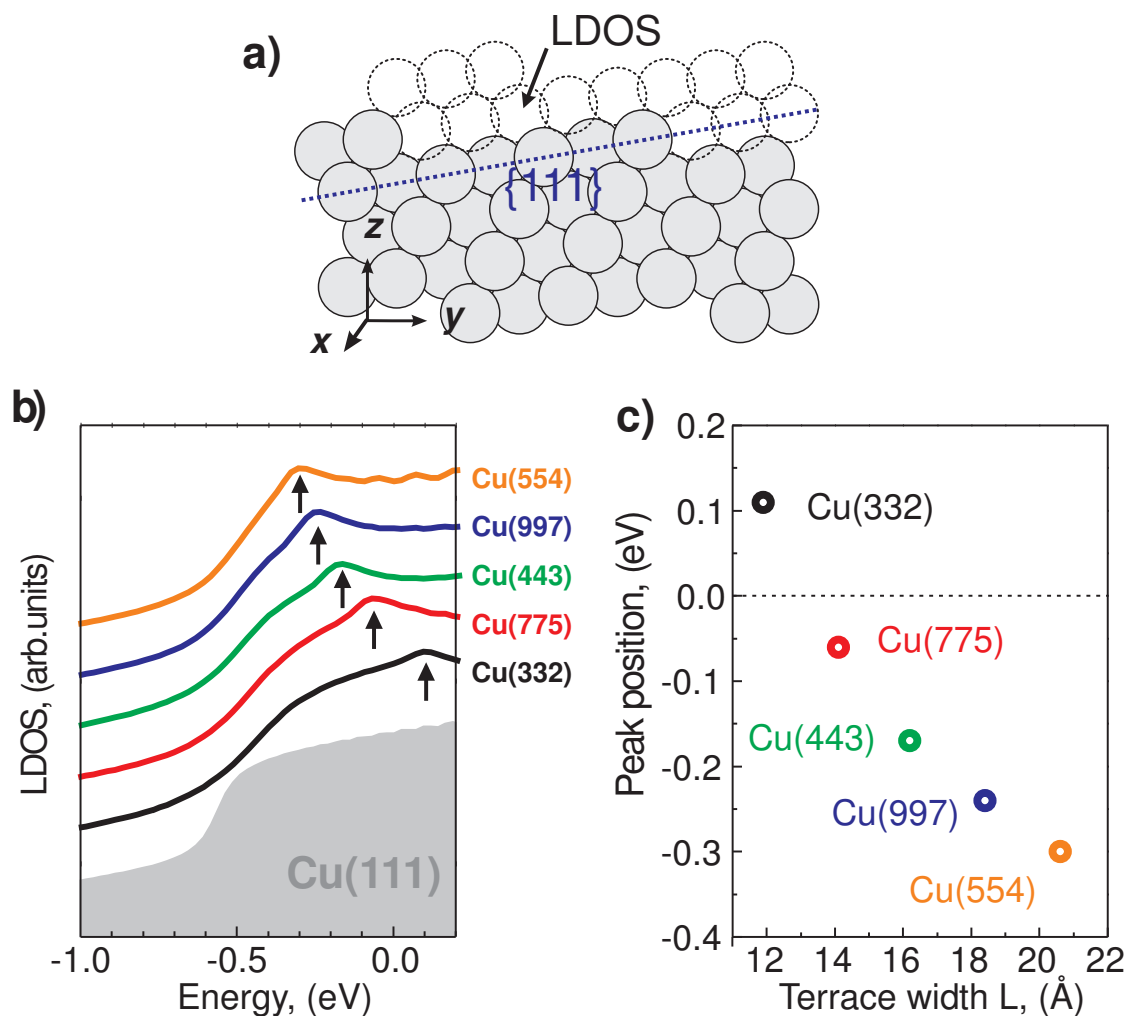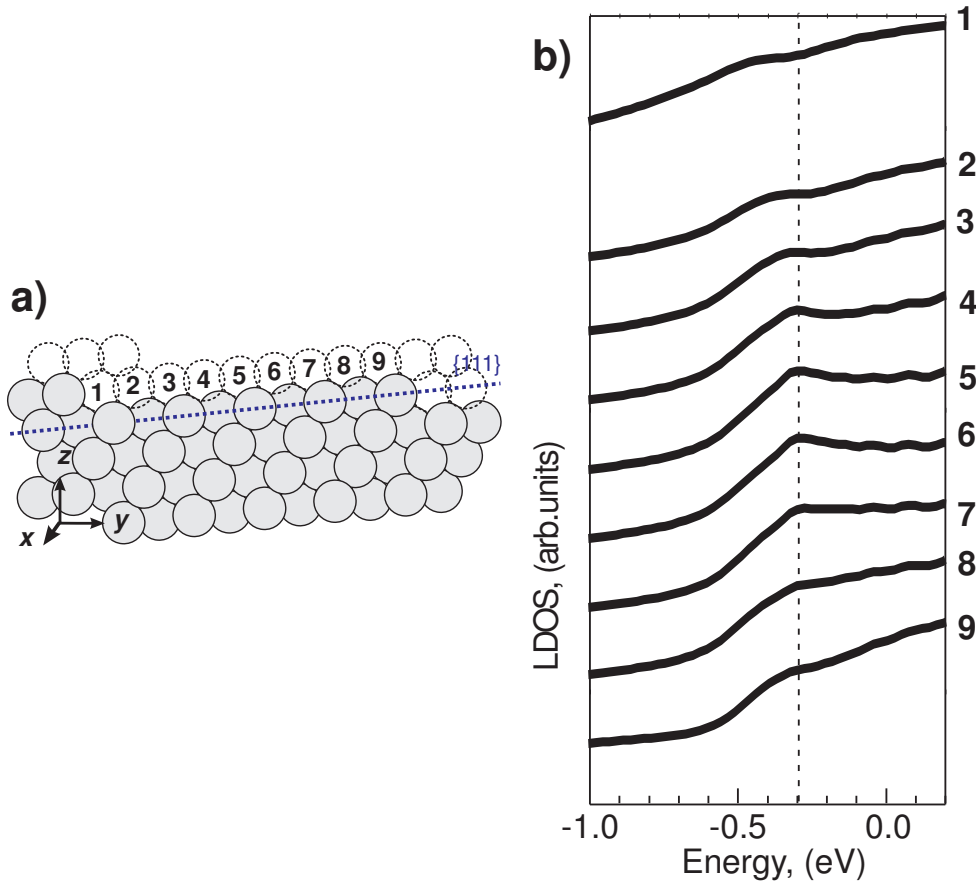
**Figure 4.3:** (a) An atomistic sketch of a terrace of Cu(332) surface. Dyed circles correspond to Cu atoms, empty circles stand for vacuum spheres. LDOS label points to the vacuum sphere at the center of the terrace, where the LDOS presented in (b) is calculated. (b) The LDOSes calculated at the center of terrace of Cu(111) vicinals. The onset of surface states on vicinal surfaces (color curves) is shifted to the higher energies with respect to clean Cu(111) (gray area). The arrows show positions of LDOS peaks. (c) The energy of peaks revealed in (b) is demonstrated as a function of terrace width.
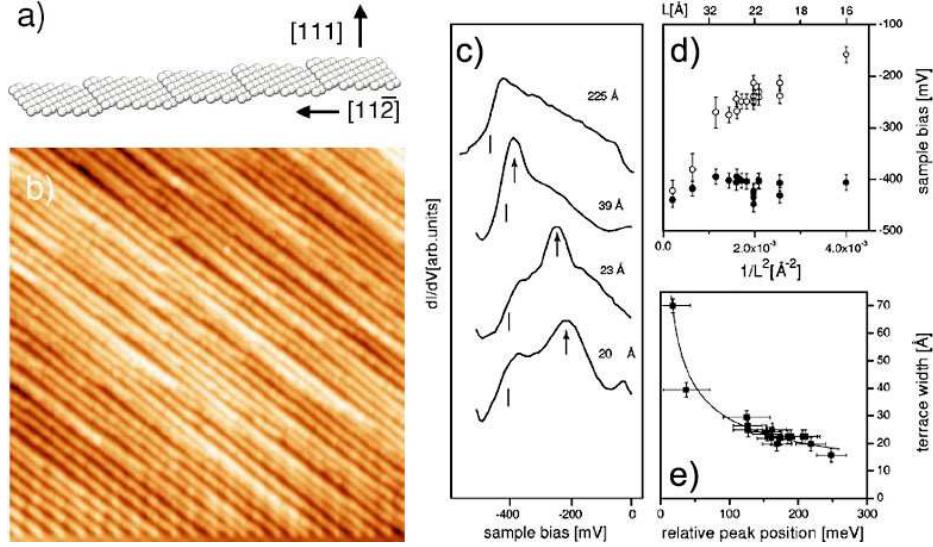
**Figure 4.4:** a) An atomistic model of the Cu(554) surface. Every {111} oriented terrace is 21 Å wide and consists of nine atomic rows. b) Topographic image of the Cu(554) surface. $810 \times 810$ Å$^2$. $V_s = 400$ mV, $I = 0.6$ nA. c) a $dI/dV$ spectra taken on terraces of different widths as indicated on the right-hand side. Straight lines denote the onset position taken from the numerical point of inflexion. Peaklike features on narrower terraces are marked with an arrow. d) Energies of onsets closed circles and peaks open circles taken from spectra similar to those in c . e) Peak energy relative to their individual onsets in d plotted against the step width. The fit corresponds to a finite 1D potential well with the barrier height as the fit parameter.

STS spectra taken on terraces of different widths by Hansmann et al. [100] are shown in Fig. 4.4(c). The widest terrace actually can be treated as flat surface. Analysis of spectra acquired over narrower terraces immediately yields two common features: (i) the surface-states like onsets of the spectra preserve but they are shifted towards the higher energies (onset positions are denoted in Fig. 4.4(c) with straight lines); (ii) a broad but a very distinct peak appears at various energies above the band bottom depending on the terrace width (peaks are marked in Fig. 4.4(c) with arrows). Energies of onsets and peaks for terraces of various widths are plotted Fig. 4.4(d). The shifted surface-states-like onset indicates that Cu(111) extended 2D surface states still exist on the considered vicinal surfaces, only partially affected by the finite transparency of the step superlattice. This observation actually supports the dispersion relation for collective superlattice states of 1D KP model (4.4). The second feature, i.e. the peak, can originate either from (i) a collective coupling of propagating states to barriers at all the steps, or (ii) from local confinement of surface electrons to the terraces. The peak should appear at the same energy for all terraces if the overall "superlattice" effect dominates. Experiments, however, traced a clear dependence of the peak position on the terrace width typical for particle-in-a-box model, i.e. $E \propto L^{-2}$ [Fig. 4.4(e)], even if measurements were performed at adjacent terraces with different width [100]. This assumes that the peak is formed by states which properties are determined by local confinement on a single terrace.

It is important to note here, that our *ab initio* results are obtained for the infinite array of the equivalent terraces separated by steps. Such a system actually should be treated as a superlattice and hence the contribution to the peak of the overall effect of all the

**Figure 4.5:** (a) The atomistic sketch of a terrace of Cu(554) surface. Each vacuum sphere on the terrace is enumerated. The LDOSes calculated in all the terrace sites are demonstrated in (b). The LDOS peak revealed at the terrace center is absent at the step ledge (position and curve 1 ) and at the terrace edge (position and curve 9). Such a spatial localization of the electronic states gives an idea on the confinement of surface state electrons to the terrace similar to the 1D KP model.

confining potentials is significant. Despite this fact we found a good agreement between our *ab initio* and experimental peak positions. In particular, for Cu(443) and Cu(554) the calculated peaks positions are equal respectively $-0.17\ eV$ and $-0.3\ eV$, and corresponding experimental values are approximately $-0.15\ eV$ and $-0.25\ eV$. Further analysis revealed, that the peak was the most pronounced at the canter of the terrace. To illustrate it we plot in Fig. 4.5 the LDOSes taken at different sites along the terrace of Cu(554) surface. The peak is absent at the step ledge (curve 1 in Fig. 4.5) and at the terrace edge (curve 9 in Fig. 4.5). This spatial localization of the electronic states again leads us to an idea on the confinement of surface state electrons to the terrace. The ratio of contributions to the LDOS peak arising due to local confinement and overall superlattice effect can be rationalized in terms of the strength of confining potential at the step edges. It can be done within the 1D Kronig-Penney model (4.4) [16, 99].

## 4.2.2 The Kronig-Penney model

An ideal stepped surface consists of an infinite number of terraces separated with monatomic steps. Bürgi et al. [19] clearly demonstrated that each step could be modeled by a repulsive potential with a finite transparency. Since the vicinal surface is periodic and one step is a copy of another, the surface state wave function $\Psi(x)$ must obey the Bloch's theorem (1.4):

$$\Psi(x+L) = \Psi(x)\exp(\mathrm{i}k_\perp L), \tag{4.1}$$

, where $L$ is the terrace width, $x$ is defined on the axis parallel to the surface perpendicular to the steps and $k_\perp$ is the projection of the wave vector on this axis. Such a formulation recalls the nearly free electron approximation (see section 1.2) for the electrons motion in the weak periodic potential. The simplest model, suggested by Kronig and Penney in 1931 [101], treats each step as $\delta$-function potential of strength $U_0 a$. The wave function between two adjacent steps can be written as

$$\Psi(x) = Ae^{\mathrm{i}qx} + A'e^{-\mathrm{i}qx} \tag{4.2}$$

In any other region wave functions can be determined by (4.1). Matching wave functions of reflected and transmitted electrons at each side of the barrier, one can derive for the KP model the following dispersion relation:

$$\cos(qL + \phi) = |T|\cos(k_\perp L), \tag{4.3}$$

or in terms of energy

$$E_\perp(k_\perp) = \frac{\hbar^2}{2m^* L^2}\left[\cos^{-1}\left(|T|\cos(k_\perp L)\right) - \phi\right]^2 + E_0, \tag{4.4}$$

where $m^*$ is the effective mass of the surface states electrons, $E_0$ is the bottom of the surface state band on the flat surface. The module of energy-dependent transmission coefficient $|T|$ and phase shift $\phi$ can be obtained using the potential barrier strength $U_0 a$ as:

$$|T|^2 = 1/\left(1 + (q_0/q)^2\right), \tag{4.5}$$

$$\phi = -\tan^{-1}(q_0/q), \tag{4.6}$$

$$q = \sqrt{(2m^*/\hbar^2)(E - E_0)} \tag{4.7}$$

where $q_0 = (m^*/\hbar^2) \cdot U_0 a$. As it has been already demonstrated for NFE approximation (Fig. 1.1), the 1D KP model results in the appearing of small gaps between two bands at $k_\perp = n\pi/L$, $n \in \mathcal{N}$ and the upward shift of the band bottom (see equation (4.4)). If the effective mass $m^*$, the band bottom $E_0$ and length of terrace $L$ are defined, then unknown potential barrier strength $U_0 a$ can be fitted to experimental or *ab initio* data to reproduce the observed shift of the surface state band bottom. Obtained values of the potential barrier strength $U_0 a$ can be then used in analysis and interpretation of the surface states confinement on vicinal surfaces.

## 4.2.3 Surface states bands: spectral density maps

To obtain surface state band bottoms we plot SDMs calculated at the center of all the considered terraces. Fig. 4.6(a) shows the SDM of the Cu(443) surface. The band is

back folded exactly at the boundaries of the supperlattice Brillouin zone (reciprocal vectors $k_\perp = \pi/L$) . Since the KKR Green's function method does not operate with wave functions and the bands can not be obtained explicitly, the surface state band bottom should be extracted from the SDMs by the fitting procedure. Below we describe the fitting algorithm we developed for this work.

Spectral density (SD) $A(\mathbf{k}, E)$ is a function of momentum $\mathbf{k}$ and energy $E$ which has local maxima at bands. It is possible to trace the band structure by finding maxima of SD. In general such a procedure is not trivial because bands can cross each other or be degenerate at some points. We have only one surface state band, so maxima tracing is expected to yield reliable results.

The KKR code is tuned to output spectral densities as a 2D array, i.e. as a matrix $A_{k_i, E_j}$ where row $i$ corresponds to momentum $k_i$ and column $j$ corresponds to energy $E_j$. The band energies are, thereore, to be interpolated from these discrete data. Note, that it is unnecessary to consider the whole band to obtain the surface state band bottom. Only a part of SDM in the proximity of the band bottom should be considered. Such a part of the Cu(443) SDM used is demonstrated in the bottom panel of Fig. 4.6.

At first, for a set of a fixed $\{k_i\}$ we determine a set of energies $\{E_{k_i}\}$ where SDM $A(k_i, E_j)$ gets its local maxima (Fig. 4.6):

$$E_{k_i} = \max_{E}\{A_{k_i}(E)\} \tag{4.8}$$

Because we use a rather dense energy mesh $\{E_j\}$ maximum energies $E_{k_i}$ should not be bound to discrete energy set $E_j$ but can be found more accurately for all the $\kappa \in \{k_i\}$ by means of parabolic interpolation of discrete SDM data $A_{\kappa, E_j}$ in the proximity of its maximum value. Blue curve shown in Fig. 4.6 is a crossection $A_\kappa(E)$ of the 2D SDM $A(k_i, E_j)$ at the fixed moment $\kappa \in \{k_i\}$. The set of maximal values of spectral density $\{k_i, E_{k_i}\}$ is demonstrated in the bottom panel of Fig. 4.6 by blue points. Now we have the surface state band described by a set of points $\{k_i, E_{k_i}\}$ in momentum-energy space. This set is fitted to the N-th order polynomial function $P_{\{c\}_N}(k) = \sum_{l=0}^{N} c_l k^l$ in $L^2$ space:

$$\{c\}_N = \min_{\{c\}_N} \left\| E_{k_i} - \sum_{l=0}^{N} c_l k_i^l \right\|_{L_2} \tag{4.9}$$

The result of this fit for Cu(443) surface is demonstrated in the bottom panel of Fig. 4.6 with a green curve. The band bottom energy (shown with the red point in the bottom panel of Fig. 4.6) is obtained as the minimum value of the polynomial $P_{\{c\}_N}(k)$. The resulting error is estimated to be within several meV.
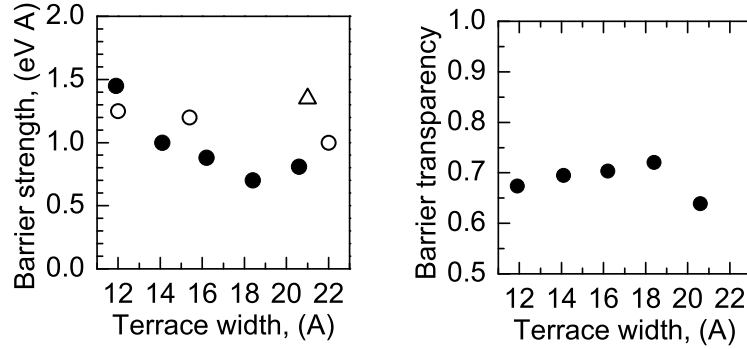
The potential barrier strength $U_0 a$ calculated from (4.4) is plotted in Fig. 4.8a as a function of the terrace width with solid circles. The values determined by Sánchez et al. [99] and Hansmann et al. [100] are also shown in Fig. 4.8a. In agreement with available experimental data the barrier strengths are around 1 eV Å and display a growth for smaller terrace widths [103]. One can see that the barrier strength exhibits the minimum approximately at the terrace width equal to 18 Å. The increase of the barrier strength at large value of the terrace width assumes that surface states get more confined to the terrace, and therefore, it can be treated as the evidence of the transition in the character of the states. Corresponding barrier transparency (4.5) demonstrated in Fig. 4.8(b) also exhibits an abrupt drop for terrace width 21 Å.
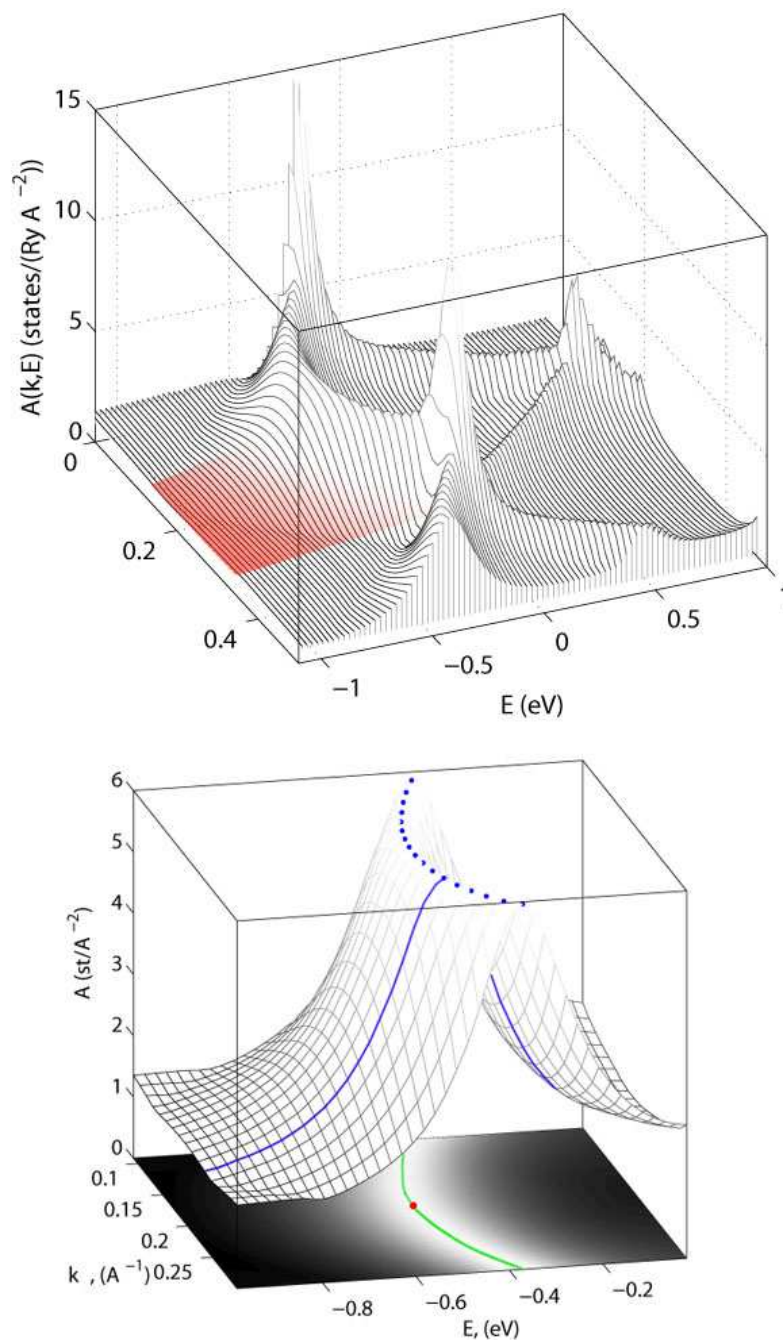
**Figure 4.6:** SDM $A_{k_i, E_j}$ of Cu(443). Red rectangle marks the region used in the fitting procedure. The SDM in this region is presented in the bottom panel of the figure. Blue curve is a crossection $A_\kappa(E)$ of the 2D SDM $A(k_i, E)$ at fixed moment $\kappa \in \{k_i\}$. The set of maximal values of SD $\{k_i, E_{k_i}\}$ is demonstrated with blue points. Green curve drawn on $(k, E)$ plane is the polynomial interpolation of this set. The band bottom energy shown with the red point is obtained as the minimum value of the polynomial.
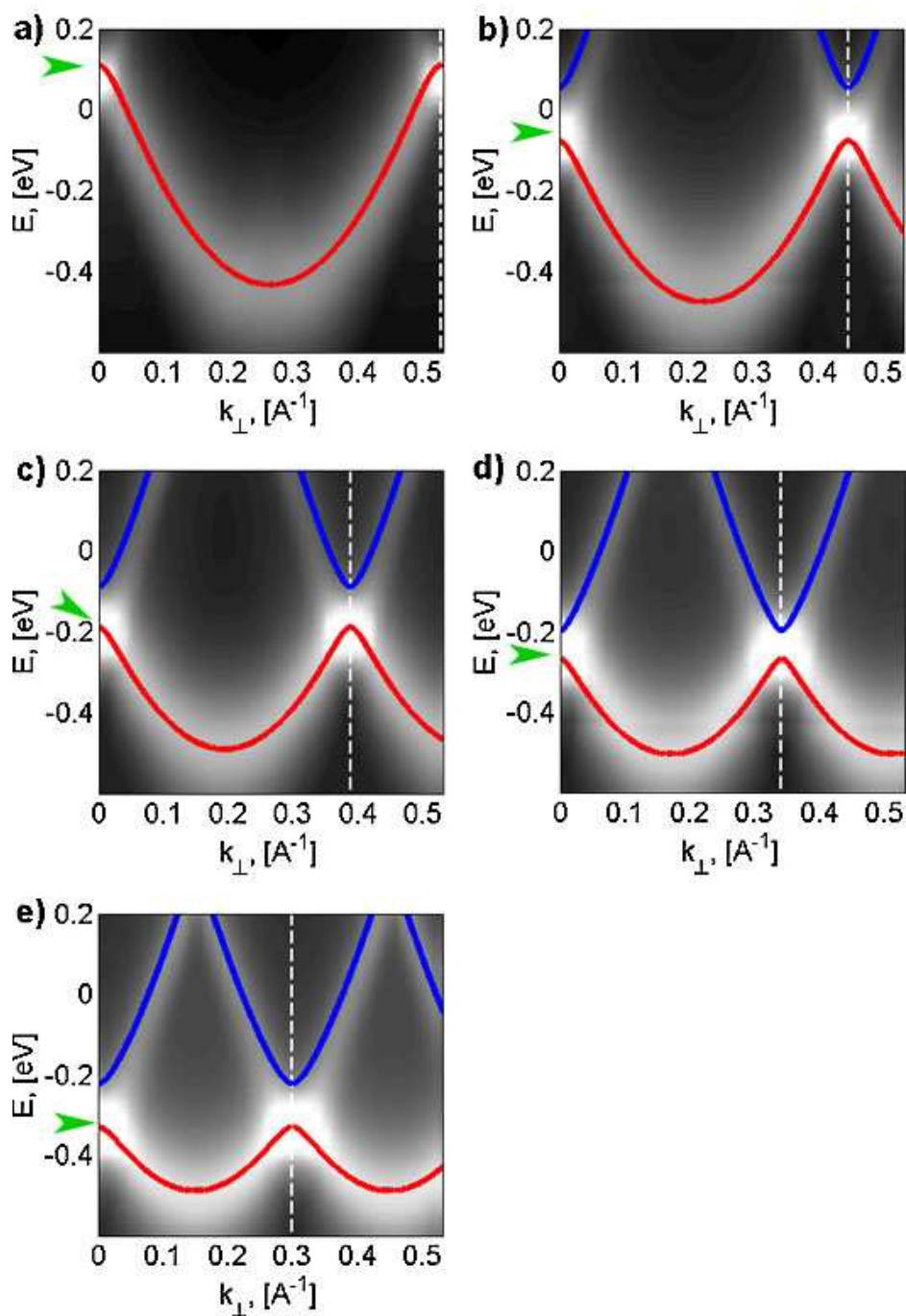
**Figure 4.7:** Spectral density maps of a) Cu(332), b) Cu(775), c) Cu(443), d) Cu(997), and e) Cu(554) surfaces calculated using KKR Green's function method. Bands are back folded exactly at boundaries of superlattice Brillouin zone ( reciprocal vectors $k = \pi/L$ are marked with the vertical dashed white lines). The 1D KP model bands are drawn by lines at the top of the spectral density maps: red solid curves correspond to the first band of 1D KP approximation, blue solid curves correspond to the second one. The green arrows correspond to the energies of the LDOS peaks. The figure is published in [102].

**Figure 4.8:** a) The potential barrier strength $U_0 a$ as a function of terrace width calculated from the SKKR ab-initio input according to (4.4) (solid circles), determined experimentally by Sánchez et al. [99] (open circles) and Hansmann et al. [100] (triangle). b) Barrier transparency as a function of terrace width calculated from the SKKR ab-initio input.

The 1KP model in our case can be directly compared to *ab initio* results. The KP bands constructed according to the dispersion relation (4.4) are visualized in Figs. 4.7(a-e) upon the corresponding SDMs. The first KP bands fit the *ab initio* SDMs surprisingly well. On the other hand, the 1D KP model unambiguously states the existence of gaps betwen bands. These KP gaps are clearly visible at $k_\perp = n\pi/L$ for all examined stepped surfaces. SDMs obtained from *ab initio* calculations, however, have no gaps at these points.

To explain this contradiction, let us consider several possible natures of the electronic states on vicinal surfaces. The first assumption is that we deal with confined states. Confined states should be nondispersive, which is not true in our case: the first bands are parabolic-like. Such a band shape can be a signature of a superlattice electronic states. But it also not the case because there are no gaps between the first and the second KP bands. The gap is closed due to overlap of surface and bulk states at step edges predicted by Ortega et al. [103]. Surface states on vicinal surfaces with narrow terraces should be treated as surface resonances rather than confined states.

## 4.3   Decorated stepped surfaces

Let us now turn to the results on decorated Cu(111) vicinals. The main goal here is to study by *ab initio* methods the effect of magnetic wire on the confined surface states . Although DFT does not account for properties of dynamical origin, it is an accurate method to determine static quantities. Thermal fluctuation may act to destroy a static magnetic order in the absence of an external field. However, if fluctuations are rather slow, nanowires would behave as magnetic ones for many practical purposes.

### 4.3.1   Effect of decoration on electronic states of stepped surfaces

In the presence of adsorbates on stepped surfaces new interesting phenomena can occur. Equidistant steps of vicinal surfaces provide a natural pattern for self-assembling of low dimensional nanostructures. In particular, Fe stripes were observed on Cu(111) [94]; Co wires are reported to grow on Pt(997) [96]. Magnetic properties of such low dimensional nanostructures significantly depend on various conditions and are the object of intensive research [104, 105, 106]. On the other hand, such nanostructures may affect a confining potential at steps of vicinal surface changing surface states. For instance, CO molecules adsorbed at step edges significantly reduce confining potentials [107]. Shiraki and coworkers have recently reported on the same effect of Fe adatoms on surface states of Au(111) vicinals. [97, 108]. They evaporated Fe adatoms on vicinal Au(111) surface and revealed the formation of Fe nanowires at step ledges. Figure 4.9 shows an STM image taken on the Au(455) at the Fe coverage of 0.04 ML. Atomically resolved Fe monatomic wires adsorbed at the lower corners of the {111} steps are clearly observed [97]. Figures 4.10(a) and 4.10(b) show the angular distributions of photoemission spectra measured in the direction perpendicular to the steps before and after the step decoration with Fe, respectively. The emission angle $\Theta$ was measured with respect to the surface normal direction. As marked with vertical bars in Fig. 4.10(a), two peaks with only a little dispersion were clearly observed on the clean Au surface. These discrete energy levels were described as the electronic states confined in quantum wells between steps. They assumed that the step potential barrier could be possibly modified by Fe adatoms and examined the surface electronic structure at room temperature by means of ARPES.

At the Fe coverage of 0.04 ML, the spectra changed strikingly as shown in Fig. 4.10(b). The peak near the Fermi level showed parabolic dispersion instead of the two peaks with little dispersion. That indicated that the electron propagation across the decorated steps on the vicinal surface was more free-electron-like and suggested that the step decoration with Fe decreases the potential barrier leading to a breakdown of the electron confinement. Figure 4.10(b) also shows a downward energy shift of the surface state band bottom compared to Fig. 4.10(a).

A further confinement of 1D quantum well states can be achieved on vicinal surfaces. The general strategy is to place somehow the barriers across the terraces. This can be done by STM manipulations [100], exploiting self-organization [109, 110] or even simply taking the surfaces with uneven steps [111]. As a result surface state is confined or partially confined in the direction parallel to steps. This allows to tune the electronic properties of the surface.

### 4.3.2   Spin-polarized surface state on decorated stepped surfaces

We performed calculations for Cu(332), Cu(775), Cu(443), Cu(997), and Cu(554) surfaces decorated with monatomic Fe wires. Figure 4.11(a) demonstrate the atomic sketch of the decorated Cu(332) surface. Fe row is placed at the step ledge of clean surfaces. The total LDOS calculated at the center of terraces are shown in Fig. 4.11(b). The peaks marked in Fig. 4.11 by arrows are blurred but still visible and the LDOS onset is shifted *downward*, i.e. in the opposite direction to the clean Cu(111) vicinals. The minority and majority density of states are demonstrated in Fig. 4.11(c),(d). It is evident that the surface states on decorated Cu(111) vicinals become spin polarized. The blurred peak in the total density of states comes from the majority part, which seems to be not much affected by the presence
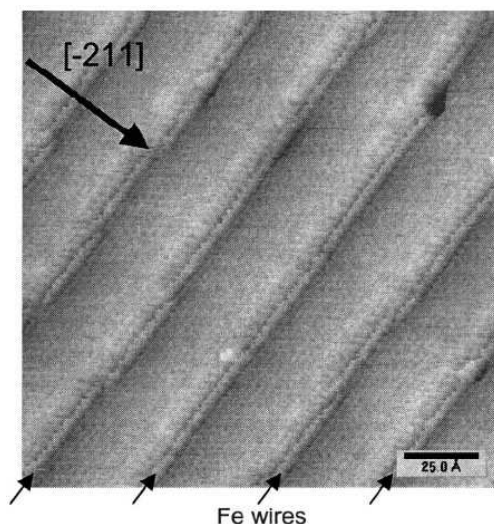
**Figure 4.9:** One-dimensional Fe nanostructure grown on the Au(455) surface (0.04 ML). The large arrow indicates the descending direction of the steps. The figure is taken from [97].
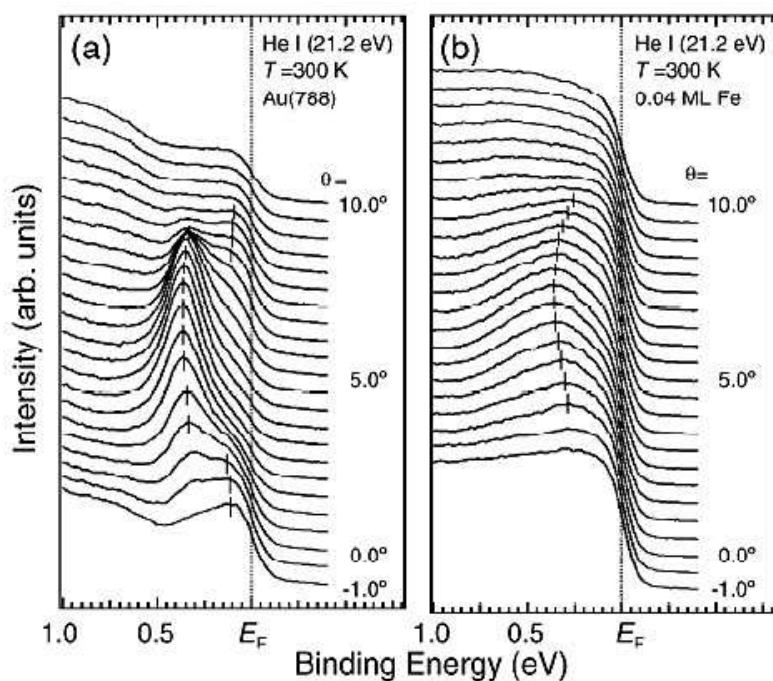


**Figure 4.10:** Angular distributions of photoemission spectra near the Fermi level measured in the direction perpendicular to the step array: (a) Au(788) and (b) 0.04 ML Fe/Au(788). The emission angle Θ is measured with respect to the surface normal. The figure is taken from [97].

of Fe wire. The minority density of states for all the examined vicinal surfaces has no such peak, but a new one appears at -0.6 eV. To reveal the origin of the peak at -0.6 eV we performed a systematical study of the spatially resolved density of states across terraces of considered vicinal surfaces. The majority and the minority LDOSes calculated along the
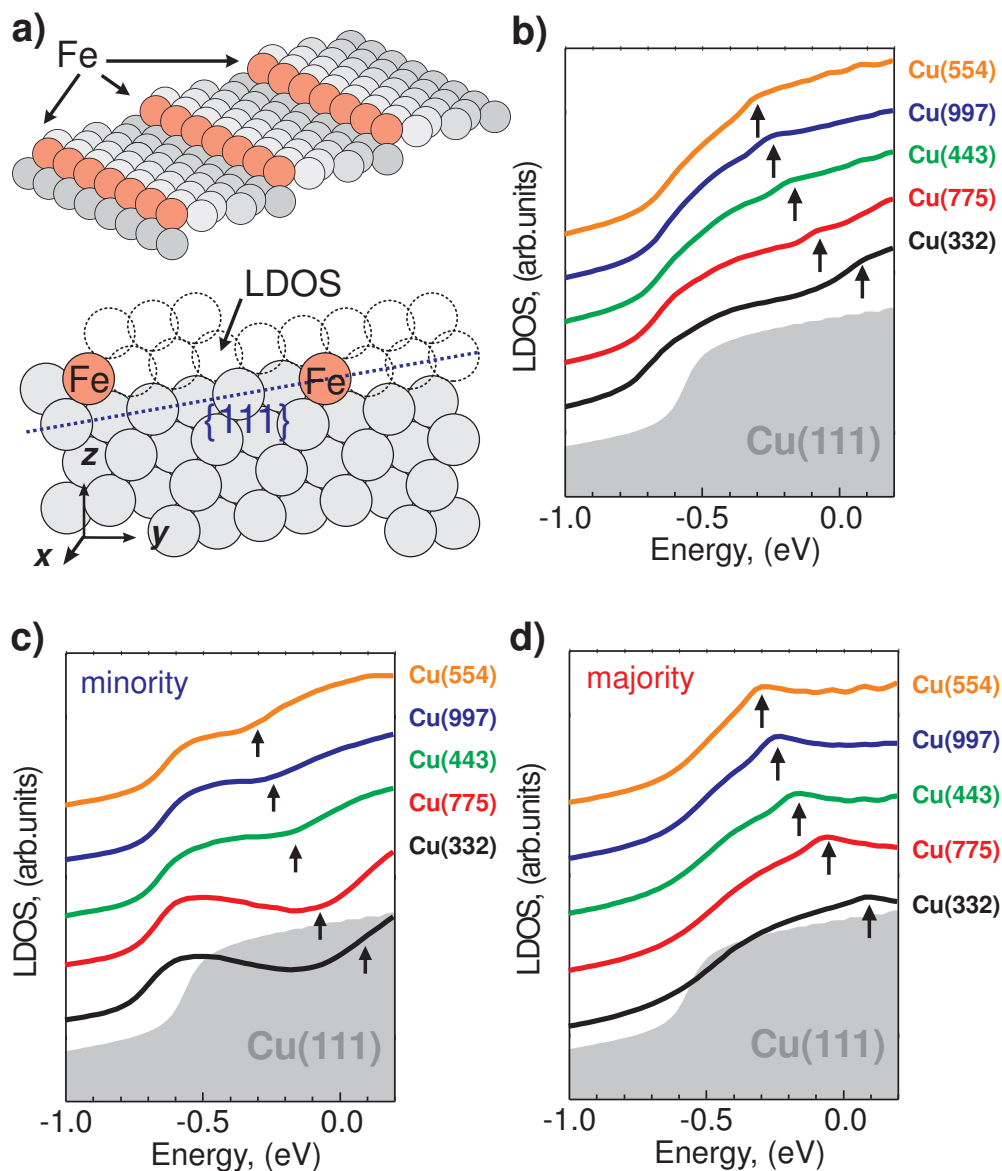
**Figure 4.11:** (a)The atomic sketch of the decorated Cu(332) surface. Fe atoms placed at the step ledge of clean surface are colored red. The total LDOS's calculated in the center of terraces are shown in (b). The peaks marked in Fig. 4.3(b) by arrows are blurred but still visible and there is a downward shift of the LDOS onset. The minority and majority density of states are demonstrated in (c) and (d). The blurred peak in the total density of states comes from the majority part, which seems not to be affected much by the presence of Fe wire. The minority density of states for all the examined vicinal surfaces exhibits a new peak at -0.6 eV.
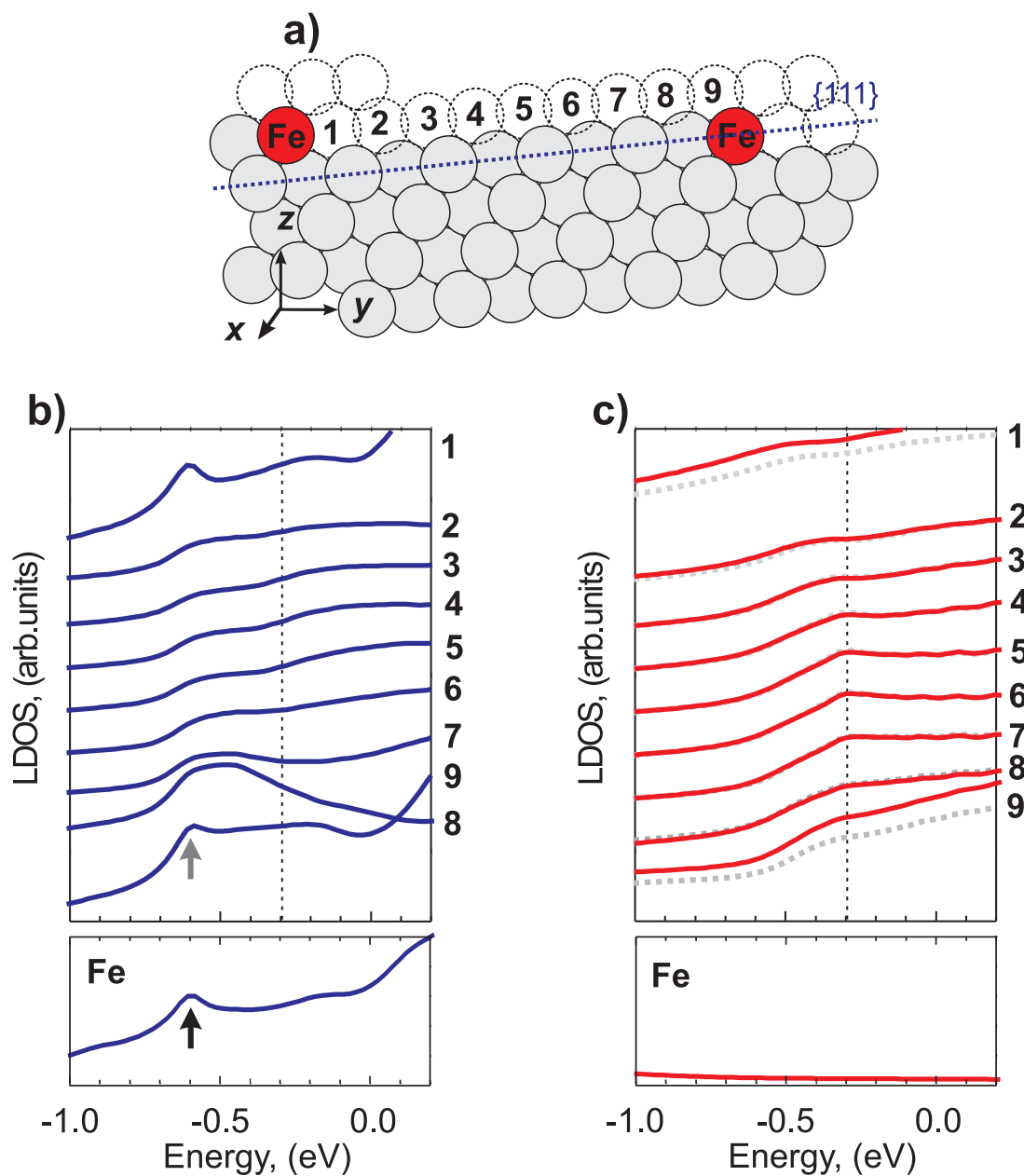
**Figure 4.12:** (a) The atomistic sketch of a terrace of Cu(554) surface. Each vacuum sphere on the terrace is enumerated. The minority and the majority LDOS's calculated in all the terrace sites are demonstrated in (b) and (c) respectively. The majority LDOS (red curves) is not affected much in comparison with the case of clean Cu(554) surface (dashed gray curves). The minority surface states hybridize with the quasi-atomic state of Fe wire (peak at -0.6 eV) and get localized at the Fe wires, thus suppresing the confinement.
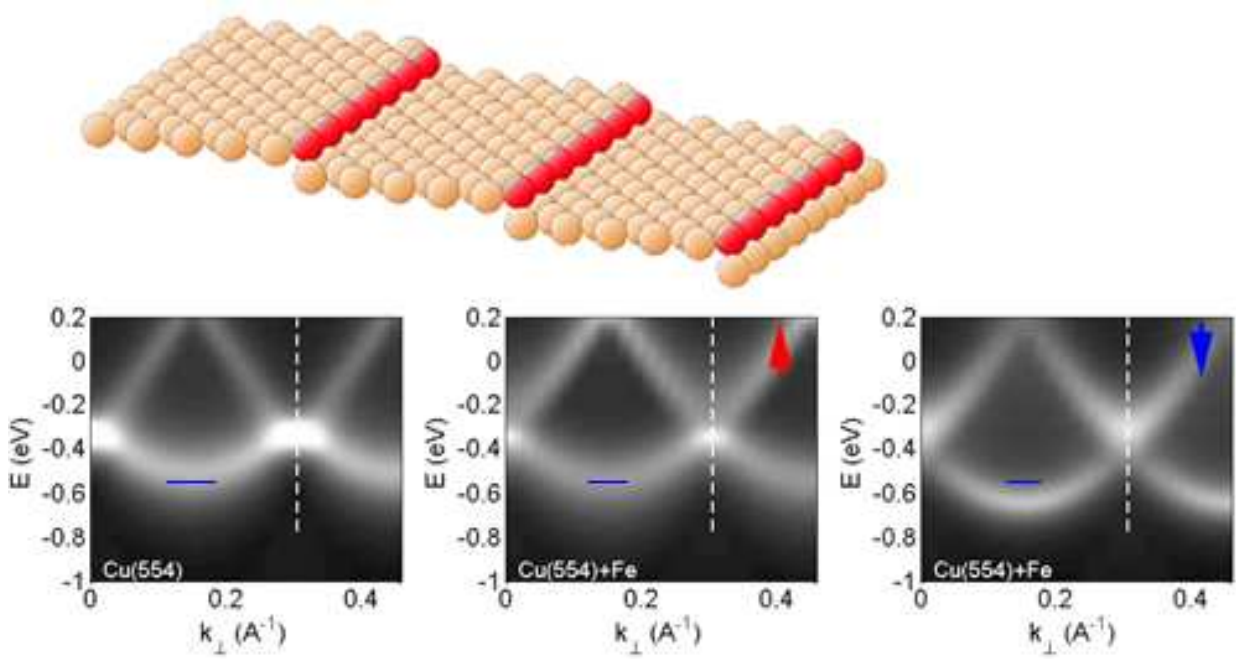
**Figure 4.13:** The comparison of the majority and the minority SDMs calculated in the terrace center of the decorated Cu(554) surface (shown in the upper panel) with the SDM of clean Cu(554) surface. Blue strokes mark the energy of the Cu(554) surface state band bottom. The majority states of the decorated surface are not affected much, while the minority exhibit downward shift of the band and redistribution of the charge density along the band.

terrace of Cu(554) surface decorated with Fe rows are plotted in Fig. 4.12 as an example. The majority LDOS [Fig. 4.12(c) red curves] is not affected much in comparison with the case of clean Cu(554) surface (dashed gray curves in Fig. 4.12). The majority states at the peak energy get the maximal density in the center of terrace. The minority states *vice versa* exhibit the maximal density at the Fe wires. This immediately gives an idea of some kind of localization of surface state electrons at Fe wires. To prove it we plot in Fig. 4.12 the density of states at atom of Fe wire. One can observe at -0.6 eV the resonance of $d$ character. Thus, the localization of surface states at Fe wires is determined by the resonant scattering of the $s$-$p$ electrons at $d$-quasi-atomic states of Fe row. The $d$-derived surface state resonance at $-0.6$ is not affected by the terrace width because terraces are wide enough to cancel direct interaction between Fe rows, so this energy is determined by the interaction of Fe atoms within the same row.

It is not clear yet if the onset of minority states is the evidence of a new modified surface state, or is a kind of bound state. To clarify it we demonstrate the spin-polarized SDMs of the decorated Cu(554) surface in Fig. 4.13. Dispersive bands preserves in both spin channels, however, the minority surface state band bottom is shifted downwards with respect to the position on flat Cu(111) surface. The density of minority electrons is significantly redistributed in comparison to clean Cu(554) surface: the upper edge of the first band is depopulated and the density of the lower edge of the second band is increased. A simple analysis of the spatial distribution of these states within the 1D KP model [101] immediately yields that populated states from the lower edge of the second band reach their maximal density in the proximity of the barriers, while the states from the upper edge of the first

band have maximal density in the center of the terrace and vanishes at the barriers. Thus, decoration of the Cu(111) vicinal surfaces at step edge with Fe rows permits to control the population of the minority surface states bands. Comparison of the majority SDM to the SDM of clean Cu(554) surface confirms that the majority SDM is not affected much by the Fe row: the shape of bands is the same but electronic density is slightly redistributed.

# 4.4 Self-organized long-period 1D nanostructures on stepped metal surfaces

In the previous Section we demonstrate how decoration of stepped surfaces allow to tune their electronic properties. Now we want to address the opposite situation when electronic states on stepped surfaces promote the self organization of low dimensional nanostructures.

## 4.4.1 Substrate mediated long range adatom-adatom interaction

Monatomic rows and stripes grown at the step ledges of a vicinal surfaces [96, 112, 97, 108, 94, 95, 113, 89, 114] are stabilized by a direct bonding between the atoms of 1D nanostructure and substrate. Usually, interatomic distances in such low-dimensional systems are close to the intrinsic nearest-neighbor spacing. However, there could be substrate-mediated long-range interactions between adatoms. These interactions are indirect and may be mediated in three ways. The first is electrostatical dipole-dipole interaction. The second is elastic deformation of substrate lattice. According to the third way the adatom-adatom interaction is mediated by substrate electrons. Decay rates of all these interactions are different. First two interactions decay with separation $r$ as $1/r^3$ [115]. Decay rate of third strictly speaking depends on the dimensionality of the system. Indeed, as was demonstrated by Friedel, electronic density oscillations appeared around an impurity introduced into a metallic host. The period of oscillations was shown to depend on the wave vector $\mathbf{k}_F$ of the electrons at the Fermi surface [84]. The same formalism can be applied to adatoms on surfaces. Oscillations of the electronic density caused by one adsorbate can influence the binding energy of another adsorbate. Lau and Kohn demonstrated that interaction between two adatoms mediated by bulk electrons decayed as $\propto 1/r^5$ [116], they also predicted that in 2D systems interaction fell off much more slowly, as $\propto 1/r^2$ [116, 117]. Hylgaard and Person examined the indirect interaction mediated by a Shockley surface-state band between adsorbates on the (111) face of noble metal surfaces in the presence of bulk electrons [118]. They stressed the importance of screening by the finite density of the surrounding bulk (conduction-band) electrons. This bulk screening permitted them to obtain a simple (but non-perturbative) description of the adsorbate-induced scattering within the surface-state band. In the asymptotic region of large adsorbate separations $r$ they provided the analytical estimate:

$$E_{int}(r) = -\varepsilon_F \left( \frac{2\sin{(\delta_F)}}{\pi} \right)^2 \frac{\sin{(2k_F r + 2\delta_F)}}{(k_F r)^2} \tag{4.10}$$

Oscillations of the surface state density can be detected by means of STM/STS measure-
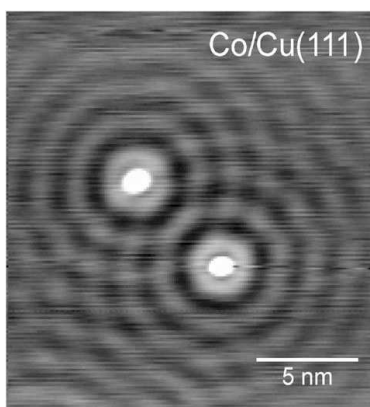
**Figure 4.14:** Constant current STM image of two Co adatoms on Cu(111), which interact via the standing waves $I = 2$ nA, $V = -50$ mV, $T = 6$ K. The figure is adopted from [119].
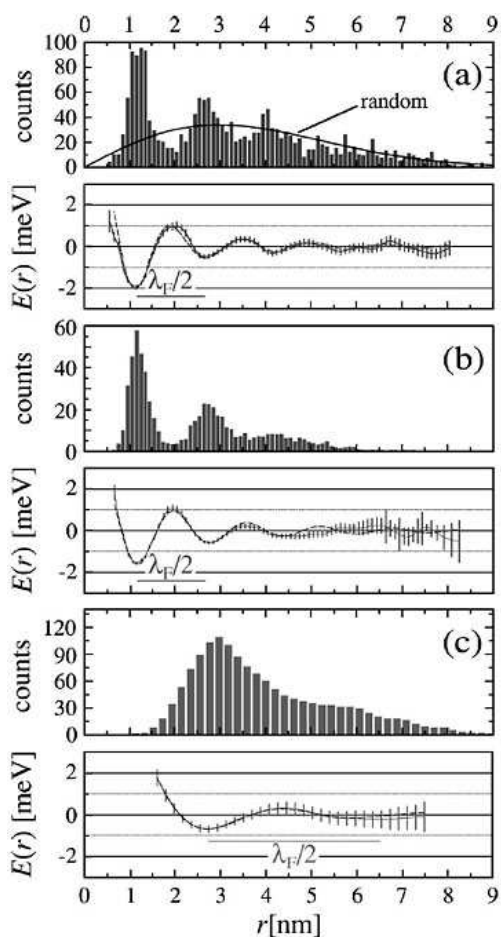


**Figure 4.15:** Histogram of (a) Cu/Cu(111), (b) Co/Cu(111), and (c) Co/Ag(111) nearest neighbor distances [ (a) coverage $\Theta = 1.4 \cdot 10^{-3}$ ML, $T = 15.6$ K; (b) $\Theta = 2.0 \cdot 10^{-3}$ ML, $T = 10.2$ K; (c) $\Theta = 4.0 \cdot 10^{-4}$ ML, $T = 18.5$ K] Fits of the data with the nonperturbative result of Ref. [118] are shown as dashed lines. The figure is taken from [115].
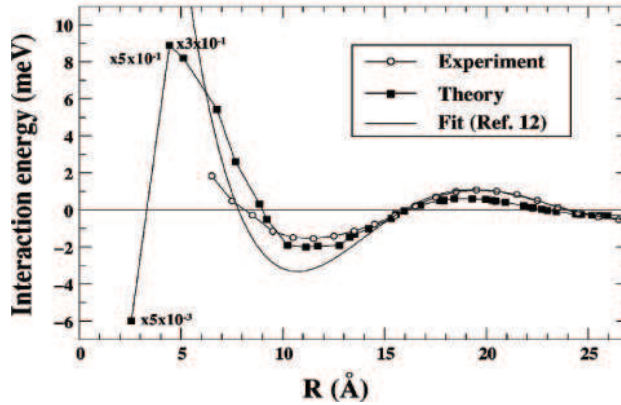
**Figure 4.16:** Experimental and calculated interaction energies between two Co adatoms on Cu(111); a fit based on the model of Ref. [118] is presented and the first three theoretical points have been rescaled. The figure is adopted from [119].

ments. Figure 4.14 demonstrates the STM image of standing wave pattern arising near two Co adatoms on Cu(111) surface. Surface state mediated long range interaction (LRI) should definitely influence the diffusion of adatoms on surfaces and may result in appearing of a long range order. STM experiments of Repp et al. [120] and Knorr et al. [115] clearly demonstrated the impact of the LRI on the adatom motion. Both scientific groups evaporated small amount of adatoms on surfaces supporting surface state, like Cu(111), Ag(111) and studied then the pairwise radial distribution function $f(r)$, i.e. the probability to find to adatoms at separation $r$ [115, 120]. The results were completely different from the case of random site occupation $f_{ran}(r)$) [115, 120]. Histograms with the number of neighbors as a function of distance $r$ and corresponding interaction energies are shown in Fig. 4.15 for Cu/Cu(111), Co/Cu(111) and Co/Ag(111). Differences $\Delta E_{int}$ in adatoms binding energies were calculated from $f(r)$ by means of Boltzmann statistics as $\Delta E_{int} = k_B T \ln\left(\frac{f(r)}{f_{ran}(r)}\right)$ [115]. All the studied interactions exhibited oscillatory behavior with the depth of the first minimum of order of one meV. To study the decay law, the obtained $\Delta E_{int}(r)$ was then fitted to eq. (4.10). Resulting curves are also shown in Fig. 4.15. The agreement between the experiment and the theory is evident.

Later on, LRI was studied by means of ab initio Green's function method [119]. Figure 4.16 shows theoretical and experimental curves as well as fit to (4.10). Ab initio calculations are in a perfect agreement with the experimental data, and predict a first minimum of the interaction energy at 1.5 meV. The theory could also provide the value of the repulsive barrier, which actually prevents dimer formation. Despite the fact that the LRI are small, they can affect atomic motion and growth processes resulting in the formation of fascinating ordered nanostructures like adatom superlattices [121] and quantum onions [122, 36].

## 4.4.2 Long-range interactions on vicinal surfaces

We have calculated the interaction energy between an Fe adatom and the step on Cu(111) for the adatom-step separation up to 4.0 nm [123]. We have considered both A-type and B-type steps on Cu(111) and found that the substrate-mediated interaction energies are essentially the same for both types of steps. Here we present only the results for B steps.
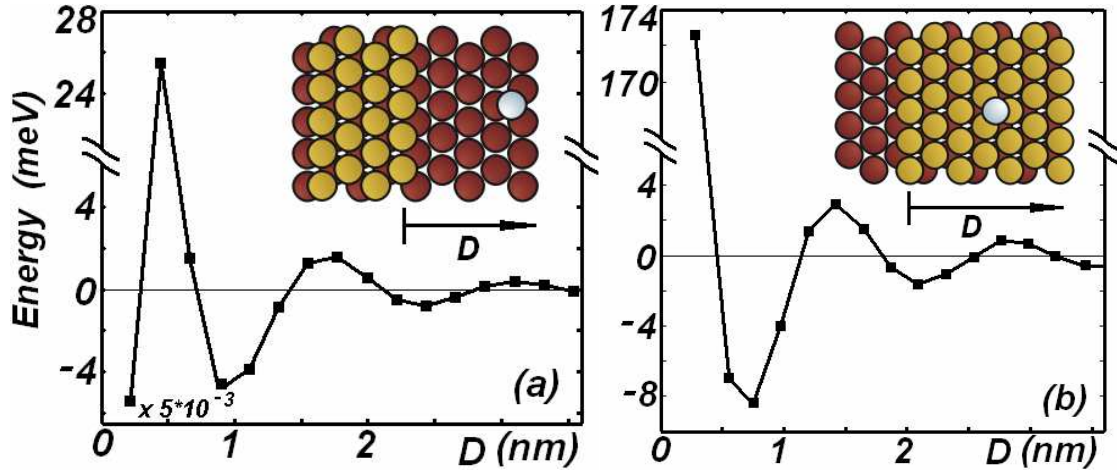
**Figure 4.17:** The interaction energy between the Fe adatom and the Cu step on Cu(111): a) for the lower terrace and b) for the upper terrace. The figure is published in [123].

We take into account the direct and substrate-mediated interactions of electronic origin. Our studies have shown that while elastic interactions can have a significant impact on an atomic motion near steps, they practically do not affect the main results presented here.

Results of our calculations for the interaction energy between the Fe adatom and the Cu step on Cu(111) for the lower and upper terraces are presented in Fig. 4.17 [123]. One can see that the interaction energy in both cases is oscillatory with a period of about 1.5 nm (half the Fermi wavelength of the surface state on Cu(111) [120, 115, 119]). The first minimum of the interaction energy is found to be $\sim 0.9$ nm on the lower terrace and $\sim 0.8$ nm for the upper terrace. But the depth of this minimum on the upper terrace ($\sim 8$ meV) is more than twice larger compared to that on the lower terrace ($\sim 4$ meV). Our results reveal that the adatom moving towards a step is repelled by the repulsive potential [Fig. 4.17]. For the lower and upper terraces, the first repulsive barrier occurs at distances of about 0.4–0.5 nm from the step. However, the strength of this repulsive potential on the upper terrace is significantly larger (173 meV) than that for the lower terrace (26 meV). The physics underlying the difference in the behavior of adatoms at the upper and lower terraces seems to be related to a redistribution of the electron-charge density at step edges as was suggested long ago by Smoluchowski [124]. The charge redistribution at step sites, with a flow of electron density from the upper step edge to the step base, is the main factor governing the differing properties between the adatom-step interaction on the upper and lower terraces near the step edge. Our calculations reveal such charge redistribution and show that the reduction of the electron density at the edge of the upper terrace reduces the screening of the direct Coulomb repulsive interaction between the Fe adatom and the step atoms. A repulsion between adatoms and the step could prevent an adatom diffusion toward the step edge at low temperatures. Note, that, due to the oscillatory nature of the adatom-step interaction, there are many different repulsive barriers for the adatom diffusion. However, our calculations show [Fig. 4.17] that such barriers e.g., for distances between 1.5 and 2.0 nm from the step edge are significantly smaller ( $< 2$ meV) than the first repulsive barrier. The above mentioned results imply that it could be possible to find a temperature at which the adatoms are trapped in attractive potential wells near steps on the upper or/and lower terraces. Fe adatoms become quite mobile on Cu(111) at temperatures larger than
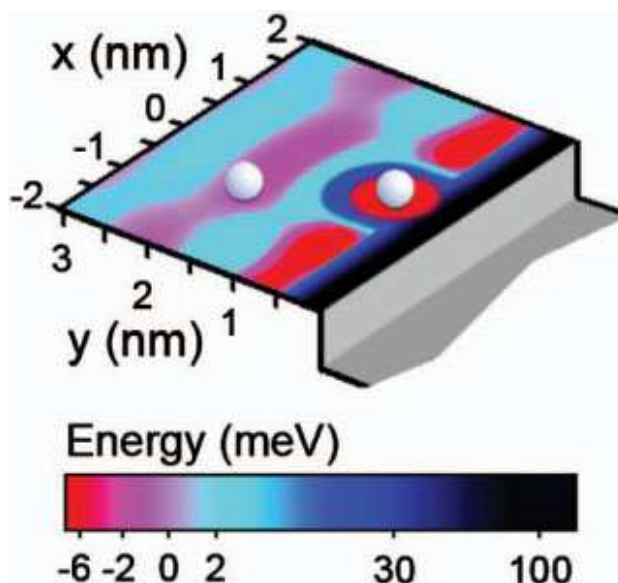
**Figure 4.18:** The potential-energy map for the Fe adatom to approach another Fe adatom trapped in the potential well near the edge of the upper terrace. [123].

10–11 K due to a small barrier for the hopping diffusion equal to 25 meV [125]. At such temperatures, adatoms can easily overcome small repulsive barriers. Using a Boltzmann distribution, $exp(-E_1/k_B T)$, where $T$ is the temperature of the substrate and $E_1$ is the depth of the first minimum of the interaction energy, one can find that the occupation probability of surface sites in the potential well near the edge of the upper terrace is about 100 times larger than that on the lower terrace at 10–13 K. In other words, it seems likely that the preferential adatom position at such temperatures is on the upper terrace at about 0.8 nm distance from the step edge. Moreover, our ab initio calculations predict that, in this region, adatom aggregation is hindered. In Fig. 4.18, we depict the potential-energy map for the Fe adatom to approach another Fe adatom trapped in the potential well near the edge of the upper terrace. The repulsive area surrounding this adatom is well seen. It is easier for the Fe adatom to approach the step edge within a distance of about 1.2 nm from the first Fe adatom. Consequently, there could be many isolated Fe adatoms near the step edge, forming an atomic string with large interatomic distances. Note that the 1.2 nm separation between adatoms is related to the first minimum of the surface-state-mediated pair interaction potential on Cu(111) . This theoretical conclusion was tested experimentally. The STM image of Fe adatoms evaporated on Cu(111) stepped surface at 12 K is demonstrated in Fig. 4.19(a). Fe atoms situated 0.8 nm away from the step edge with interatomic separation equal to 1.2 nm form quasi 1D atomic strings at step edges. Kinetic Monte Carlo simulations by Negulyaev [123] based on ab initio LRI interaction potentials yield the same 1D structure [Fig. 4.19](b).

This finding demonstrates, that surface-state electrons on stepped metal surfaces can be exploited to create a well-ordered array of atomic strings at low temperatures. Our studies reveal that such 1D nanostructures are stabilized by surface-state-mediated long-range interactions. The universal nature of the underlying physics suggests that this bottom-up approach for an adatom self-organization may be of general importance for the growth of 1D nanostructures on different metal substrates supporting an electronic surface state.
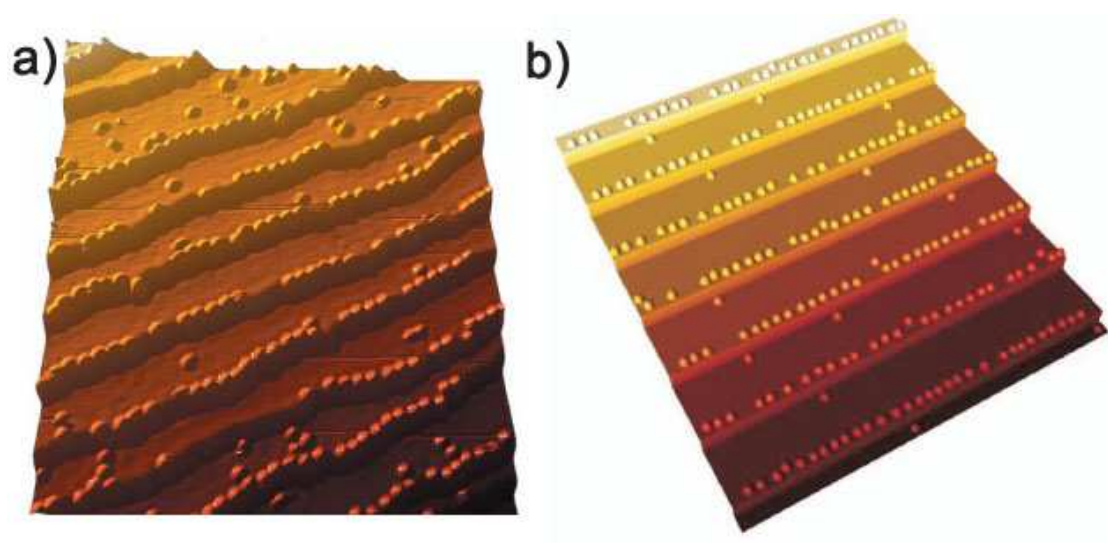
**Figure 4.19:** a) The STM image of Fe atomic strings on a vicinal Cu(111) surface. The size is $40 \times 40$ nm$^2$ and the coverage is 0.008 ML. Imaging condition: $-0.8$ V and 1 nA. b) The kMC simulations of the self-organization of Fe adatoms on a vicinal Cu(111) into atomic strings. Calculations are performed according to the experiments. The figure is published in [123].

# Chapter 5

# Surface states on Co nanoislands on noble metal substrates

Spin-polarized surface states arising on magnetic nanostructures supported on nonmagnetic substrates (e.g. Co islands on Cu(111) or Au(111) ) have attracted much attention recently [48, 49, 50, 51]. The main reason is that spin-polarized surface-state (SP-SS) may act as spin-dependent channels for transport to or from another magnetic material [126]. In Section 2.5, we described how the polarization of SP-SS can be controlled locally by an appropriate choice of the shape of Co nanoislands [50]. Here we draw attention to the decisive influence of structural properties of the Co nanoislands grown on noble metal substrates on the spin-polarized surface states. By means of ab-initio methods we demonstrate the evolution of electronic states above Co nanoislands of various sizes starting from a single Co adatom up to Co bilayers. We show the origins of majority and minority surface states. We illustrate the effect of the stacking of Co bilayer on the spin-polarized surface states. Finally, comparing surface states on Co nanoislands on Cu(111) and Au(111) substrates we figure out the essential role of the substrate in the formation of surface states and demonstrate that variation of the substrate lattice constant permits to tune surface states energies.

## 5.1 Evolution of electronic states above Co nanostructures on Cu(111)

At first we consider a single Co adatom on Cu(111) surfaces. The spin-polarized LDOS calculated 2.1 Å above an adatom is demonstrated in Fig. 5.1(a). Similarly to the case of Fe adatom considered in Section 3.3, Co atom on Cu(111) surface provokes the appearance of a bound state below the Cu(111) surface state band bottom, i.e. at energies around $-0.6$ eV. This state is spin-polarized, with small splitting caused by different strength of the majority and the minority effective potentials [47] Width of bound state resonances is determined by the its coupling to the bulk states of Cu(111) substrate [41]. The minority LDOS peak near the Fermi energy is determined by the hybridization of $s$-$p$ states with the quasi-atomic minority $d$ state of Co adatom.

The next considered structure is a compact Co trimer [Fig. 5.1(b)] . Interaction between Co atoms results in the splitting of quasi-atomic minority resonance of Co adatom: one broad minority resonance appears at $-0.45$ eV, and two peaks are situated in the minority channel above the Fermi level at 0.1 and 0.4 eV, respectively. Majority states above the
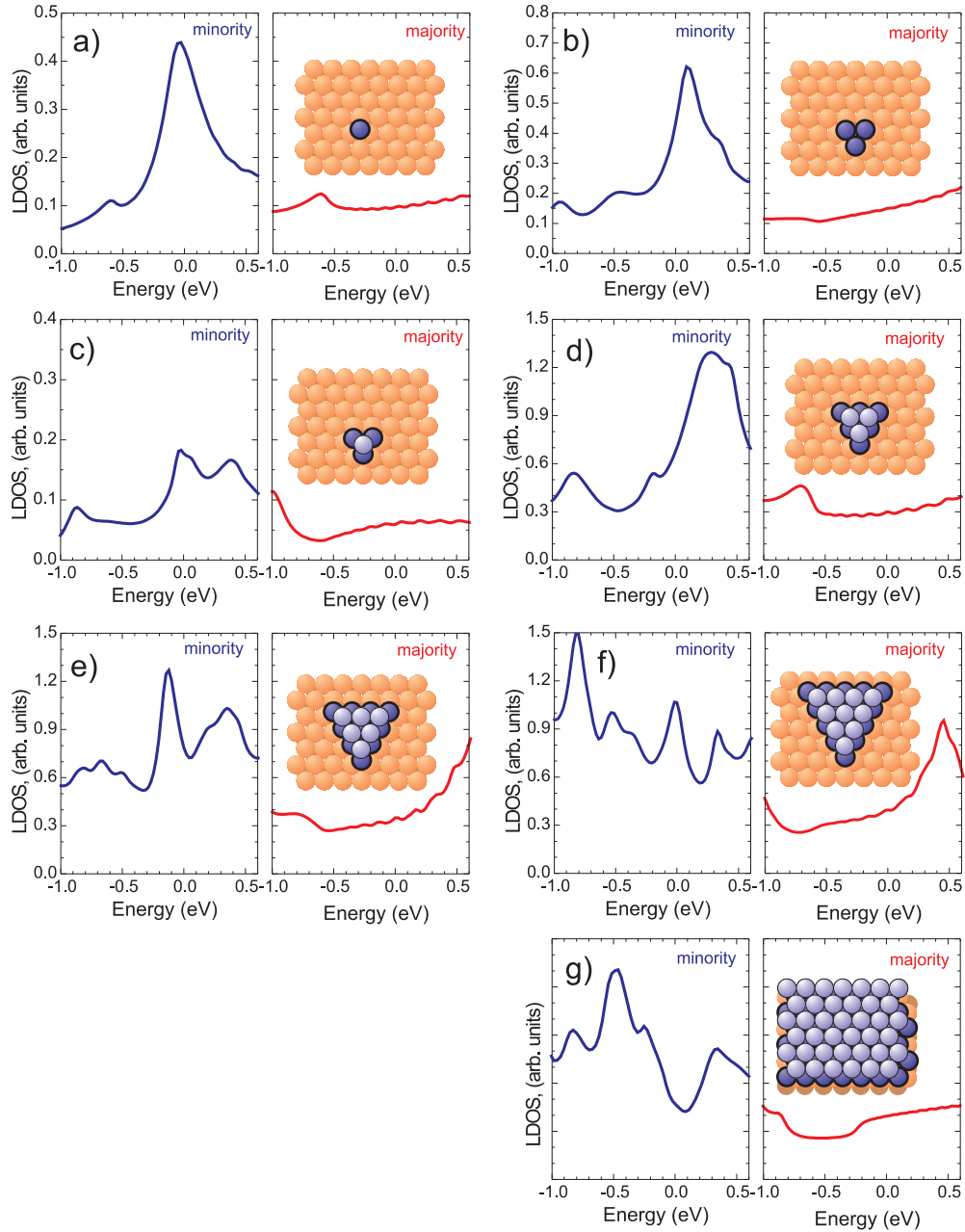
**Figure 5.1:** The spin-polarized LDOS calculated above the Co nanostructures of different size, starting from a single adatom and up to Co bilayer. The quasi-atomic minority resonance of Co adatom splits into a sequence of peaks in nanoislands of larger sizes. The occupied minority peaks appear along with the second layer of Co. The LDOS above the largest considered nanoisland exhibits a minority peak right at the Fermi level. This feature is absent in the LDOS of Co bilayer.

compact Co trimer on Cu(111) surface exhibit no features, the majority bound state becomes very broad and blurred.

The next considered structure is a pyramid built of four Co atoms, as it is shown in the inset of Fig. 5.1(c). Unoccupied peaks situated at 0.1 eV splits up and moves to the Fermi level. The further increase of the Co nanoisland size results in the appearance of the complex sequence of minority resonances below the Fermi level and splitting and shifting of the unoccupied minority LDOS peaks [see Figs. 5.1(d,e,f)]. All these resonances, thus, can be assigned as the features of double-layered Co nanostructures.

The LDOS above the largest of the studied nanoislands can be compared to the LDOS above an infinite Co bilayer shown in Fig. 5.1(g). The minority peaks visible in the LDOS of the finite-size nanoisland in Fig. 5.1(g) at $-0.8$, $-0.5$ and $-0.3$ meV can be identified in the LDOS of infinite Co bilayer at energies $-0.8$, $-0.5$ and $-0.2$ meV. The unoccupied peak at $+0.35$ eV is also present in both plots. The only difference is the pronounced minority resonance which falls in the LDOS of Co nanoisland right at the Fermi level.

A very similar feature at the Fermi level was found by Pietzsch et al in the islands' rims [51]. In constant current images rims exhibited an increased apparent height at small bias voltages. STS investigations demonstrated that the tunneling current was increased due to emerging of a new peak in the spectra. This peak is energetically located right at the Fermi energy and is found neither on the inner Co island nor on Cu substrate. It is the hallmark of the rim. SP-STM studies clarified that peak at the Fermi energy was of minority character.

## 5.2 Spin-polarized surface states on 2ML of Co on Cu(111)

### 5.2.1 Origin of the surface states on Co bilayers on noble metal substrates

To trace down the origin of the surface states peaks reveled in the calculations of vacuum LDOS we plot a layer-resolved spectral density maps (SDM). SP SDM of the interface Cu layer, two Co layers and three vacuum layers [see Fig. 5.2] calculated along $\overline{\Gamma} - \overline{M}$ direction of BZ are demonstrated in Figures 5.3 and 5.4. Corresponding LDOS's calculated in the vacuum are plotted aside the minority and the majority SDM's to clarify the origin of peaks. Each peak in Fig. 5.4 has its own label. The occupied minority peak at $-0.3$ is denoted as $p1$, the peak at $-0.45$ eV is denoted as $p2$ and the unoccupied peak at $+0.3$ eV is denoted $p3$. The majority dispersive surface state is labeled $ss$.
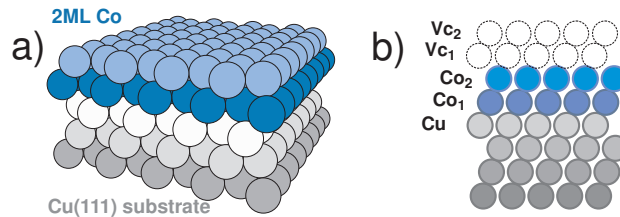


**Figure 5.2:** Scheme of layers notations used in layer resolved spectral density maps plotted in Figs. 5.3 and 5.4.
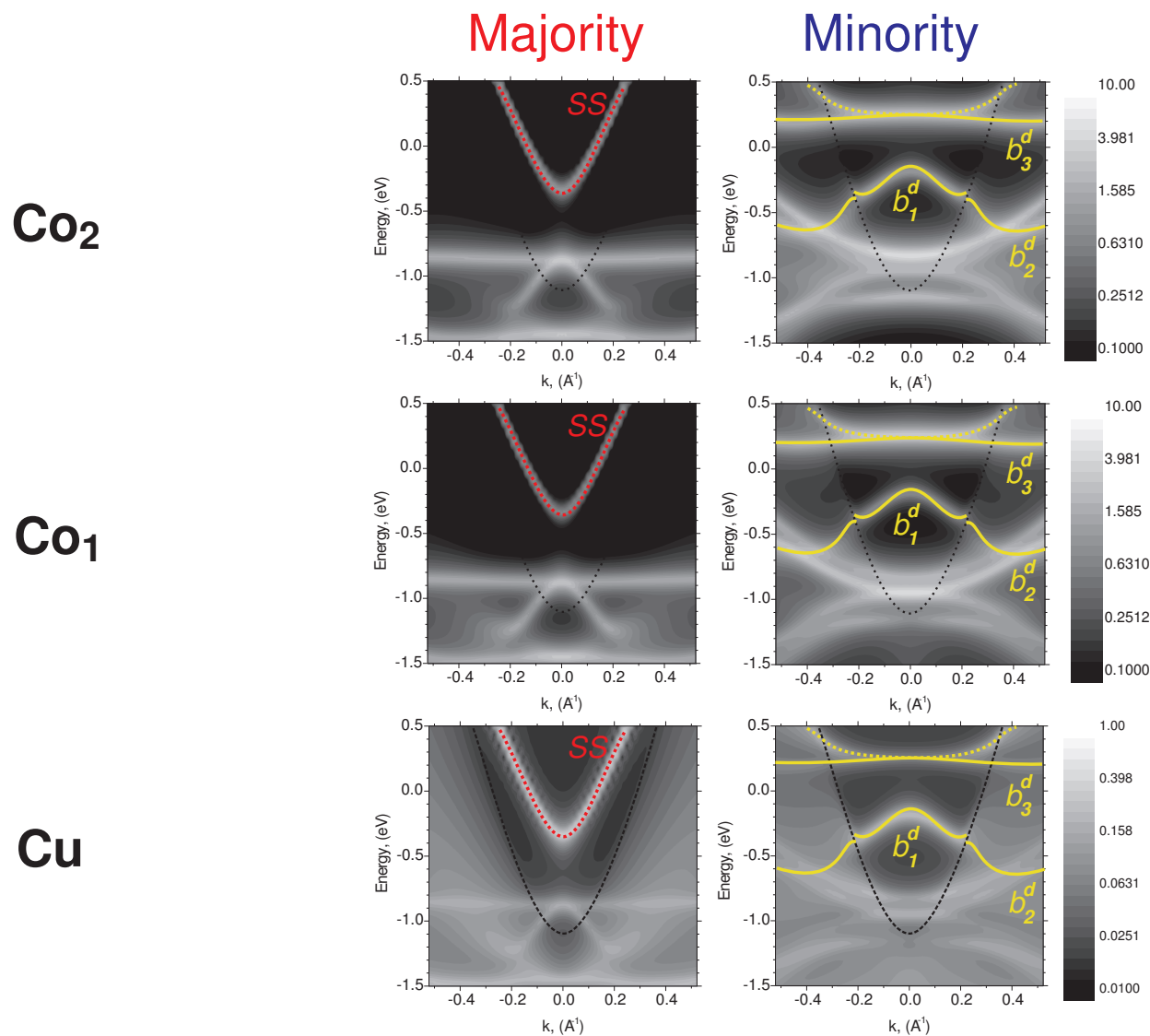
**Figure 5.3:** Spectral density maps of the topmost Cu layer of Cu(111) substrate and two Co overlayers [see Fig. 5.2]. The border of the projected gap of the Cu bulk states is marked with dotted black curve. Solid yellow lines sketch Co $d_{z^2}$ minority bands, from which peaks $p1,p2$ and $p3$ of vacuum LDOS originate. Bands $b_1^d$ and $b_2^d$ can be treated as the same band split at the border of the bulk band gap. The majority band $ss$ represents the majority dispersive Shockley surface state.
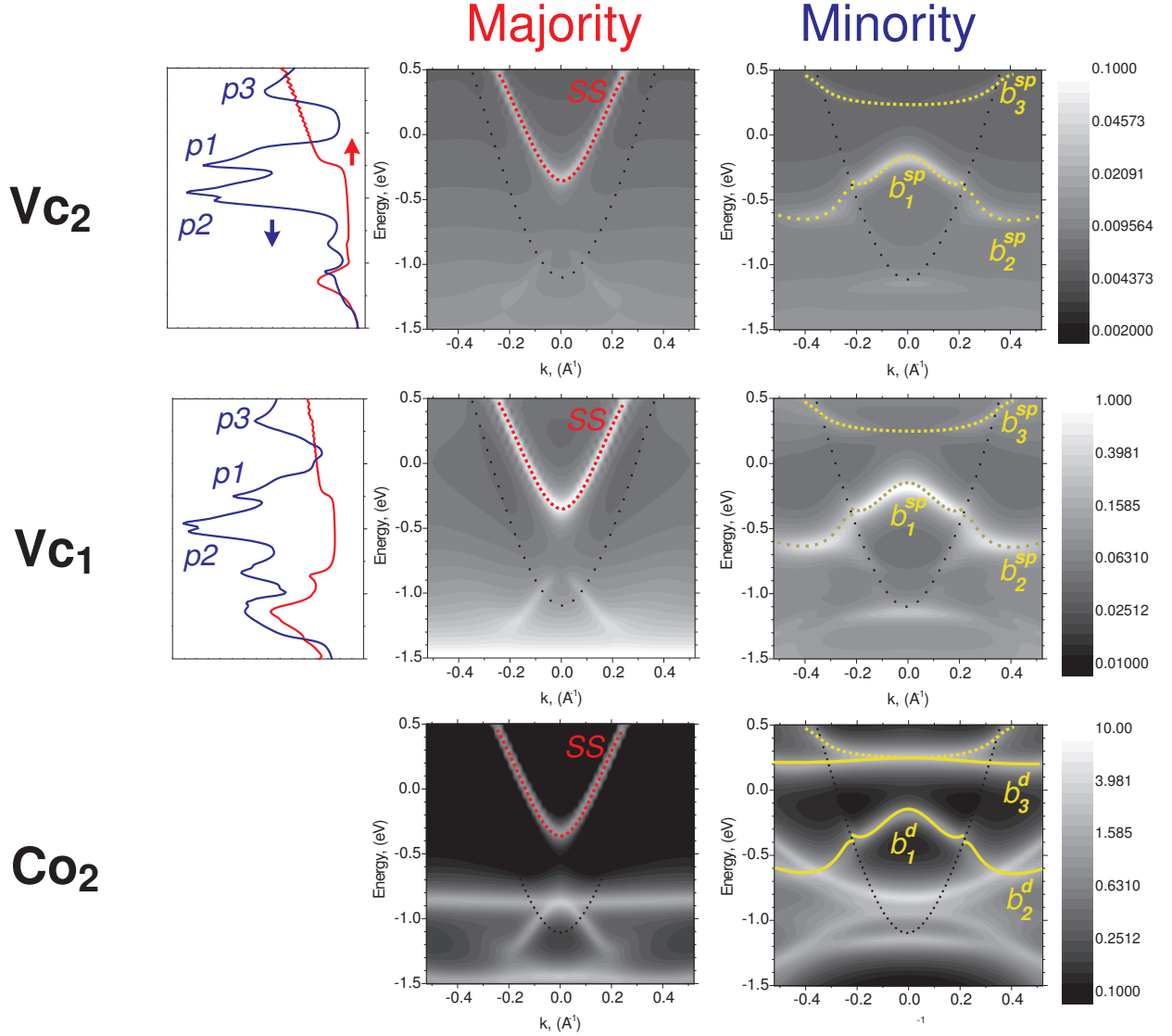
**Figure 5.4:** Spectral density maps of the topmost Co layer and two vacuum layers [see Fig. 5.2]. The boundary of the projected gap of the Cu bulk states is marked with dotted black curve. Solid yellow lines point out Co $d$ minority bands from which peaks $p1$, $p2$ and $p3$ of vacuum LDOS originate. Bands $b_1^d$ and $b_2^d$ can be treated as the same band split at the border of the bulk band gap. Dotted yellow curves demonstrate vacuum bands of $s-p$ character. Band $b_1^{sp}$ is situated in the bulk band gap and therefore can be treated as a surface state. Band $b_2^{sp}$ is a result of resonance scattering of bulk Bloch states at a Co bilayer. Minority dispersive band $b_3^{sp}$ is degenerated in the topmost Co layer with the $b_3^d$-band. The majority band $ss$ represents the majority dispersive Shockley surface state.

Let us first pay attention to the impact of the substrate on the electronic structure of the system. At the Fermi energy Cu(111) surface has the projected bulk band gap around the $\overline{\Gamma}$-point (see our results for clean Cu(111) in Fig. 3.6). Co bilayer does not influence this feature and the gap is clearly visible in SDM of the topmost Cu layer as a dark area surrounded by bulk states. The projected bulk band gap is emphasized in Figures 5.3 and 5.4 by dotted black curves. Several minority dispersive bands crossing the gap region in SDM of the topmost Cu layer come from the electronic structure of the Co bilayer. We are particularly interested in the minority $d$ bands of $d_{z^2}$ symmetry, because $s-p$ states can hybridize with such bands. There are several minority $d$ bands hybridized with $s-p$ states: two occupied $b_1^d$, $b_2^d$ and one unoccupied $b_3^d$. Such bands marked in Figures 5.3 and 5.4 by yellow solid lines. The occupied bands $b_1^d$ and $b_2^d$ can be considered as originally the same $d$ band split at the intersection with Cu(111) bulk states: the upper part $b_1^d$ remains in the gap and the rest $b_2^d$ overlaps with the bulk states. The occupied surface states peak $p1$ at $-0.3$ originates from the $s-p$ states hybridized with the $d$-band $b_1^d$. The resulting vacuum $s-p$ band is marked with a dotted yellow line $b_1^{sp}$ in Fig. 5.4. Note, that this state appears in the Cu projected bulk band gap due to Co bilayer, but not because of termination of the crystal. The minority peak $p2$ comes from the resonance scattering of bulk Bloch states at band $b_2^d$ of Co bilayer. This resonance is pointed out with a yellow dotted curves $b_2^{sp}$ in Fig. 5.4.

The unoccupied vacuum minority LDOS peak $p3$ at $+0.3$ eV is determined by dispersive band $b_3^{sp}$ filled mostly by $s$ and $p$ electrons. It is interesting that the spectral density of states vanishes at the bottom of this band. To clarify the reason one should take a look at the SDM of the topmost Co layer. The $s-p$ dispersive minority band is visible there but at the bottom it degenerates with the nondispersive $d$-band $b_3^d$ of Co. Since $d$-band is spatially localized and bound to the Co bilayer it decays into the vacuum much faster than the $s-p$ states, so electrons do not propagate far away into the vacuum region.

The majority states actually demonstrate some interesting feature, namely, the parabolic band $ss$ of free-like electrons. The majority $d$ states of Co are situated far below the Fermi energy and do not change the electronic structure of surface states significantly, so the Shockley surface state preserves in the majority channel being shifted to the higher energy.

## 5.2.2   Impact of the Co bilayer stacking on the surface states

Let us now turn to the question on the structure of the Co bilayer. At room temperature, evaporated Co adatoms form triangular islands two monolayers in height and oriented in opposite directions on a Cu(111) substrate [88, 127, 128]. According to Negulyaev et al. [88] triangles are formed due to the anisotropic diffusion barriers at island corners. At room temperatures, adatoms jump easily from the A step ( the step with {100} facet) to B step (the step with {111} facet). A reverse motion from B to A is less probable than a further diffusion along the B step [88]. As a result, the length of the B steps decreases till a single atom is left. Such a scenario suggests that the first layer of the Co triangular islands on Cu(111) always forms the B step and therefore, different orientations of the Co islands are a signature of a stacking fault. Here we assume that the second Co layer can grow both on $fcc$ and $hcp$ sites simply filling the area of the first layer.

Differently stacked Co bilayer islands with respect to their orientations are sketched in Fig. 5.5. A stacking order is noted by the letter sequence. The first 3 letters $ABC$ stand for the $fcc$ stacking order of Cu(111) substrate. The last two letters show the stacking order of
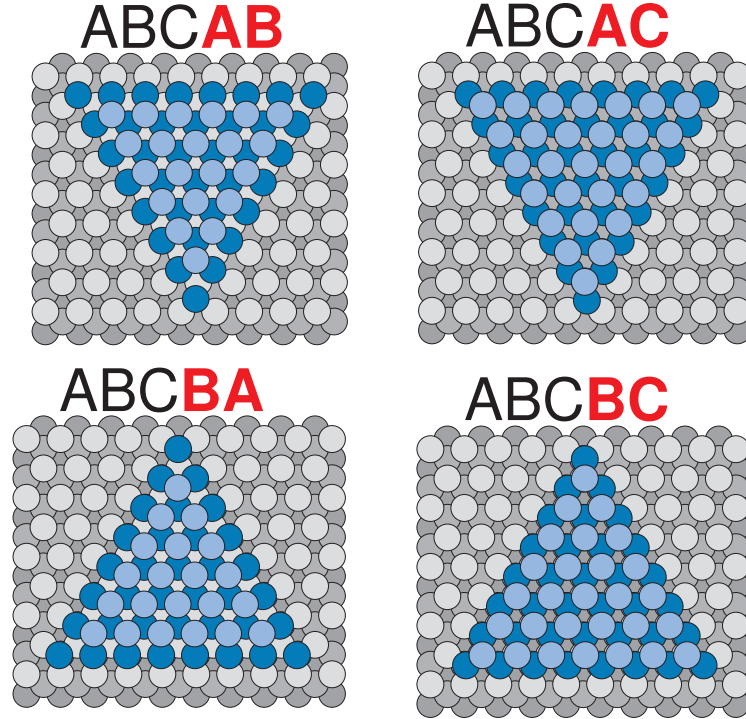
**Figure 5.5:** Sketch of four different stacking orders of Co bilayers on Cu(111) with respect to the island orientation.

the Co layers. As it has been already mentioned, in our calculations we consider large Co island as infinite layers stacked in an appropriate way. The LDOS calculated $\sim 4$ Å above the topmost Co layer is shown in Fig. 5.6 for all possible stacking orders. The main peak $p1$ is clearly visible but its exact position depends on the Co layers stacking: ABCAB and ABCBA stackings yield the peak $p1$ at $-0.25$ eV and ABCBC and ABCAC result in the peak $p1$ at $-0.22$ eV [51] Figures 5.7 and 5.8 give an insight into the constitution of surface states on unfaulted (ABCAB) and faulted (ABCBC) respectively. In both cases LDOS peaks are determined by the minority $s - p$ states hybridized with $d$ states of Co bilayer. The majority LDOS exhibits the onset of free-electron-like surface state ($ss$ in Fig. 5.2) at $\sim -0.2$ eV

For differently stacked Co bilayers Co-Cu hybridization occurs at different energies and therefore the position of the surface-states minority peak also shifts. In principle, the peak position should be different for all the stacking orders, even though in practice we observe only two pronounced positions. This can be rationalized in the following way: one should consider that only the coupling between Co layers and the interface Cu layer is important. There are two general ways to attach a Co bilayer to the Cu(111) surface: (i) the interface Cu and two Co layers form *fcc*-like layer sequences CAB and CBA; (ii) the topmost three layers are stacked *hcp*-like (sequences CBC and CAC).

Our results can be compared with the STM/STS experiments by Pietzsch et al. [49]. They studied the spin-averaged and the spin-polarized electronic structure of nanometer-scale Co islands on Cu(111). According to their results, two island types of different stacking could be clearly recognized by their inequivalent spectra. They emphasize two main features: (i) a strong and sharp occupied peak, and (ii) the second peak about 0.25 eV lower in energy.
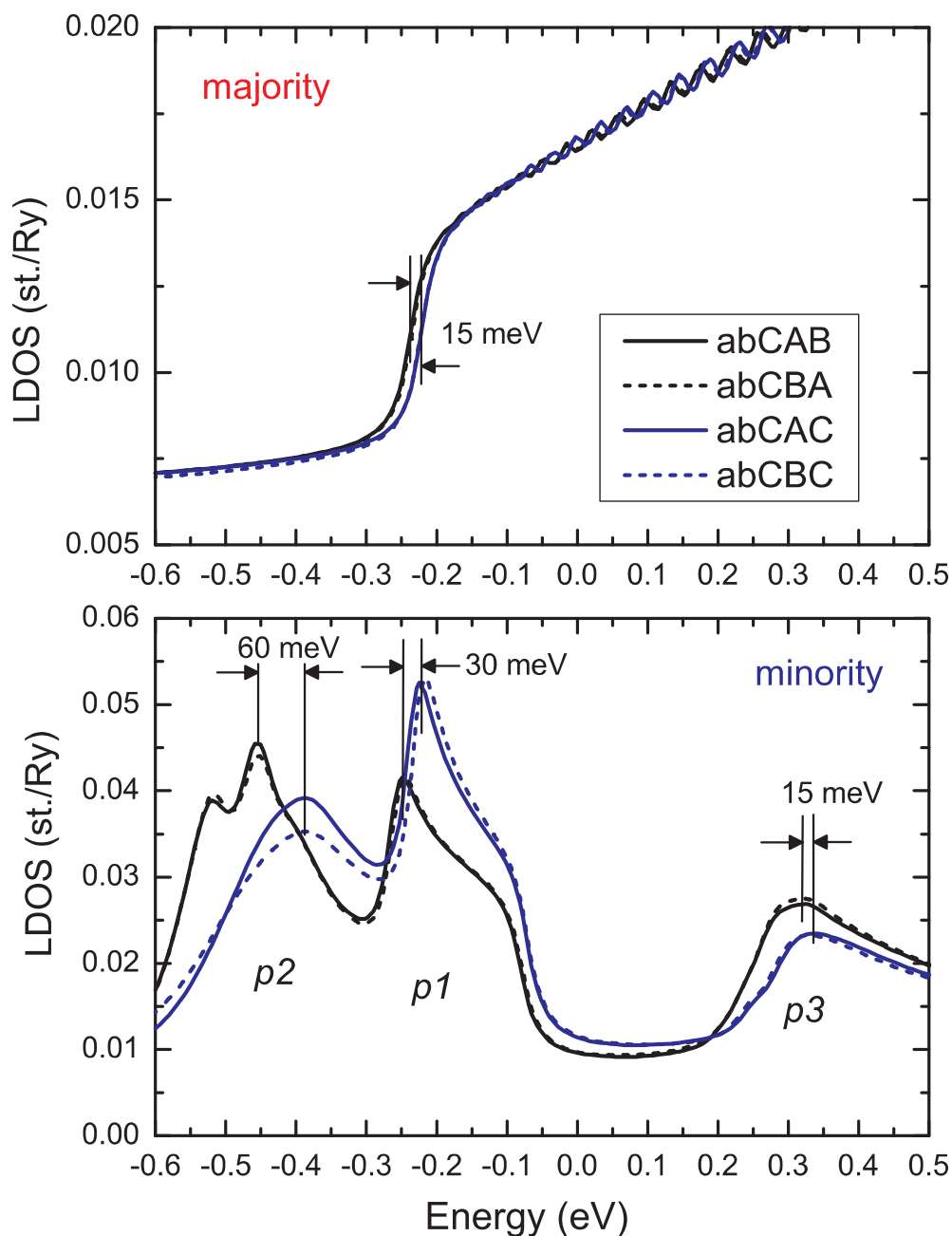
**Figure 5.6:** The minority a) and majority b) LDOS's above differently stacked Co bilayers on Cu(111) substrate. The black curves correspond to the unfaulted stackings, the blue curves to the faulted ones. The minority peaks *p1*,*p2* and *p3* on faulted islands are shifted towards the Fermi energy by 30, 60 and 15 meV respectively. The majority dispersive state band bottom on faulted islands is also shifted by 15 meV towards the higher energies.
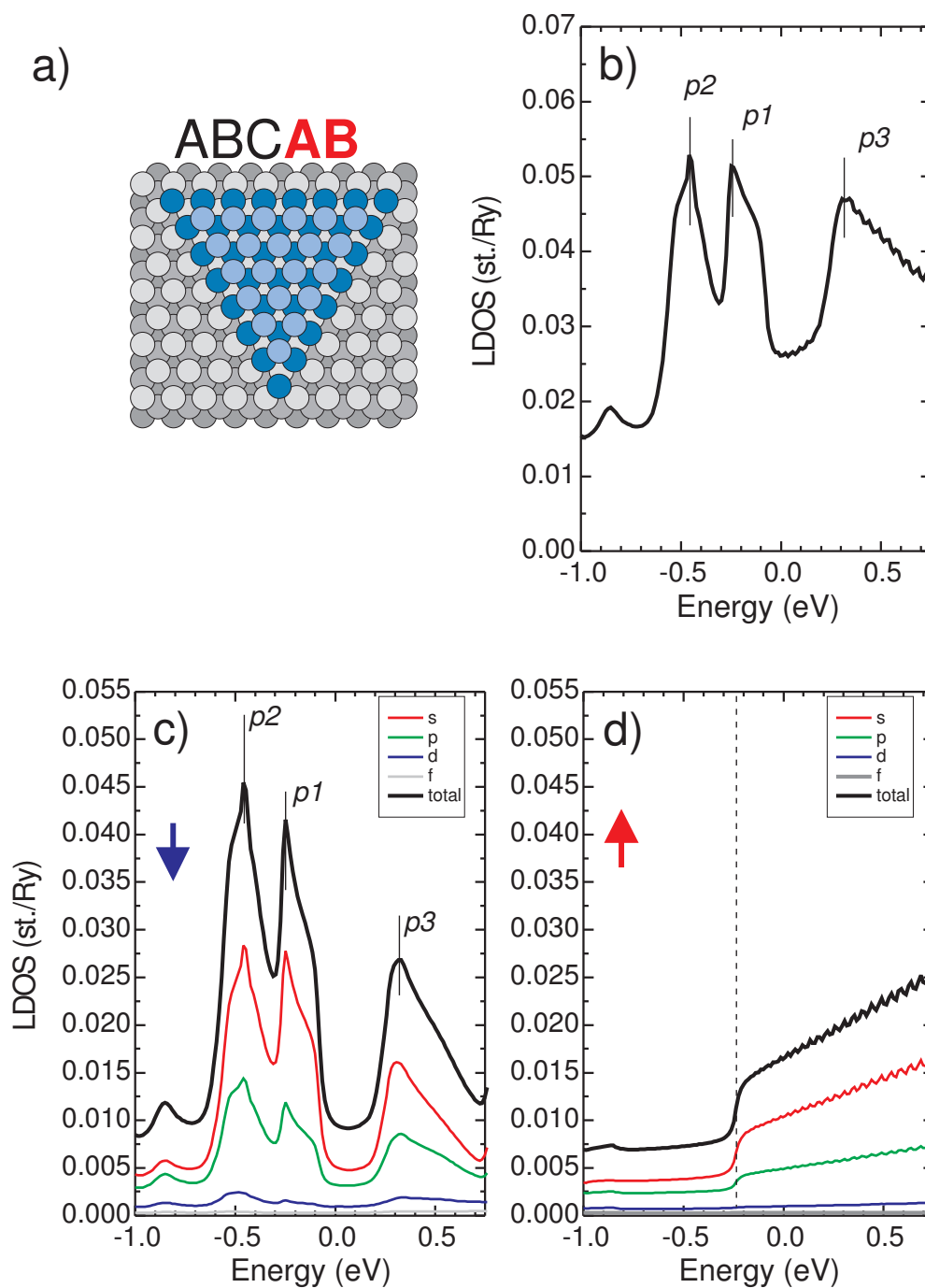
**Figure 5.7:** a) Atomistic sketch of the unfaulted triangular Co nanoisland on Cu(111) surface. b) The total LDOS 4 Å above the unfaulted Co bilayer. Three LDOS peaks originating in the minority $d$-bands are clearly visible.  c) Partial minority LDOS. All the minority peaks at 4 Å consist mainly of $s$ and $p$ electrons with small $d$ contribution d) Partial majority LDOS. The onset at $-0.24$ eV corresponds to the nearly free-electron-like surface state band.
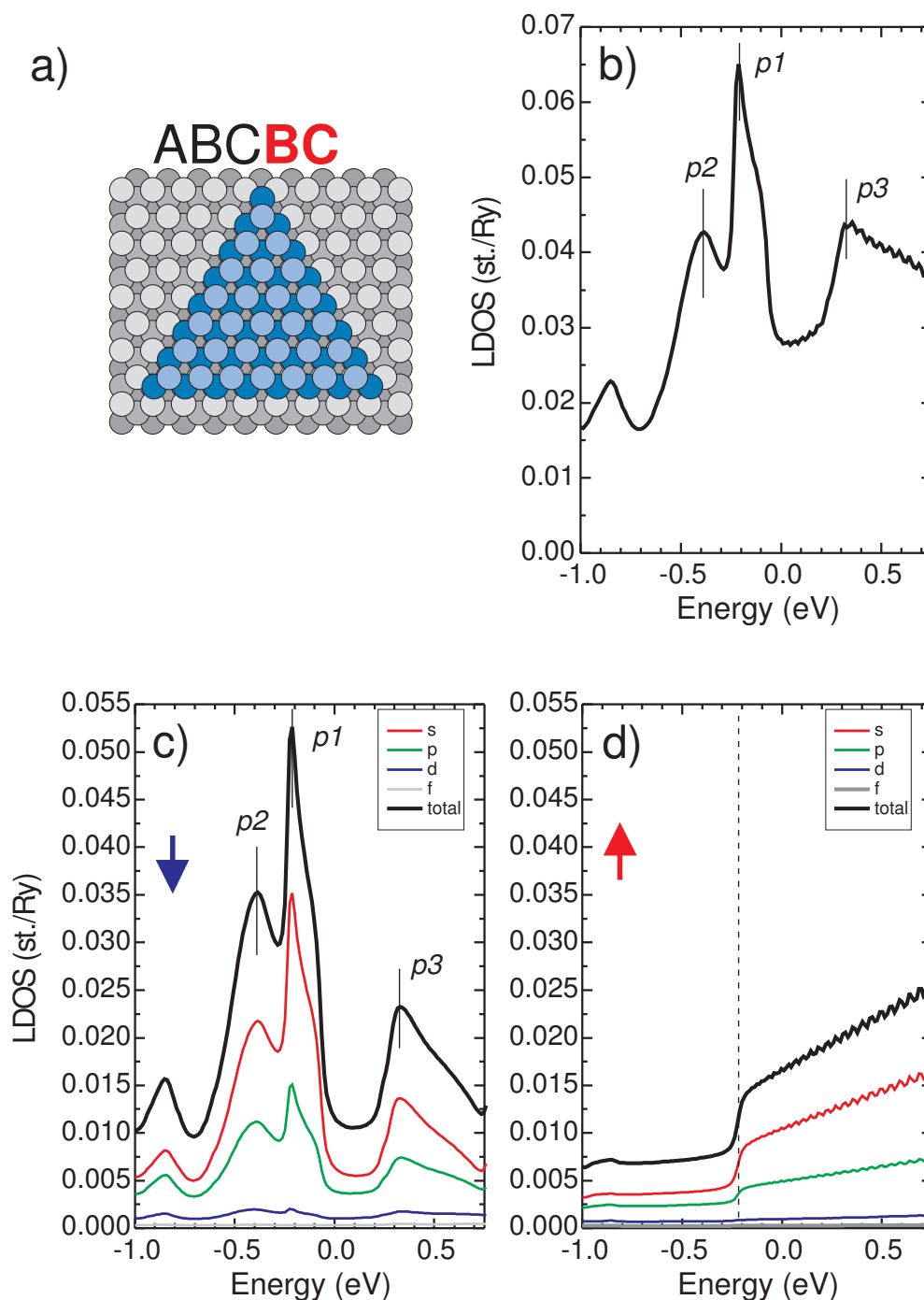
**Figure 5.8:** Atomistic sketch of the faulted triangular Co nanoisland on Cu(111) surface. b) The total LDOS 4 Å above the faulted Co bilayer. Three LDOS peaks originating in the minority $d$-bands are clearly visible. c) Partial minority LDOS. All the minority peaks at 4 Å consist mainly of $s$ and $p$ electrons with small $d$ contribution d) Partial majority LDOS. The onset at $-0.22$ eV corresponds to the nearly free-electron-like surface state band.

Exact positions of this features depend on the stacking of the island. On *fcc* islands, the peak (i) is centered at $-0.35$ eV while it is found at $-0.28$ eV on faulted islands. The theory yields slightly higher energies of these peaks ($-0.25$ eV and $-0.22$ eV, respectively) and smaller shift.

## 5.3 Spin-polarized surface states on 2ML Co on Au(111)

Bilayer Co nanoislands can also grow on the Au(111) substrate. The herringbone reconstructed surface of Au(111) [129, 130] is ideal for self-organization of two-dimensional arrays of Co-clusters [131]. Due to the particular topology of reconstructed Au(111) surface, Co clusters grow on it at preferential nucleation sites pertaining to *fcc* and *hcp* zig-zag domains of the topmost atomic layer. On these domains, Co was found to grow in stable atomic bilayer clusters [131, 132, 133]. The STM topology of Co nanoislands on reconstructed Au(111) surface is presented in Fig. 5.9(a) for two rows of Co-clusters, self-organized on *fcc* sites and *hcp* sites respectively. If a lateral size of a cluster exceeds 3 nm it may also cover parts of the discommensuration lines. Unlikely to Co nanoislands on Cu(111), the "nearly" triangular clusters pointing at two opposite directions are observed on Au(111) [54]. As an example, Fig. 5.9(a) shows an STM image, where such clusters were labelled 1 and 2. STS measurements performed on these clusters are shown in Fig. 5.9(b). The spectrum acquired on cluster 1 shows a pronounced peak at $-0.15$ eV, whereas in cluster 2 this peak appears at $-0.085$ eV. The shift of this main peak can be the signature of different stacking orders, similar to that found on Co/Cu(111) [49].
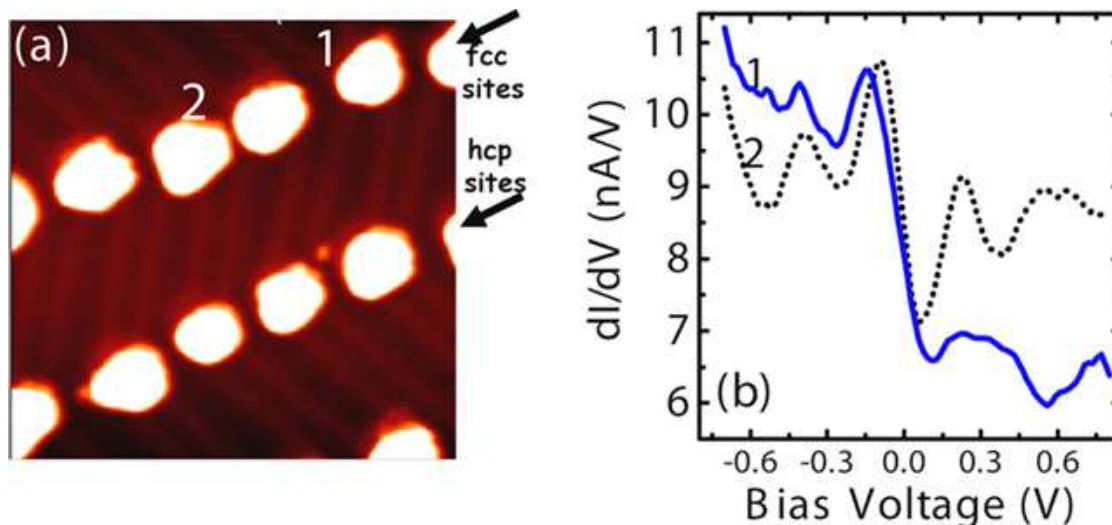


**Figure 5.9:** a) Constant current ($320 \times 320$ Å$^2$) STM image of self-organized bilayer Co clusters on the herringbone reconstruction of Au(111). b) STS spectra measured on clusters noted 1 and 2. Each spectrum is an average of 4 single point spectra. Set-point parameters before feedback opening were 530 pA and 0.095 V. The figure is published in [54].

Four possible stacking orders are possible for a bilayer cluster on *fcc* surface as shown in Fig. 5.10(a)). The STM image of Fig. 5.9(a) alone does not allow identifying a priori which stacking order corresponds to clusters 1 and 2. However, the clusters are limited by either {111} or {100} steps. Due to the higher stability of the {111} steps with respect to {100}
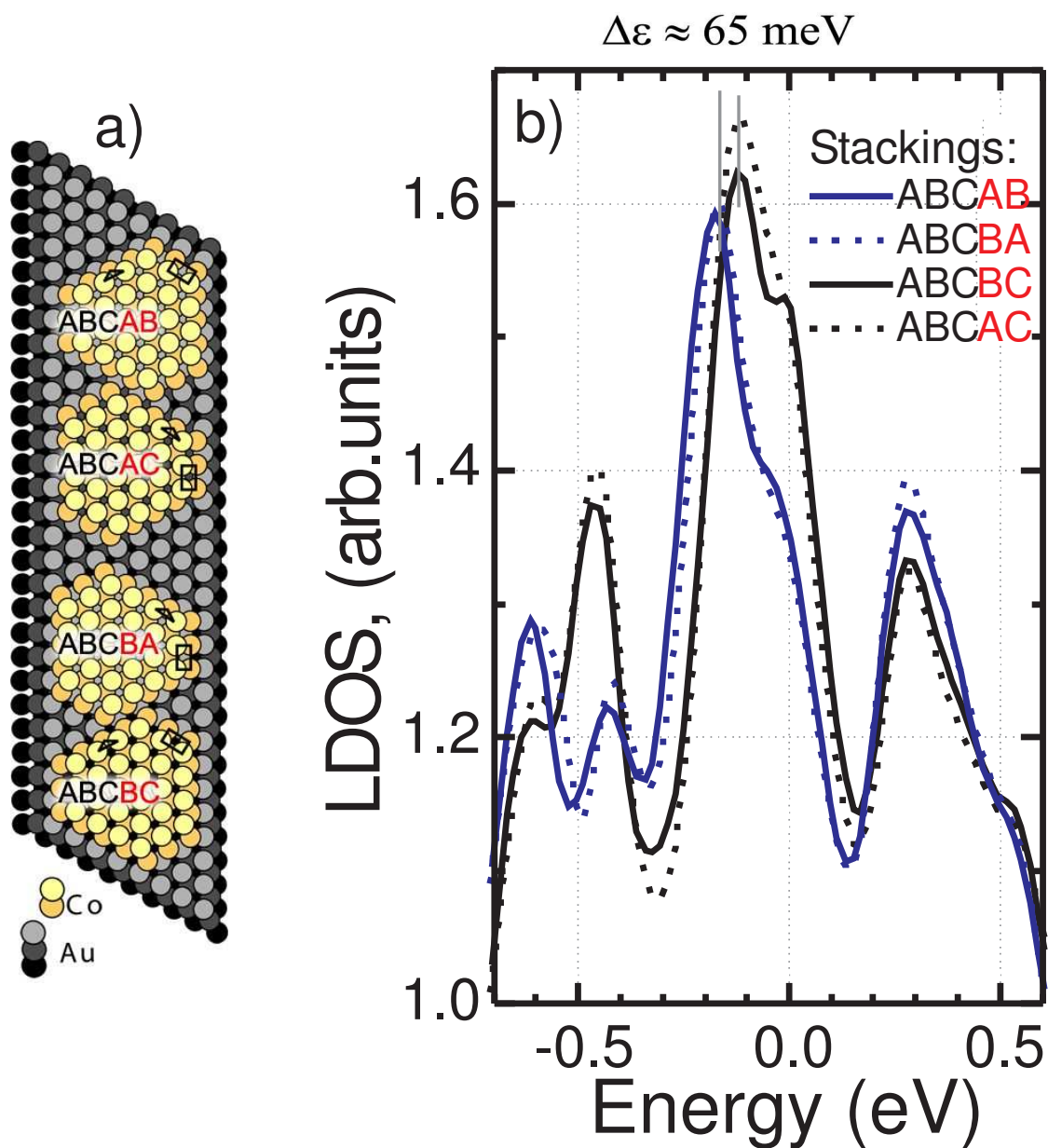
**Figure 5.10:** a) Four possible stacking orders for 2L Co islands on *fcc* Au(111) with opposite islands orientation. The small black triangles show the (111) facets, while the black rectangles the (100) ones. b),c) Calculated LDOS, 2.35 Å above the Co bilayer on the *fcc* Au(111) surface. The LDOS's have been paired to satisfy both, orientations and the main LDOS peak shift.

ones [131], the clusters are expected to adopt the particular shapes shown in Fig. 5.10(a). The small Co bilayer clusters on Au(111) are allowed to rearrange permanently during growth as evidenced by the transition from monolayer to bilayer occurring at about 20 atoms [133] . This behavior is mainly due to the strong affinity of Co for Co and to the large lattice mismatch of about 13% between Co and Au [54]. The shape of Co islands on Au(111) is therefore defined primarily by the minimization of its edge energy, contrary to Co islands on Cu(111) which shape is determined by kinetical processes [88].

In order to discuss the energy shift of the main peak, four possible cluster pairs with opposite orientations were considered. Electronic structures of the various configurations have been calculated by the SKKR Green's function method. All stacking orders sketched in Fig. 5.10(a) have been considered in the calculation. The calculated local densities of states (LDOS) above the two cobalt layers on fcc-Au(111) are shown in Fig. 5.10(b). The calculations show that the pronounced peaks, below and above the Fermi energy, have minority state character. Similarly to the case of Co bilayer on Cu(111) faulted and unfaulted bilayers can be distinguished by the shift of the main LDOS peak. The main peak shift appears if three topmost layers are stacked in a *hcp* manner [ABCAC and ABCBC in Fig. 5.10(b)] and does not appear if these layers are stacked *fcc*-like [ABCAB and ABCBA in Fig. 5.10(b)].

## 5.4 Comparing surface states on Co bilayers on various substrates

The pronounced peak in the density of surface states on Co clusters on Au(111) is of the same origin like the one found in Co/Cu(111) [48, 49] but is situated at energy much closer to the Fermi level than in the case of Co/Cu(111). Peak $p1$ originates from the $d$-band of Co bilayer, therefore variations in its position should be related to the interaction between Co atoms of the bilayer. Such an interaction should depend on the Co-Co interatomic separations, which are determined by substrate lattice constant. Table 5.1 presents positions of the peak measured for different substrates. The smaller is the lattice constant, the deeper in energy peak $p1$ lies.

**Table 5.1:** Energy of the minority surface state peak on bilayered Co islands on different substrates. The larger is the substrate lattice constant, the higher is the energy of the peak.

|                    | Au(111) | Pt(111)    | Cu(111) |
|--------------------|---------|------------|---------|
| Mismatch (%)       | 13      | 9          | 2       |
| Peak position (eV) | -0.13   | -0.23[53]  | -0.31   |

In order to get a better insight into the role of substrate, we have performed ab initio calculations for Co bilayers on a Au(111) substrate compressed to the Cu lattice on the one hand and on Cu(111) substrate expanded to the Au lattice on the other hand. As shown in Fig. 5.11, in both cases a significant shift of surface states is revealed in the calculated LDOS. A compressed Au(111) substrate results in a peak shifted by 0.35 eV to the lower energies [Fig. 5.11(a)] while an expanded Cu substrate shifts the Co peak by approximately 0.25 eV to the higher energies [Fig. 5.11(b)].
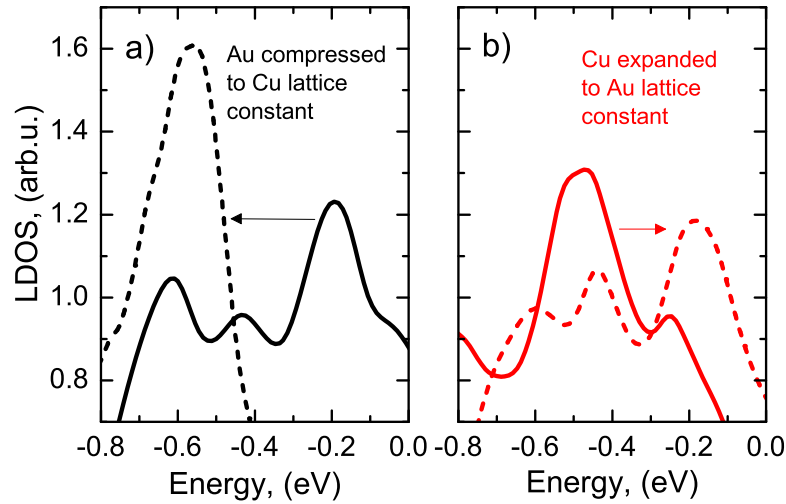
**Figure 5.11:** Minority component of the LDOS calculated 2.35 Å above the Co bilayers on normal (solid line) and strained (dashed line) *fcc* Au(111) (a) and *fcc* Cu(111) (b) substrates. A large shift of the main occupied peak towards the Fermi level occurs for substrates with large lattice constants. The figure is published in [54].

To prove that the shifted and un-shifted peak arises from a change in energetic position of the same state we plot spectral density maps of spin-polarized surface states above Co bilayers on normal and compressed *fcc* Au(111) along $\overline{\Gamma} - \overline{M}$ direction [Fig. 5.12]. For both substrates the peak below the Fermi energy is determined by hybridization of *s-p* states with the *d* states of Co bilayer [Fig. 5.12(a,c)] similar to the Co/Cu(111) system. The main contribution to the LDOS calculated 2.35 Å above the surface is given by a region away from the $\overline{\Gamma}$-point, near 0.3 Å$^{-1}$. Therefore, a compression of the substrate leads to the shift of this state to lower energies but the contributing region seems to remain nearly the same. As a result, the lateral compression or expansion of the Co layers is found to be the driving force for the shifting of the minority peak below the Fermi level. Vertical relaxations practically do not affect the character of surface states.

Analysis of spin-polarized surface states on Co bilayers on Cu(111) and Au(111) has clearly demonstrated that a careful choice of the structure and the substrate for Co nanostructures may lead to a variety of conditions influencing the energy of surface states electron. In particular, a pronounced occupied states peak with minority character, has been found on bilayer Co islands on Au(111) much closer to the Fermi energy than in the case of Co/ Cu(111) . The further possibility to tune the energy of the minority peak is to adjust a stacking of Co bilayer. It has been revealed that faulted Co bilayers exhibit this state at slightly higher energies. This finding opens the possibility to increase low bias spin transmission in magnetic tunnel devices based on Co nanostructures and can be interesting for practical applications.
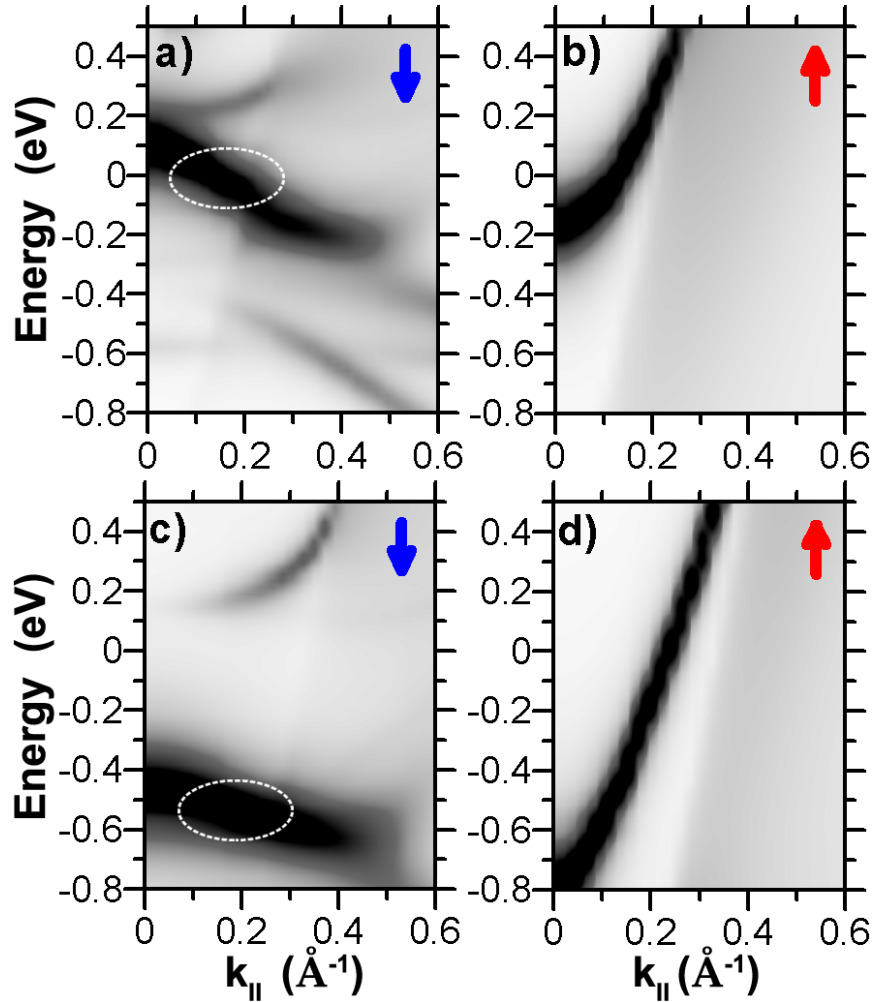
**Figure 5.12:** Spectral density maps of spin-polarized surface states calculated 2.35 Å above Co bilayers on normal (a),(b) and compressed (c),(d) *fcc* Au(111) along the $\overline{\Gamma} - \overline{K}$ direction. The minority peak below the Fermi energy is determined by strongly hybridized s-p-d states. The region away from the $\overline{\Gamma}$-point where these states are located is marked in (a) and (c) by the dashed white ovals. It is found that the compression results in the shift of the peak to the lower energies while the contributing region remains nearly the same. Majority states have parabolic dispersion relations (b),(d). The figure is published in [54].

# Chapter 6

# Size-dependent surface states on Co islands on Cu(111)

Recent STS experiments have established that the occupied surface states exhibit a size-dependent energy shift [134]. A shift has been also observed at the corners and edges of islands with respect to their centers. In this chapter we demonstrate the interplay between strain-induced structural relaxations and surface states of Co nanoislands on Cu(111). Our atomic-scale simulations and *ab initio* calculations reveal [134] that the energy positions of the occupied surface states are determined by mesoscopic relaxations in the nanoislands [87]. Our work suggests that surface states can be a sensitive probe for variations of the atomic structure at the nanoscale.

## 6.1 Concept of mesoscopic relaxation

In the previous chapter we demonstrated that the position of the localized minority peak *p1* [see Fig. 5.4] of surface states on bilayer Co films are very sensitive to the in-plane Co-Co separations. Co atoms in bilayer film are situated exactly in the high-symmetry adsorption sites so the in-plane Co-Co bond length is determined by the substrate lattice constant. In the same time, it was theoretically predicted that bond length in small Co nanoislands on Cu(111) substrate depend on the size of the island and can significantly alter from that in a bilayer film [85].

Lengths of interatomic bonds in solid crystals are determined by the atomic species and the structure of the material considered. Equilibrium lattice parameters usually are determined by the minimization of the total energy of a crystal with respect to its structure. A presence of a surface results in the redistribution of the electronic density near the crystal-vacuum interface and, hence, a surface-related strain appears. To relieve the strain, a number of surface layers shift from their ideal bulk positions. The magnitude and direction of displacements is individual for every particular material. For instance, a Cu(111) surface relaxes inwards and the topmost layer shifts by $\sim 2\%$ of ideal interatomic distance [135]. Pt(111) surface on the contrary exhibits small ($< 1\%$) outwards relaxations [135]. The situation can be even more complicated because of strain induced surface reconstruction. A classical example of such a system is herring-bone reconstruction of Au(111) surface [130].

Suppose now that we have a nanostructure of finite size epitaxially grown on some unreconstructed substrate. Similarly to the case of surface-induced relaxations one can expect significant atomic displacements caused by the bonds broken at the borders of nanostruc-
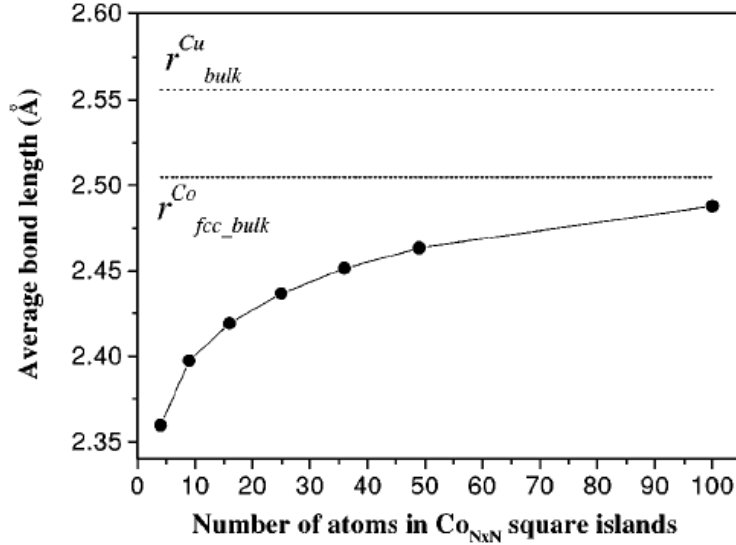
**Figure 6.1:** The average Co-Co bond length in two-dimensional compact Co islands on Cu(001) . The figure is taken from [85]

ture. Strain-induced shape transitions in islands were predicted by Tersoff and Tromp [136]. At a glance, atomic displacements in the case of epitaxial growth can be expected to depend on the macroscopic mismatch $m$ between bulk lattice constants $r_0$ and $r_b$ of the substrate and nanostructure species:

$$M = \frac{r_b - r_0}{r_0} \qquad (6.1)$$

If $M$ is negative, then interatomic bonds in nanostructure should be smaller than those of the substrate because nanoislands tend to adopt their native lattice constant. If $M$ is positive then interatomic bonds in the nanostructure are expected to be larger than those of the substrate.

However, detailed investigations of the problem showed that the mesoscopic lattice mismatch should depend on the size of nanostructures. Relaxations of atoms in islands can lead to in-plane lattice spacing variations, which cannot be predicted using macroscopic mismatch arguments [87, 86, 85]. In small islands of the mesoscopic scale the average bond length $< r_{Cluster} >$ can be significantly smaller than $r_b$ and a new characteristic, mesoscopic mismatch, should be introduced:

$$m = \frac{< r_{Cluster} > - r_0}{r_0}. \qquad (6.2)$$

To illustrate the effect of mesoscopic mismatch we review the case of 2D compact square Co islands on Cu(001) surface from the work by Stepanyuk et al. [85]. The macroscopic mismatch $m_{Cu/Co}$between Cu and Co is $\sim 2\%$. Quantitatively atomic relaxation can be characterized by the average bond length in islands. Results of atomic scale simulation are presented in Fig. 6.1. One can see that average bonds in the islands are shorter than the bond length in *fcc* Co and Cu bulk due to the strong relaxation of edge atoms. These relaxations are smaller than in the free-standing Co clusters, because bonding of Co atoms to the Cu substrate prevents shrinking. This would suggest a small tensile strain in Co nanostructures on Cu(001). With increasing size of the cluster, the effect of edge atoms becomes less

important and the average bond length increases. In small islands the relaxation of edge atoms governs the bond length. Since the perimeter of square islands scales as $\sqrt{N}$ ($N$ is the total number of atoms in the island) the estimated scaling law for the mesoscopic misfit $m$ should scale like $[\sqrt{N}]^{-1}$ [86]. Still in a Co island containing 100 atoms the average bond length is smaller than that in *fcc* Co bulk. Recent surface X-Ray diffraction (SXRD) experiments have provided a direct confirmation of the theory of mesoscopic relaxations [91].

## 6.2 Experimental motivation

The theory of mesoscopic relaxation predicts that bond lengths in nanostructures depend on the size of nanostructure. The surface state on Co bilayer can be utilized as a probe of the Co-Co in-plane bond length. Recent STM/STS experiments performed by the group of Prof. J.-P. Bucher [134] have demonstrated the validity of such an approach. Figure 6.2(a) demonstrates a set of spectra acquired on Co nanoislands of different size. Three peaks $p1$, $p2$ and $p3$ are clearly visible. Peaks $p1$ and $p2$ shift downward in energy when the island size decreases from 22.5 nm to 4.8 nm, with no appreciable changes in the shape and in the amplitude of the line. On the contrary, the position of $p3$ is unchanged. Figure 6.2(b) presents a quantitative evaluation of the size-dependent shift of peak $p1$. Presented data figure out a monotonical peak shift over 0.09 V for unfaulted islands. The faulted ones show a steeper increase of the shift with an asymptotic behavior appearing above an island larger than 13 nm. Figure 6.2(b) is the result of a systematic study of STS data acquired in the center of 230 islands of increasing island size – from 4.8 to 31.9 nm on unfaulted islands, and from 6.7 to 32.9 nm on faulted ones.

In order to explore a possible involvement of edge effects, especially in the smallest islands studied, spectra were acquired over the surface of faulted and unfaulted islands. Figure 6.3(a) shows the typical spatial dependency of peak $p1$ when moving from a corner of an island (here a faulted one), through the center, to the opposite edge. The peak positions extracted from all the spectra acquired along with the line profile of the island are presented in Figs. 6.3(b,c) respectively. In the center of the island [spectra 5, 6, 7] peak $p1$ is shifted approximately to $-0.36$ V because of the small island size (7.1 nm). However, within $\approx 1.0$ nm from the edge peak $p1$ starts to move further downward in energy [spectrum 8 on Fig. 6.3(a)], reaching a displacement of $-0.03$ V [spectrum 9] relative to the center position. A diminished amplitude of $p1$ is also observed, in agreement with [51]. Similarly, at $\approx 2.5$ nm from the corner, an additional displacement of $-0.05$ V progressively sets in [spectra 2, 3, 4], the amplitude of the peak also decreases until disappearance at the corner [spectrum 1]. This additional shift only occurs close to the edges and corners, and it has a negligible influence on the shift in the center of the island, even in the smallest islands investigated. In our previous work it was concluded that Co-Co bond lengths had to vary with the lattice constant of a given substrate, affecting thereby the energy positions of the occupied peaks [54]. This strongly hints to a size-dependent in-plane Co-Co bond variation for Co nanoislands on Cu(111), i.e. to a mesoscopic relaxation, as we establish below.
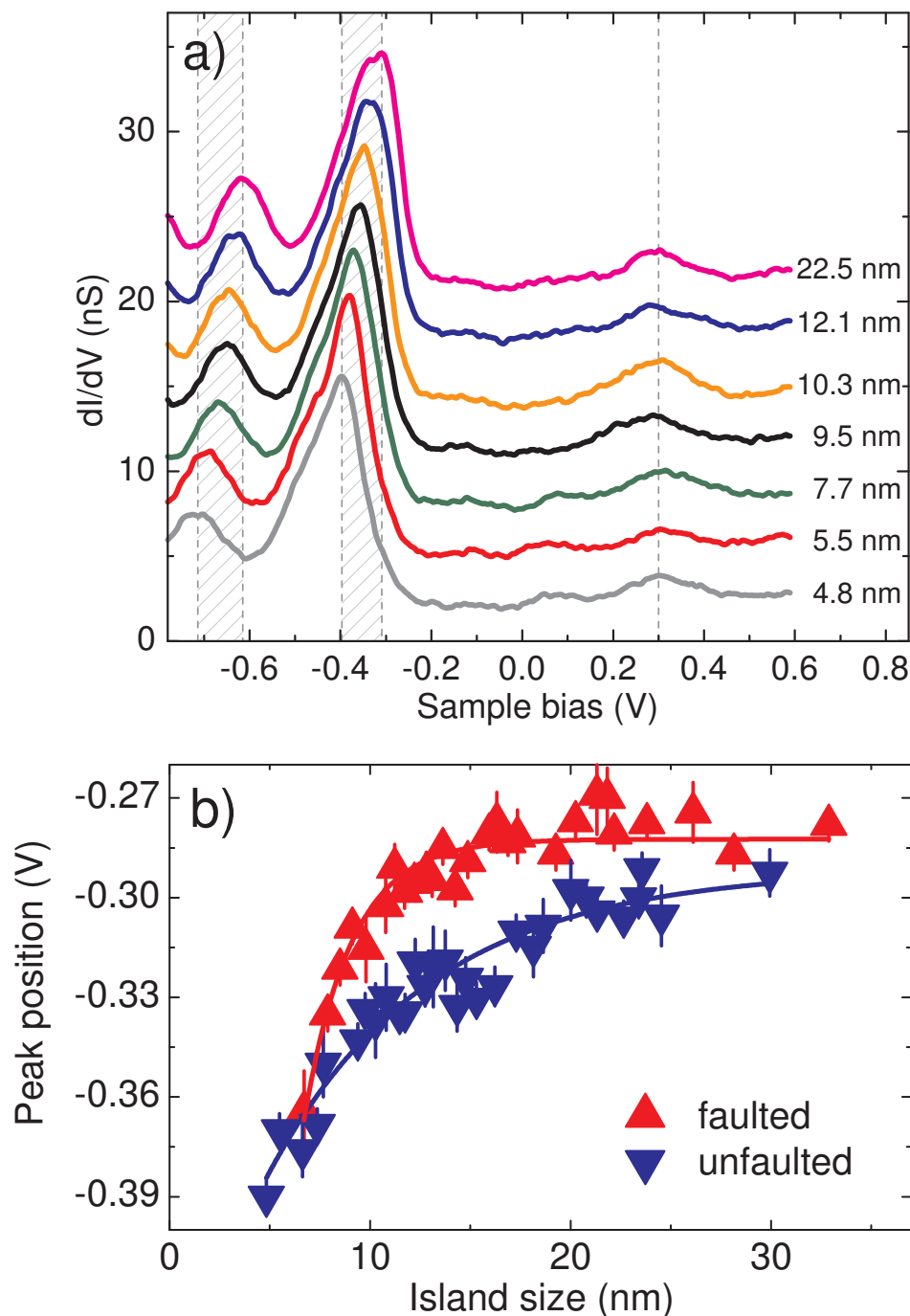
**Figure 6.2:** a) $dI/dV$ spectra on unfaulted nanoislands of increasing size. Feedback loop opened at 1.5 nA, 0.6 V. Spectra over islands sizes of 5.5, 7.7, 9.5, 10.3, 12.1, 22.5 nm are vertically shifted upward by 3, 6, 9.2, 12, 16, 19 nS, respectively. The hatched areas delimit the range over which an energy shift is observed for peak $p1$ and $p2$ in these spectra. The dashed line is positioned at peak $p3$. b) Peak $p1$ position versus island size (up triangles: faulted, down triangles: unfaulted). Solid lines are a guide to the eye. Data is binned by steps of 0.5 nm. Measurements were performed by the group of Prof. J.-P. Bucher. The figure is published in [134].

## 6.3   Theoretical results

A set of calculations were conducted firstly to find the fully relaxed atomic configurations and secondly to estimate the corresponding energy shift of surface states on Co bilayer. The
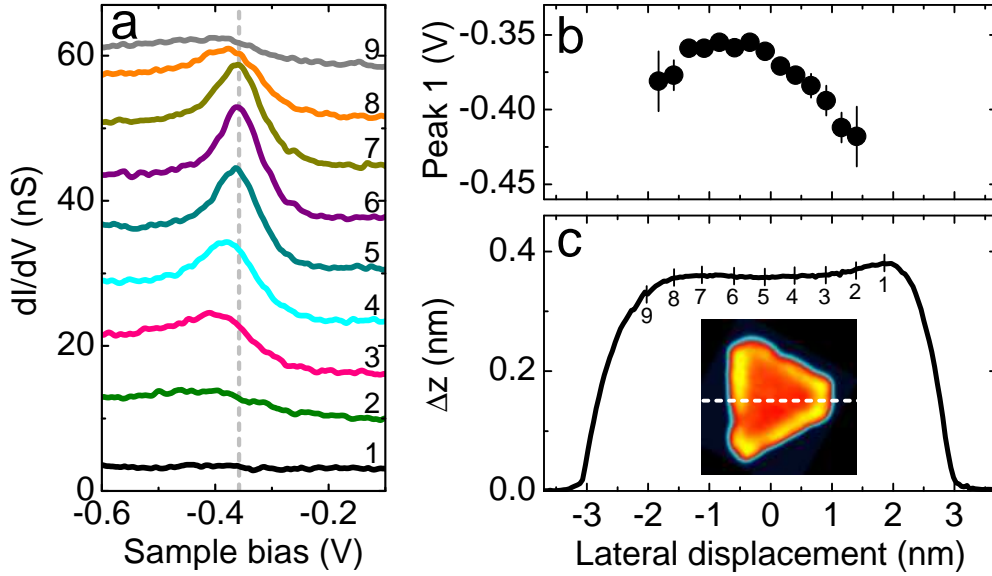
**Figure 6.3:** a) $dI/dV$ spectra acquired across a faulted 7 nm nanoisland. Feedback loop opened at 1 nA, 0.5 V. Spectra 2–9 are shifted vertically by steps of 7 nS. The dashed line is centered at the peak positions of spectra acquired in the island center of gravity (spectra 5–7). b) Energy shift of peak $p1$, and c) Line profile across the island (from corner to edge as depicted by the dashed line on the image). Numbers from 1 to 9 are the corresponding positions where the spectra noted 1 to 9 on panel a) were acquired. Measurements were performed by the group of Prof. J.-P. Bucher. The figure is published in [134].

relaxed atomic configurations have been obtained by molecular dynamics method described in Section 3.4. Perfectly triangular unfaulted bilayer Co islands with sizes ranging from 4 nm up to 30 nm were studied. The analysis has confirmed that both in-plane bond length and interlayer distance depend on the island size and vary across the island. The distribution of the topmost Co layer in-plane bond length over a 15 nm island is presented as an example in Fig. 6.4(a). The distribution is inhomogeneous over the island. The Co atoms at the edges/corners are relaxing in the direction of the center of the island and take other equilibrium positions with shorter bonds with respect to Co atoms in the center. The inner region around the gravity center of the island presents a nearly homogeneous distribution of the bond lengths [inset of Fig. 6.4(a)], and thus an average in-plane bond length $r$ and interlayer distance $z$ can be used to describe the structure of this region. Both $r$ [Fig. 6.5(b)] and $z$ depend on the island size. With an increasing island size $r$ increases towards the ideal bond length of bulk Cu ($r_0 = 0.2556$ nm). The mismatch $(r_0 - r)/r_0$ varies from 0.1% and approaches in the smallest islands the macroscopic mismatch of 2%. Concomitantly, the interlayer distance decreases by about 1% with increasing island size.

To calculate the surface states LDOS above the Co islands the full potential (FP) approximation of the SKKR Green's function method has been applied. To estimate the surface states above the center of each island we have performed the calculations for the infinite Co bilayers. The correct average in-plane Co-Co bond length $r$ in the central region of an island obtained from the MD simulations was introduced through the adjustment of the substrate lattice constant. We found that such a shrinking of the substrate did not
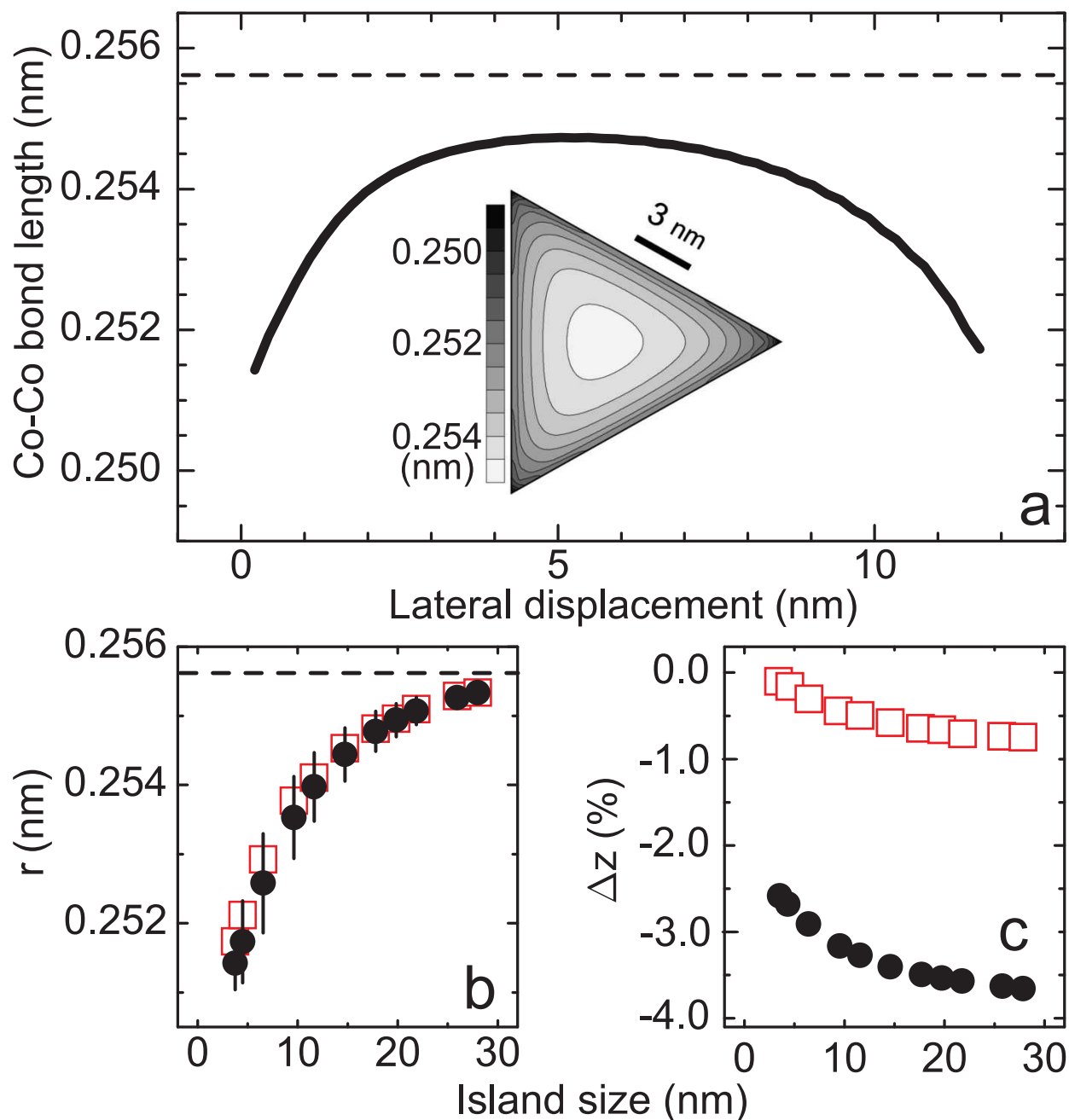
**Figure 6.4:** a) Variation of the in-plane bond length of the top Co layer across the island with the edge length equal to 14 nm (dashed line: ideal bulk Cu bond). Inset: Spatial distribution of in-plane Co-Co bonds. b) Average-bond length $r$, described in the text, for the top (solid circles) and bottom (open squares) Co layers. c) Change of the average distance between Co layers (solid circles) and the bottom Co layer and substrate (open squares) in percentage of the ideal Cu-Cu interlayer distance as a function of island size. The figure is published in [134].

affect the projected gap of the Cu bulk states, so shift of the peak positions really originate from the changes of the Co $d$-bands. Vacuum LDOSes plotted for several values of in-plane Co-Co bond lengths are shown in Fig. 6.5(a). The behavior of the peaks is the same as that observed experimentally. The positions of peaks $p1$ and $p2$ depend on island size. The calculated shift of peak $p1$ versus the island size is presented in Fig. 6.5(b) and is seen to vary over 0.07 eV, in a good agreement with the experimental results. Peak $p2$ yields a similar variation, also in agreement with the experimental results. In the previous chapter we demonstrated that peaks $p1$ and $p2$ originate from the same occupied $d$-band of the Co bilayer. The simultaneous shift of both peaks indicates that strain effects cause an energy shift of this $d$ band. The variation of the in-plane bond length is the driving force for the shift observed.

The agreement between the experimental results and the theoretical results is evident, however there is an underestimation of the theoretical shift for the small islands. The approximation of the relaxed Co islands with infinite Co bilayers does not take into account the impact of strongly relaxed island edges on the surface states. Such an impact is comprised of two contributions. The first is the purely structural effect caused by strongly inhomogeneous bond length distribution near the island edges [see Fig. 6.4(a)]. Bonds lengths variations within a few percent of the ideal value alter the surface states but do not affect their band structure. This effect plays a large role in small islands but counts a little in large ones. The second contribution can arise from the fact that the electronic structure of Co atoms at island edges differs significantly from that of the atoms in the center of the islands [51]. This contribution is not taken into account in the present theoretical approximation. We performed calculations to estimate the impact of the structural relaxations at the edges/corners of the island on the surface states. Despite the lower accuracy expected due to the spatial averaging applied, a shifts of $-0.03$ eV and $-0.06$ eV estimated for peak $p1$ at the edges and corners, respectively, are agreement with the experimental values of Fig. 6.3(b).

The downward shift of peaks $p1$ and $p2$ for decreasing island size can be rationalized in the framework of a tight binding model [11, 137]. Taking an infinite Co bilayer, the shift of the band as a function of the Co-Co bond length is given by $\Delta E(\vec{k}, r) = \beta(r)F(\vec{k}, r)$, where $F(\vec{k}, r)$ is a positive sum of k-dependent cosine functions ($\| \vec{k} \| < \pi/2r$). Following [137], we express the transfer integral as $\beta = \beta_0 exp(-qr)$, where $q$ is a positive material-dependent constant, and neglect the crystal-field contribution. For occupied electronic states the transfer integral is negative ($\beta_0 < 0$), and in the limit of a small variation of the average bond length ($r = r_0 - \delta r$) as in Fig. 6.4(b), it follows that $\Delta E \propto (1 + q\,\delta r)\,\beta_0$. Peak $p1$ and $p2$ both exhibit a negative shift close in amplitude, which decreases linearly with decreasing Co-Co bond length [Fig. 6.4(b) and Fig. 6.5(b)]. On the contrary, the unoccupied minority $d$ band [peak $p3$] is unlikely to shift in energy. This follows from the flat nature of the unoccupied minority band around the $\Gamma$-point, which then implies a narrow bandwidth ($\beta_0$ is close to zero) and, hence, a negligible energy shift.[134]

The impact of atomic relaxations in Co nanoislands on the energy position of the occupied surface revealed in this work confirms the predictions on mesoscopic relaxation [87, 86]. Our results give clear evidence that the surface-state electrons on nanoislands are significantly affected by the local atomic structure. When the size of the island decreases, i.e., with increasing lateral strain, the occupied states move to lower energies. A variation of the catalytic activity can then be expected with island size [138].
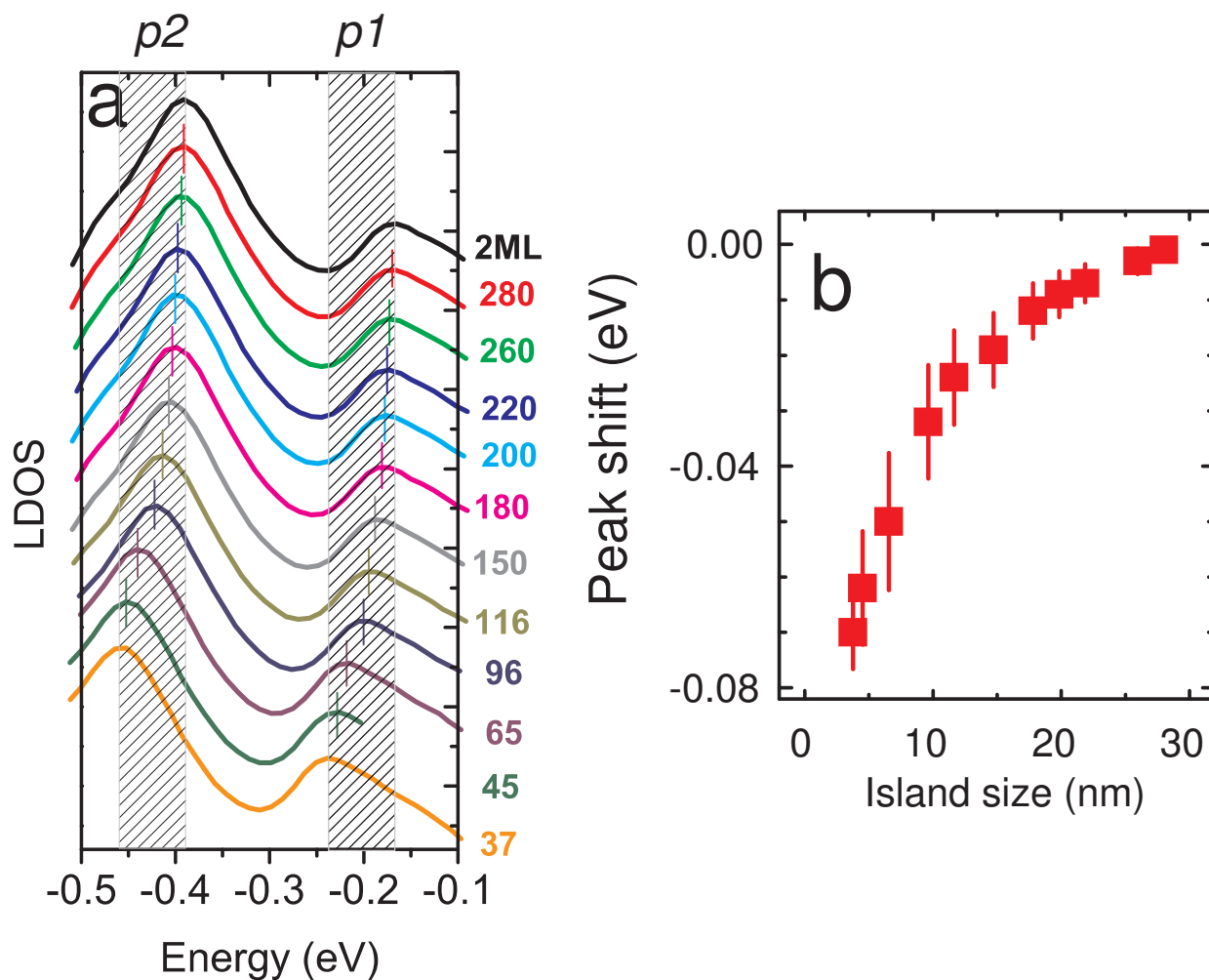
**Figure 6.5:** a) Vacuum LDOS over Co bilayers with Co-Co in-plane bond length and interlayer separations adopted from the MD simulations [see Fig. 6.5(a,b)]. Corresponding island size is denoted on right side of each curve. Vertical ticks demonstrates peak *p1* position. The hatched areas delimit the range over which an energy shift is observed for peak *p*1 and *p*2 in these spectra. b) Energy shift of peak *p*1 in the center of islands with increasing size. The figure is published in [134].

# Conclusions

In this work we present the results on studies of spin-polarized surface states arising on noble metal substrates decorated with low-dimensional magnetic nanostructures.

By means of ab initio calculations we investigated surface states on clean Cu(111) stepped surfaces. In agreement with previous experimental works electronic states significantly affected by repulsive potential at steps have been found close to the Fermi energy. Our calculations have demonstrated that the position of such states is strongly dependent on the terrace width. The strength of the potential barrier at the step edges has been found to be in good agreement with experimentally determined values.

It has been shown monatomic Fe rows placed at steps ledges can significantly affect surface states on vicinal surfaces. Surface states become spin polarized due to spin-dependent scattering of surface-state and bulk electrons at Fe wires: the majority surface states remain unaffected; the minority states get localized at Fe wires. Such localization suppresses the confinement-like features in surface states electronic structure.

Our ab initio calculations have revealed that the surface-state-mediated adatom-step and adatom-adatom interactions can be exploited for the self-organization of Fe adatoms on vicinal Cu(111) surfaces at low temperatures. The interatomic separation (1.2 nm) in such kind of nanostructures is determined by the wavelength of the surface-state charge density oscillations.

Development of Cu(111) surace state above magnetic Co clusters of an increasing size, from a single adatom up to bilayer has been considered. It has been revealed that surface states above small clusters strongly depend on a cluster size. Surface states of large clusters are close to those of monolayers, with the exception to the minority resonance right at the Fermi level.

Origins of spin-polarized surface states on Ci bilayer have been revealed. The interplay between the Co bilayer stacking and spin-polarized surface states has been demonstrated. The essential role of the substrate on the surface states energies has been shown.

The effect of the size-dependent mesoscopic relaxation of Co nanoislands on spin-polarized surface states has been demonstrated by means of combined atomic scale simulations and ab initio calculations. It has been shown that relaxation-driven Co-Co in-plane bond contraction governs the position of surface states on Co nanoislands.

# Bibliography

[1] I. E. Tamm. *Z. Phys.*, 76:849, 1932.

[2] Katsnelson A. A., Stepanyuk V. S., Szasz A., and Farberovich O. V. *Computational Methods in Condensed Matter.* AIP press, 1992.

[3] R. M. Martin. *Electronic structure: basic theory and practical methods.* Cambridge university press, 2004.

[4] F. Bloch. über die quantenmechanik der elektronen in kristallgittern. *Z.Physik*, 52:555, 1928.

[5] G. Floquet. Sur les équations différentielles linéaires á coefficients périodiques. *Ann. École Norm. Sup.*, 12:47, 1883.

[6] W. Shockley. On the surface states associated with a periodic potential. *Physical Review*, 56:317, 1939.

[7] F. Reinert, G. Nicolay, S. Schmidt, D. Ehm, and S. Hüfner. Direct measurements of the l-gap surface states on the (111) face of noble metals by photoelectron spectroscopy. *Physical Review B*, 63:115415, 2001.

[8] E. I. Rashba. *Fiz. Tverd. Tela (Leningrad)*, 2:1224, 1960.

[9] G. Feve, W. D. Oliver, M. Aranzana, and Y. Yamamoto. Rashba effect within the coherent scattering formalism. *Phys. Rev. B*, 66:155328, 2002.

[10] J. Henk, A. Ernst, and P. Bruno. Spin polarization of the l-gap surface states on au(111). *Phys. Rev. B*, 68:165416, 2003.

[11] Sydney G. Davison and Maria Steslicka. *Basic theory of surface states*, volume 46 of *Monographs of the physics and chemistry of materials.* Oxford: Clarendon Press; New York: Oxford University press, 1992.

[12] N. Memmel. Monitoring and modifying properties of metal surfaces by electronic surface states. *Surface Science Reports*, 32:91, 1998.

[13] L. D. Landau and E. M. Lifshitz. *Quantum mechanics : non-relativistic theory*, volume 3 of *Course of theoretical physics / by L. D. Landau and E. M. Lifshitz.* Pergamon Press, 1999.

[14] J. Tersoff and D. R. Hamann. Theory of the scanning tunneling microscope. *Physical Review B*, 31:805, 1985.

[15] J. Bardeen. Tunnelling from a many-particle point of view. *Physical Review Letters*, 6:57, 1961.

[16] L. C. Davis, M. P. Everson, R. C. Jaklevic, and Weidian Shen. Theory of the local density of surface states on a metal: Comparison with scanning tunneling spectroscopy of a au(111) surface. *Physical Review B*, 43:3821, 1991.

[17] M. F. Crommie, C. P. Lutz, and D. M. Eigler. Imaging standing waves in a two-dimensional electron gas. *Nature*, 363:524, 1993.

[18] J. Li, W.-D. Schneider, R. Berndt, and S. Crampin. Electron confinement to nanoscale ag islands on ag(111): A quantitative study. *Physical Review Letters*, 80:3332, 1998.

[19] L. Bürgi, O. Jeandupeux, A. Hirstein, H. Brune, and K. Kern. Confinement of surface state electrons in fabry-pérot resonators. *Physical Review Letters*, 81:5370, 1998.

[20] G. Rodary, D. Sander, H. Liu, H. Zhao, L. Niebergall, V. S. Stepanyuk, P. Bruno, and J. Kirschner. Quantization of the electron wave vector in nanostructures: Counting k-states. *Physical Review B*, 75:233412, 2007.

[21] S. Crampin, H. Jensen, J. Kröger, L. Limot, and R. Berndt. Resonator design for use in scanning tunneling spectroscopy studies of surface electron lifetimes. *Physical Review B*, 72:035443, 2005.

[22] A. Mugarza, F. Schiller, Cordón J. Kuntze, J., M. Ruiz-Osés, and J. E. Ortega. Modelling nanostructures with vicinal surfaces. *Journal of Physics: Condensed Matter*, 18:S27, 2006.

[23] L. Niebergall, G. Rodary, H. F. Ding, D. Sander, V. S. Stepanyuk, P. Bruno, and J. Kirschner. Electron confinement in hexagonal vacancy islands: Theory and experiment. *Physical Review B*, 74:195436, 2006.

[24] J. E. Ortega, S. Speller, A. R. Bachmann, A. Mascaraque, E. G. Michel, A. Närmann, A. Mugarza, A. Rubio, and F. J. Himpsel. Electron wave function at a vicinal surface: Switch from terrace to step modulation. *Physical Review Letters*, 84:6110, 2000.

[25] M. F. Crommie, C. P. Lutz, and D. M. Eigler. Confinement of electrons to quantum corrals on a metal surface. *Science*, 262:218, 1993.

[26] E. J. Heller, M. F. Crommie, C. P. Lutz, and D. M. Eigler. Scattering and absorption of surface electron waves in quantum corrals. *Nature*, 369:464, 1994.

[27] S. Crampin and O. R. Bryant. Fully three-dimensional scattering calculations of standing electron waves in quantum nanostructures: The importance of quasiparticle interactions. *Physical Review B*, 54:R17367, 1996.

[28] H. C. Manoharan, C. P. Lutz, and D. M. Eigler. Quantum mirages formed by coherent projection of electronic structure. *Nature*, 403:512, 2000.

[29] V. Madhavan, W. Chen, T. Jamneala, M. F. Crommie, and N. S. Wingreen. Tunneling into a Single Magnetic Atom: Spectroscopic Evidence of the Kondo Resonance. *Science*, 280:567, 1998.

[30] J. Li, W.-D.r Schneider, R. Berndt, and B. Delley. Kondo scattering observed at a single magnetic impurity. *Physical Review Letters*, 80:2893, 1998.

[31] T. Jamneala, V. Madhavan, and M. F. Crommie. Kondo response of a single antiferromagnetic chromium trimer. *Physical Review Letters*, 87:256804, 2001.

[32] N. Knorr, M. A. Schneider, L. Diekhöner, P. Wahl, and K. Kern. Kondo effect of single co adatoms on cu surfaces. *Physical Review Letters*, 88:096804, 2002.

[33] O. Újsághy, J. Kroha, L. Szunyogh, and A. Zawadowski. Theory of the fano resonance in the stm tunneling density of states due to a single kondo impurity. *Physical Review Letters*, 85:2557, 2000.

[34] P. Wahl, P. Simon, L. Diekhöner, V. S. Stepanyuk, P. Bruno, M. A. Schneider, and K. Kern. Exchange interaction between single magnetic adatoms. *Physical Review Letters*, 98(5):056601, 2007.

[35] V. S. Stepanyuk, L. Niebergall, W. Hergert, and P. Bruno. Ab initio study of mirages and magnetic interactions in quantum corrals. *Physical Review Letters*, 94:187201, 2005.

[36] V S Stepanyuk, N N Negulyaev, L Niebergall, and P Bruno. Effect of quantum confinement of surface electrons on adatom&ndash;adatom interactions. *New Journal of Physics*, 9:388, 2007.

[37] A. A. Correa, F. A. Reboredo, and C. A. Balseiro. Quantum corral wave-function engineering. *Physical Review B*, 71:035418, 2005.

[38] C. Trallero-Giner, S. E. Ulloa, and V. López-Richard. Local density of states in parabolic quantum corrals. *Physical Review B*, 69:115423, 2004.

[39] N. A. Stavropoulos and D. K. Morr. Quantum imaging and selection rules in triangular quantum corrals. *Physical Review B*, 71:140501, 2005.

[40] B. Simon. The bound state of weakly coupled schrödinger operators in one and two dimensions. *Ann. Phys.*, 97:279, 1976.

[41] L. Limot, E. Pehlke, J. Kröger, and R. Berndt. Surface-state localization at adatoms. *Physical Review Letters*, 94:036805, 2005.

[42] F. E. Olsson, M. Persson, A. G. Borisov, J.-P. Gauyacq, J. Lagoute, and S. Fölsch. Localization of the cu(111) surface state by single cu adatoms. *Physical Review Letters*, 93:206803, 2004.

[43] J. P. Gauyacq, A. G. Borisov, and A. K. Kazansky. Impurity-induced localisation of the 2d surface-state continuum on a metal surface. *Applied Physics A: Materials Science & Processing*, 78:141, 2004.

[44] D. M. Newns. Self-consistent model of hydrogen chemisorption. *Physical Review*, 178:1123, 1969.

[45] V. S. Stepanyuk, A. N. Klavsyuk, L. Niebergall, and P. Bruno. End electronic states in cu chains on cu(111): Ab initio calculations. *Physical Review B*, 72:153407, 2005.

[46] B. Lazarovits, L. Szunyogh, and P. Weinberger. Spin-polarized surface states close to adatoms on cu(111). *Physical Review B*, 73:045430, 2006.

[47] S. Lounis, P. Mavropoulos, P. H. Dederichs, and S. Blügel. Surface-state scattering by adatoms on noble metals: Ab initio calculations using the korringa-kohn-rostoker green function method. *Physical Review B*, 73:195421, 2006.

[48] L. Diekhöner, M. A. Schneider, A. N. Baranov, V. S. Stepanyuk, P. Bruno, and K. Kern. Surface states of cobalt nanoislands on cu(111). *Physical Review Letters*, 90:236801, 2003.

[49] O. Pietzsch, A. Kubetzka, M. Bode, and R. Wiesendanger. Spin-polarized scanning tunneling spectroscopy of nanoscale cobalt islands on cu(111). *Physical Review Letters*, 92:057202, 2004.

[50] L. Niebergall, V. S. Stepanyuk, J. Berakdar, and P. Bruno. Controlling the spin polarization of nanostructures on magnetic substrates. *Physical Review Letters*, 96:127204, 2006.

[51] O. Pietzsch, S. Okatov, A. Kubetzka, M. Bode, S. Heinze, A. Lichtenstein, and R. Wiesendanger. Spin-resolved electronic structure of nanoscale cobalt islands on cu(111). *Physical Review Letters*, 96:237203, 2006.

[52] F. Meier, K. von Bergmann, P. Ferriani, J. Wiebe, M. Bode, K. Hashimoto, S. Heinze, and R. Wiesendanger. Spin-dependent electronic and magnetic properties of co nanostructures on pt(111) studied by spin-resolved scanning tunneling spectroscopy. *Physical Review B*, 74:195411, 2006.

[53] J Wiebe M Bode F Meier, K von Bergmann and R Wiesendanger. Co double-layer nanostructures on pt(111) studied by spin-polarized scanning tunnelling microscopy. *Journal of Physics D: Applied Physics*, 40:1306, 2007.

[54] M. V. Rastei, J. P. Bucher, P. A. Ignatiev, V. S. Stepanyuk, and P. Bruno. Surface electronic states in co nanoclusters on au(111): Scanning tunneling spectroscopy measurements and ab initio calculations. *Physical Review B*, 75:045436, 2007.

[55] M V Rastei and J P Bucher. Spin polarized tunnelling investigation of nanometre co clusters by means of a ni bulk tip. *Journal of Physics: Condensed Matter*, 18:L619, 2006.

[56] M. Julliere. Tunneling between ferromagnetic films. *Physics Letters A*, 54:225, 1975.

[57] W. Wulfhekel, U. Schlikum, and J. Kirschner. *Applied Scanning Probe Methods II: Scanning Probe Microscopy Techniques*, volume Applied Scanning Probe Methods of *NanoScience and Technology*, chapter 4. Spin-polarized scunning tunneling microscopy, page 121. Springer Verlag, 2006.

[58] J. C. Slonczewski. Conductance and exchange coupling of two ferromagnets separated by a tunneling barrier. *Physical Review B*, 39:6995, 1989.

[59] C. Rau and S. Eichner. Electron-spin polarization at single-crystalline cr and ni surfaces determined with electron-capture spectroscopy. *Phys. Rev. Lett.*, 47(13):939, 1981.

[60] P. Hohenberg and W. Kohn. Inhomogeneous electron gas. *Physical Review*, 136:B864, 1964.

[61] D. Joubert, editor. *Density Functionals: Theory and Applications*, volume 500 of *Lecture notes in physics*. Springer, 1998.

[62] P. Weinberger. *Electron scattering theory for ordered and disordered matter*. Oxford university press, 1990.

[63] J . Korringa. On the calculation of the energy of a bloch wave in a metal. *Physica*, 13:392.

[64] W. Kohn and N. Rostoker. Solution of the schrödinger equation in periodic lattices with an application to metallic lithium. *Physical Review*, 94:1111, 1954.

[65] A. Gonis. *Green functions for ordered and disordered systems*, volume 4 of *Studies in mathematical physics*. North-Holland Elsevier science publishers B.V., 1992.

[66] J. Zabloudil, Hammerling R., Szunyogh L., and Weinberger P. *Electron scattering in solid matter: a theoretical and computational treatise*, volume 147 of *Springer Series in solid-state sciences*. Springer Verlag, Berlin, 2005.

[67] I. Mertig, E. Mrosan, and P. Ziesche. *Multiple scattering theory of point defects in metals : electronic properties*, volume 11 of *Teubner-Texte zur Physik*. Teubner, 1987.

[68] R. Zeller and P. H. Dederichs. Electronic structure of impurities in cu, calculated self-consistently by korringa-kohn-rostoker green's-function method. *Physical Review Letters*, 42:1713, 1979.

[69] R. Podloucky, R. Zeller, and P. H. Dederichs. Electronic structure of magnetic impurities calculated from first principles. *Physical Review B*, 22:5777, 1980.

[70] K. Wildberger, R. Zeller, and P. H. Dederichs. Screened kkr-green's-function method for layered systems. *Physical Review B*, 55:10074, 1997.

[71] P. Mavropoulos and N. Papanikolaou. The korringa-kohn-rostoker (kkr) green function method. volume 31, page 131. John von Neumann Institute for Computing, Jülich, 2006.

[72] R Zeller N Papanikolaou and P H Dederichs. Conceptual improvements of the kkr method. *Journal of Physics: Condensed Matter*, 14:2799, 2002.

[73] R. Zeller, P. H. Dederichs, B. Újfalussy, L. Szunyogh, and P. Weinberger. Theory and convergence properties of the screened korringa-kohn-rostoker method. *Physical Review B*, 52:8807, 1995.

[74] K. Wildberger, V. S. Stepanyuk, P. Lang, R. Zeller, and P. H. Dederichs. Magnetic nanostructures: 4 d clusters on ag(001). *Physical Review Letters*, 75:509, 1995.

[75] P. J. Braspenning, R. Zeller, A. Lodder, and P. H. Dederichs. Self-consistent cluster calculations with correct embedding for 3*d*, 4*d*, and some *sp* impurities in copper. *Physical Review B*, 29:703, 1984.

[76] V. S. Stepanyuk, R. Zeller, P. H. Dederichs, and I. Mertig. Electronic structure and magnetic properties of dilute co alloys with transition-metal impurities. *Physical Review B*, 49:5157, 1994.

[77] A Oswald, R Zeller, P J Braspenning, and P H Dederichs. Interaction of magnetic impurities in cu and ag. *Journal of Physics F: Metal Physics*, 15:193, 1985.

[78] V. S. Stepanyuk, W. Hergert, P. Rennert, K. Wildberger, R. Zeller, and P. H. Dederichs. Magnetic dimers of transition-metal atoms on the ag(001) surface. *Physical Review B*, 54:14121, 1996.

[79] V. S. Stepanyuk, W. Hergert, K. Wildberger, R. Zeller, and P. H. Dederichs. Magnetism of 3d, 4d, and 5d transition-metal impurities on pd(001) and pt(001) surfaces. *Physical Review B*, 53:2121, 1996.

[80] H. J. Monkhorst and J. D. Pack. Special points for brillouin-zone integrations. *Physical Review B*, 13:5188, 1976.

[81] F. Cyrot-Lackmann. Sur le calcul de la cohsion et de la tension superficielle des mtaux de transition par une mthode de liaisons fortes. *Journal of Physics and Chemistry of Solids*, 29:1235, 1968.

[82] F. Cyrot-Lackmann. On the calculation of surface tension in transition metals. *Surface Science*, 15:535, 1969.

[83] F. Ducastelle and F. Cyrot-Lackmann. Moments developments and their application to the electronic charge distribution of d bands. *Journal of Physics and Chemistry of Solids*, 31:1295, 1970.

[84] J. Friedel. Metallic alloys. *Il Nuovo Cimento (1955-1965)*, 7:287, 1958.

[85] V. S. Stepanyuk, D. I. Bazhanov, A. N. Baranov, W. Hergert, P. H. Dederichs, and J. Kirschner. Strain relief and island shape evolution in heteroepitaxial metal growth. *Physical Review B*, 62:15398, 2000.

[86] V. S. Stepanyuk, D. I. Bazhanov, W. Hergert, and J. Kirschner. Strain and adatom motion on mesoscopic islands. *Physical Review B*, 63:153406, 2001.

[87] O. V. Lysenko, V. S. Stepanyuk, W. Hergert, and J. Kirschner. Mesoscopic relaxation in homoepitaxial metal growth. *Physical Review Letters*, 89:126102, 2002.

[88] N. N. Negulyaev, V. S. Stepanyuk, P. Bruno, L. Diekhöner, P. Wahl, and K. Kern. Bilayer growth of nanoscale co islands on cu(111). *Physical Review B*, 77:125437, 2008.

[89] N. N. Negulyaev, V. S. Stepanyuk, W. Hergert, P. Bruno, and J. Kirschner. Atomic-scale self-organization of fe nanostripes on stepped cu(111) surfaces: Molecular dynamics and kinetic monte carlo simulations. *Physical Review B*, 77:085430, 2008.

[90] Š. Pick, P. A. Ignatiev, A. L. Klavsyuk, W. Hergert, V. S. Stepanyuk, and P. Bruno. Structure and magnetic properties of co chains on a stepped cu surface. *Journal of Physics: Condensed Matter*, 19:446001, 2007.

[91] O. Mironets, H. L. Meyerheim, C. Tusche, V. S. Stepanyuk, E. Soyka, P. Zschack, H. Hong, N. Jeutter, R. Felici, and J. Kirschner. Direct evidence for mesoscopic relaxations in cobalt nanoislands on cu(001). *Physical Review Letters*, 100:096103, 2008.

[92] V. S. Stepanyuk, L. Niebergall, R. C. Longo, W. Hergert, and P. Bruno. Magnetic nanostructures stabilized by surface-state electrons. *Physical Review B*, 70:075414, 2004.

[93] M. A. Van Hove and G. A. Somorjai. A new microfacet notation for high-miller-index surfaces of cubic materials with terrace, step and kink structures. *Surface Science*, 92:489, 1980.

[94] J. Shen, R. Skomski, M. Klaua, H. Jenniches, S. Sundar Manoharan, and J. Kirschner. Magnetism in one dimension: Fe on cu(111). *Physical Review B*, 56:2340, 1997.

[95] J. Shen, M. Klaua, P. Ohresser, H. Jenniches, J. Barthel, Ch. V. Mohan, and J. Kirschner. Structural and magnetic phase transitions of fe on stepped cu(111). *Physical Review B*, 56:11134, 1997.

[96] P. Gambardella, M. Blanc, L. Bürgi, K. Kuhnke, and K. Kern. Co growth on pt(997): from monatomic chains to monolayer completion. *Surface Science*, 449:93, 2000.

[97] S. Shiraki, H. Fujisawa, M. Nantoh, and M. Kawai. Confining barriers for surface state electrons tailored by monatomic fe rows on vicinal au(111) surfaces. *Physical Review Letters*, 92:096102, 2004.

[98] V. Bellini, N. Papanikolaou, R. Zeller, and P. H. Dederichs. Magnetic 4*d* monoatomic rows on ag vicinal surfaces. *Physical Review B*, 64:094403, 2001.

[99] O. Sánchez, J. M. García, P. Segovia, J. Alvarez, A. L. Vázquez de Parga, J. E. Ortega, M. Prietsch, and R. Miranda. Lateral confinement of surface states on stepped cu(111). *Physical Review B*, 52:7894, 1995.

[100] M. Hansmann, J. I. Pascual, G. Ceballos, H.-P. Rust, and K. Horn. Scanning tunneling spectroscopy study of cu(554): confinement and dimensionality at a stepped surface. *Physical Review B*, 67:121409, 2003.

[101] R. de L. Kronig and W. G. Penney. Quantum mechanics of electrons in crystal lattices. *Proceedings of the Royal Society of London. Series A, Containing Papers of a Mathematical and Physical Character (1905-1934)*, 130:499, 1931.

[102] P. A. Ignatiev, V. S. Stepanyuk, A. L. Klavsyuk, W. Hergert, and P. Bruno. Electronic confinement on stepped cu(111) surfaces: Ab initio study. *Physical Review B*, 75:155428, 2007.

[103] J. E. Ortega, M. Ruiz-Osés, J. Cordón, A. Mugarza, J. Kuntze, and F. Schiller. One-dimensional versus two-dimensional electronic states in vicinal surfaces. *New Journal of Physics*, 7:101, 2005.

[104] P. Gambardella, S. Rusponi, M. Veronese, S. S. Dhesi, C. Grazioli, A. Dallmeyer, I. Cabria, R. Zeller, P. H. Dederichs, K. Kern, C. Carbone, and H. Brune. Giant magnetic anisotropy of single cobalt atoms and nanoparticles. *Science*, 300:1130, 2003.

[105] J. Dorantes-Dávila and G. M. Pastor. Magnetic anisotropy of one-dimensional nanostructures of transition metals. *Physical Review Letters*, 81:208, 1998.

[106] J. Dorantes-Dávila and G. M. Pastor. Magnetic reorientation transitions along the crossover from one-dimensional to two-dimensional transition-metal nanostructures. *Physical Review B*, 72:085427, 2005.

[107] F. Baumberger, T. Greber, B. Delley, and J. Osterwalder. Tailoring confining barriers for surface states by step decoration: Co /vicinal cu(111). *Physical Review Letters*, 88:237601, 2002.

[108] S. Shiraki, H. Fujisawa, M. Nantoh, and M. Kawai. One-dimensional fe nanostructures formed on vicinal au(111) surfaces. *Journal of the Physical Society of Japan*, 74:2033, 2005.

[109] C. Didiot, A. Tejeda, Y. Fagot-Revurat, V. Repain, B. Kierren, S. Rousset, and D. Malterre. Interacting quantum box superlattice by self-organized co nanodots on au(788). *Physical Review B*, 76:081404, 2007.

[110] C. Didiot, S. Pons, B. Kierren, Y. Fagot-Revurat, and D. Malterre. Nanopatterning the electronic properties of gold surfaces with self-organized superlattices of metallic nanostructures. *Nat Nano*, 2:617, 2007.

[111] K. Morgenstern, K.-H. Rieder, and G. A. Fiete. Disorder-induced local-density-of-states oscillations on narrow ag(111) terraces. *Physical Review B*, 71:155413, 2005.

[112] P. Gambardella, A. Dallmeyer, K. Maiti, M. C. Malagoli, S. Rusponi, P. Ohresser, W. Eberhardt, C. Carbone, and K. Kern. Oscillatory magnetic anisotropy in one-dimensional atomic wires. *Physical Review Letters*, 93:077203, 2004.

[113] J. Guo, Y. Mo, E. Kaxiras, Z. Zhang, and H. H. Weitering. Formation of monatomic fe chains on vicinal cu(111) surfaces: An atomistic view. *Physical Review B*, 73:193405, 2006.

[114] F. J. Himpsel, J. E. Ortega, G. J. Mankey, and R. F. Willis. Magnetic nanostructures. *Advances in Physics*, 7:11.

[115] N. Knorr, H. Brune, M. Epple, A. Hirstein, M. A. Schneider, and K. Kern. Long-range adsorbate interactions mediated by a two-dimensional electron gas. *Physical Review B*, 65:115420, 2002.

[116] K. H. Lau and W. Kohn. Indirect long-range oscillatory interaction between adsorbed atoms. *Surface Science*, 75:69, 1978.

[117] Michael L. Merrick, Weiwei Luo, and Kristen A. Fichthorn. Substrate-mediated interactions on solid surfaces: theory, experiment, and consequences for thin-film morphology. *Progress in Surface Science*, 72:117, 2003.

[118] P. Hyldgaard and M. Persson. Long-ranged adsorbate-adsorbate interactions mediated by a surface-state band. *Journal of Physics: Condensed Matter*, 12:L13, 2000.

[119] V. S. Stepanyuk, A. N. Baranov, D. V. Tsivlin, W. Hergert, P. Bruno, N. Knorr, M. A. Schneider, and K. Kern. Quantum interference and long-range adsorbate-adsorbate interactions. *Physical Review B*, 68:205410, 2003.

[120] J. Repp, F. Moresco, G. Meyer, K.-H. Rieder, P. Hyldgaard, and M. Persson. Substrate mediated long-range oscillatory interaction between adatoms: Cu /cu(111). *Physical Review Letters*, 85:2981, 2000.

[121] F. Silly, M. Pivetta, M. Ternes, F.. Patthey, J. P. Pelz, and W.-D. Schneider. Creation of an atomic superlattice by immersing metallic adatoms in a two-dimensional electron sea. *Physical Review Letters*, 92:016101, 2004.

[122] V. S. Stepanyuk, N. N. Negulyaev, L. Niebergall, R. C. Longo, and P. Bruno. Adatom self-organization induced by quantum confinement of surface electrons. *Physical Review Letters*, 97:186403, 2006.

[123] H. F. Ding, V. S. Stepanyuk, P. A. Ignatiev, N. N. Negulyaev, L. Niebergall, M. Wasniowska, C. L. Gao, P. Bruno, and J. Kirschner. Self-organized long-period adatom strings on stepped metal surfaces: Scanning tunneling microscopy, ab initio calculations, and kinetic monte carlo simulations. *Physical Review B*, 76:033409, 2007.

[124] R. Smoluchowski. Anisotropy of the electronic work function of metals. *Physical Review*, 60:661, 1941.

[125] Y. Mo, K. Varga, E. Kaxiras, and Z. Zhang. Kinetic pathway for the formation of fe nanowires on stepped cu(111) surfaces. *Physical Review Letters*, 94:155503, 2005.

[126] E. Y. Tsymbal, O. N. Mryasov, and P. R. LeClair. Spin-dependent tunnelling in magnetic tunnel junctions. *Journal of Physics: Condensed Matter*, 15:R109, 2003.

[127] J. de la Figuera, J. E. Prieto, C. Ocal, and R. Miranda. Scanning-tunneling-microscopy study of the growth of cobalt on cu(111). *Physical Review B*, 47:13043, 1993.

[128] M. O. Pedersen, I. A. Bonicke, E. Laegsgaard, I. Stensgaard, A. Ruban, J. K. Norskov, and F. Besenbacher. Growth of co on cu(111): subsurface growth of trilayer co islands. *Surface Science*, 387:86, 1997.

[129] Ch. Wöll, S. Chiang, R. J. Wilson, and P. H. Lippel. Determination of atom positions at stacking-fault dislocations on au(111) by scanning tunneling microscopy. *Physical Review B*, 39:7988, 1989.

[130] J. V. Barth, H. Brune, G. Ertl, and R. J. Behm. Scanning tunneling microscopy observations on the reconstructed au(111) surface: Atomic structure, long-range superstructure, rotational domains, and surface defects. *Physical Review B*, 42:9307, 1990.

[131] B. Voigtländer, G. Meyer, and Nabil M. Amer. Epitaxial growth of thin magnetic cobalt films on au(111) studied by scanning tunneling microscopy. *Physical Review B*, 44:10354, 1991.

[132] H. Bulou and J.-P. Bucher. Long range substrate mediated mass transport on metal surfaces induced by adatom clusters. *Physical Review Letters*, 96:076102, 2006.

[133] I. Chado, C. Goyhenex, H. Bulou, and J. P. Bucher. Cluster critical size effect during growth on a heterogeneous surface. *Physical Review B*, 69:085413, 2004.

[134] M. V. Rastei, B. Heinrich, L. Limot, P. A. Ignatiev, V. S. Stepanyuk, P. Bruno, and J. P. Bucher. Size-dependent surface states of strained cobalt nanoislands on cu(111). *Physical Review Letters*, 99:246102, 2007.

[135] Juarez L.F. Da Silva, Catherine Stampfl, and Matthias Scheffler. Converged properties of clean metal surfaces by all-electron first-principles calculations. *Surface Science*, 600:703, 2006.

[136] J. Tersoff and R. M. Tromp. Shape transition in growth of strained islands: Spontaneous formation of quantum wires. *Phys. Rev. Lett.*, 70:2782, 1993.

[137] J. Friedel. *Electrons*, volume I of *The Physics of Metals*. Cambridge University Press, London, 1969, 1969.

[138] M. Mavrikakis, B. Hammer, and J. K. Nørskov. Effect of strain on the reactivity of metal surfaces. *Phys. Rev. Lett.*, 81:2819, 1998.

# Veröffentlichungen

Teile der vorliegenden Arbeit wurden an folgenden Stellen veröffentlicht:

1. M. V. Rastei, B. Heinrich, L. Limot, P. A. Ignatiev, V. S. Stepanyuk, P. Bruno, J.-P. Bucher
   *Size-dependent surface states of strained cobalt nanoislands on Cu(111)*
   Physical Review Letters **99**, 246102 (2007).

2. P. .A. Ignatiev, V. .S. Stepanyuk, L. Niebergall,P. Bruno, J. Berakdar
   *Interplay of electronic, magnetic and structural properties of surface-supported clusters*
   European Physical Journal D **45**, 547 (2007).

3. Š. Pick, P. A. Ignatiev, A. L. Klavsyuk, W. Hergert, V. S. Stepanyuk, P. Bruno
   *Structure and magnetic properties of Co chains on a stepped Cu surface*
   Journal of Physics: Condensed Matter **19**, 446001 (2007).

4. H. F. Ding, V. S. Stepanyuk, P. A. Ignatiev,N. N. Negulyaev, L. Niebergall, M. Wasniowska, C. L. Gao, P. Bruno, J. Kirschner
   *Self-organized long-period adatom strings on stepped metal surfaces: Scanning tunneling microscopy, ab initio calculations, and kinetic Monte Carlo simulations*
   Physical Review B **76**, 033409 (2007)

5. P. A. Ignatiev, V. S. Stepanyuk, A. L. Klavsyuk, W. Hergert, P. Bruno
   *Electronic confinement in stepped Cu(111) surfaces: Ab initio study*
   Physical Review B **75** 155428 (2007)

6. M. V. Rastei, J.-P. Bucher, P. A. Ignatiev, V. S. Stepanyuk, P. Bruno
   *Surface electronic states in Co nanoclusters on Au(111): Scanning tunneling spectroscopy measurements and ab initio calculations*
   Physical Review B **75**, 045436 (2007).

# Curriculum Vitae

| | |
|---|---|
| **Name, Vorname:** | Pavel, Ignatiev |
| **Geburtsdatum:** | 11/02/1979 |
| **Geburtsort:** | Puschtshino, Moskauer Gebiet |
| **Staatsangehörigkeit:** | Russland |
| **Familienstand:** | Verheiratet, 1 Kind (2 Jahre) |
| **Adresse (privat):** | Fuhneweg 11, 06122, Halle |
| **Adresse (dienstlich):** | Weinberg 2, 06120, Halle |

## Ausbildung and Qualifikation

| | |
|---|---|
| **1985-1995** | Mittelschule N2 der Stadt Puschtschino der Moskauer Gebiet |
| **1995-2001** | Physikstudium an der Staatlichen Universität namens Lomonosov M. V. Moskau, Physikalische Fakultät, Fachrichtung: Physik, Spezialgebiet: Computermethode der Physik. Abschluß: Dipl.-Phys. |
| **2001-2004** | Promotion auf dem Gebiet der Computermethode der Physik, Staatlichen Universität namens Lomonosov M. V. Moskau, Physikalische Fakultät. *Promotion nicht abgeschlossen.* |
| **2005-** | Wissenschaftlicher Mitarbeiter am Max-Planck-Institut für Mikrostrukturphysik, Halle, Germany |

# Erklärung

Ich versichere hiermit, die vorliegende Dissertation

## Theoretical study of spin-polarized surface states on metal surfaces

selbständig und ohne fremde Hilfe verfasst und keine anderen als die von mir angegebenen Quellen und Hilfsmittel verwendet zu haben. Den benutzten Werken wörtlich oder inhaltlich entnommene Stellen sind als solche gekennzeichnet.

Halle (Saale), 1.07.2008                      Pavel Ignatiev

# Erklärung

Ich versichere hiermit, dass ich mich an keiner wissenschaftlichen Hochschule im Geltungsbereich des deutschen Grundgesetzes bereits früher um den Doktorgrad beworben habe.

Halle (Saale), 1.07.2008                    Pavel Ignatiev

# Acknowledgments

I would like to express my gratitude to my supervisor Prof. Dr. V.S. Stepanyuk for his guidance and advice. His interest in Physics and numerous intensive discussions were very stimulating for me. Without his support this work would not have appeared.

I would like to appreciate Prof. Dr. P. Bruno for his valuable criticism and experience I have got during his seminars and discussions.

I would like to greatly acknowledge Prof. Dr. J. Kirschner and his coworkers for the experiments performed to check theoretical predictions on the atomic strings.

I am very thankful to Prof. Dr. J.-P. Bucher from IPCM Strasbourg and his coworkers Dr. M.-V. Rastei, Dr. L. Limot, B. Heinrich. The fruitful collaboration with the group of Prof. Bucher gave me the abundant experience.

Many warm and kind thanks are going to Dr. N. Negulaev, Dr. L. Niebergall, O. Brovko, Dr. A. Moskalenko for their help. I am indebted to our system administrator U. Schmidt for his patience and time he spent to solve my problems.

I gratefully acknowledge all the colleagues from the MPI Halle: scientists, technicians and staff of administration, for the stimulating atmosphere. I appreciate the invaluable help of our secretary I. Goffin.

I also want to express my thanks to my parents, my brother and my little daughter

Finally, I thank my dear wife Alevtina for here support and love.

Halle (Saale), 1.07.2008                                        Pavel Ignatiev